MODELING, PATTERN ANALYSIS AND FEATURE-BASED RETRIEVAL ON RETINAL IMAGES

A Dissertation

by

HUAJUN YING

Submitted to the Office of Graduate Studies of
Texas A&M University
in partial fulfillment of the requirements for the degree of

DOCTOR OF PHILOSOPHY

May 2011

Major Subject: Computer Engineering

MODELING, PATTERN ANALYSIS AND FEATURE-BASED RETRIEVAL ON RETINAL IMAGES

A Dissertation

by

HUAJUN YING

Submitted to the Office of Graduate Studies of
Texas A&M University
in partial fulfillment of the requirements for the degree of

DOCTOR OF PHILOSOPHY

Approved by:

Chair of Committee,	Jyh-Charn Liu
Committee Members,	Dezhen Song
	Yoonsuck Choe
	Deepa Kundur
Head of Department,	Valerie Taylor

May 2011

Major Subject: Computer Engineering

ABSTRACT

Modeling, Pattern Analysis and Feature-Based Retrieval on Retinal Images.

(May 2011)

Huajun Ying, B.S. Shanghai JiaoTong University

Chair of Advisory Committee: Dr. Jyh-Charn (Steve) Liu

Inexpensive high quality fundus camera systems enable imaging of retina for vision related health management and diagnosis at large scale. A computer based analysis system can help establish the general baseline of normal conditions vs. anomalous ones, so that different classes of retinal conditions can be classified. Advanced applications, ranging from disease screening algorithms, aging vs. disease trend modeling and prediction, and content-based retrieval systems can be developed.

In this dissertation, I propose an analytical framework for the modeling of retina blood vessels to capture their statistical properties, so that based on these properties one can develop blood vessel mapping algorithms with self-optimized parameters. Then, other image objects can be registered based on vascular topology modeling techniques. On the basis of these low level analytical models and algorithms, the third major element of this dissertation is a high level population statistics application, in which texture classification of macular patterns is correlated with vessel structures, which can also be used for retinal image retrieval. The analytical models have been implemented and tested based on various image sources. Some of the algorithms have been used for clinical tests.

The major contributions of this dissertation are summarized as follows: (1) A concise, accurate feature representation of retinal blood vessel on retinal images by proposing two feature descriptors S_p and E_p derived from radial contrast transform. (2) A new statistical model of log-normal distribution, which captures the underlying physical property of the levels of generations of the vascular network on retinal images. (3) Fast and accurate detection algorithms for retinal objects, which include retinal blood vessel, macular-fovea area and optic disc, and (4) A novel population statistics based modeling technique for correlation analysis of blood vessels and other image objects that only exhibit subtle texture changes.

To My Parents

ACKNOWLEDGMENTS

First of all, I would like to thank my advisor Dr. Jyh-Charn Liu. He has been more than an advisor for me during the past 5 years of my life. Dr. Liu always gives me trust, inspiration and encouragement not only in my research work, but also my career development and many other things in my life. His unique perspective and deep thoughts on my research topic guided me through the hardest time in my research and gave me courage to conquer the most challenging problem. I found in every talk and discussion with Dr. Liu, the time we spent in finding the new ideas, in debate, or even in a warm casual talk, was the most pleasant time in my doctoral studies. Besides the guidance in research, Dr. Liu also helped me go through the down time during my Ph.D. studies. I would like to say, from the bottom of heart, "Thank you" to Dr. Liu for his years of support.

I am immensely grateful to Dr. Dezhen Song, Dr. Yoonsuck Choe, and Dr. Kundur Deepa for their support in my research study. They give me a lot of input to my research work, and show me a lot of new things, either in computer science aspect, or signal processing aspect. I really appreciate their time spent with me on my research work.

I would like express my appreciation to all my colleagues, and in particular to Dr. Ming Zhang. The cooperation with Dr. Zhang has been very pleasant and productive. When I first came to the lab, he treated me as a brother and guided me through my research from the very fundamental programming skills to algorithm designs. Without his help, I could not have made the progress so quickly. I thank Mr. Pu Duan. We worked as best teammates and friends and overcame the challenges together we met with in our project. I thank Mr. Cheng-Chung Tan, Dr. Hong Lu, Mr. Shengya Lin, Mr. Tao Peng, Mr. Hao Wang, Mr. Shi Pu, Mr. Sanming Liu, Mr. Mike George, Mr. John Pecarina, who were members of a great team in

real-time distribution system lab. I also would like thank all my friends in Texas A&M University. During the whole time of my stay, you have brought me tons of joy and encouragement. Thank you all for being with me when I was in need of your help.

Finally, my deepest gratitude goes to my dear parents and my girlfriend, Cheng Lu, who provide unreserved support to me all the time. Without them, I would not have gone to study abroad and finish my Ph.D.

TABLE OF CONTENTS

CHAPTER Page

LIST OF FIGURES

LIST OF TABLES

CHAPTER I

INTRODUCTION

A. Overview of the Dissertation

Retinal imaging is one of the most important diagnosis and caring tools for both eye diseases and other chronic diseases that may introduce complications in retinal health conditions. With aging of the baby boomer generation and proliferation of chronic diseases like diabetics, there is a strong demand for automated image analysis solutions of retinal images to better capture developing cases at their early stages at low costs. The main theme of this dissertation is to develop an analysis automation framework to support robust, accurate low level image analysis functions, and also high level statistical analysis of high level system dynamics based on the low level analysis results. Major elements of the analytical framework are shown in Figure 1.

Our study starts with in Chapter III, an anatomically-driven modeling technique, which allows us to establish a reliable relationship between blood vessels and a mathematical model with self-optimized parameters. The essence of the proposed modeling technique of blood vessel network is based on observation of *generation levels* [1] of blood vessel branches, which capture the morphological relationships between vessel segments at different

---

This dissertation follows the style of *IEEE Transactions on Image Processing.*

locations. Using pattern analysis and statistical modeling techniques on the *rotational contrast transform (RCT)* of image pixels, we do a quantified reasoning of the transitional

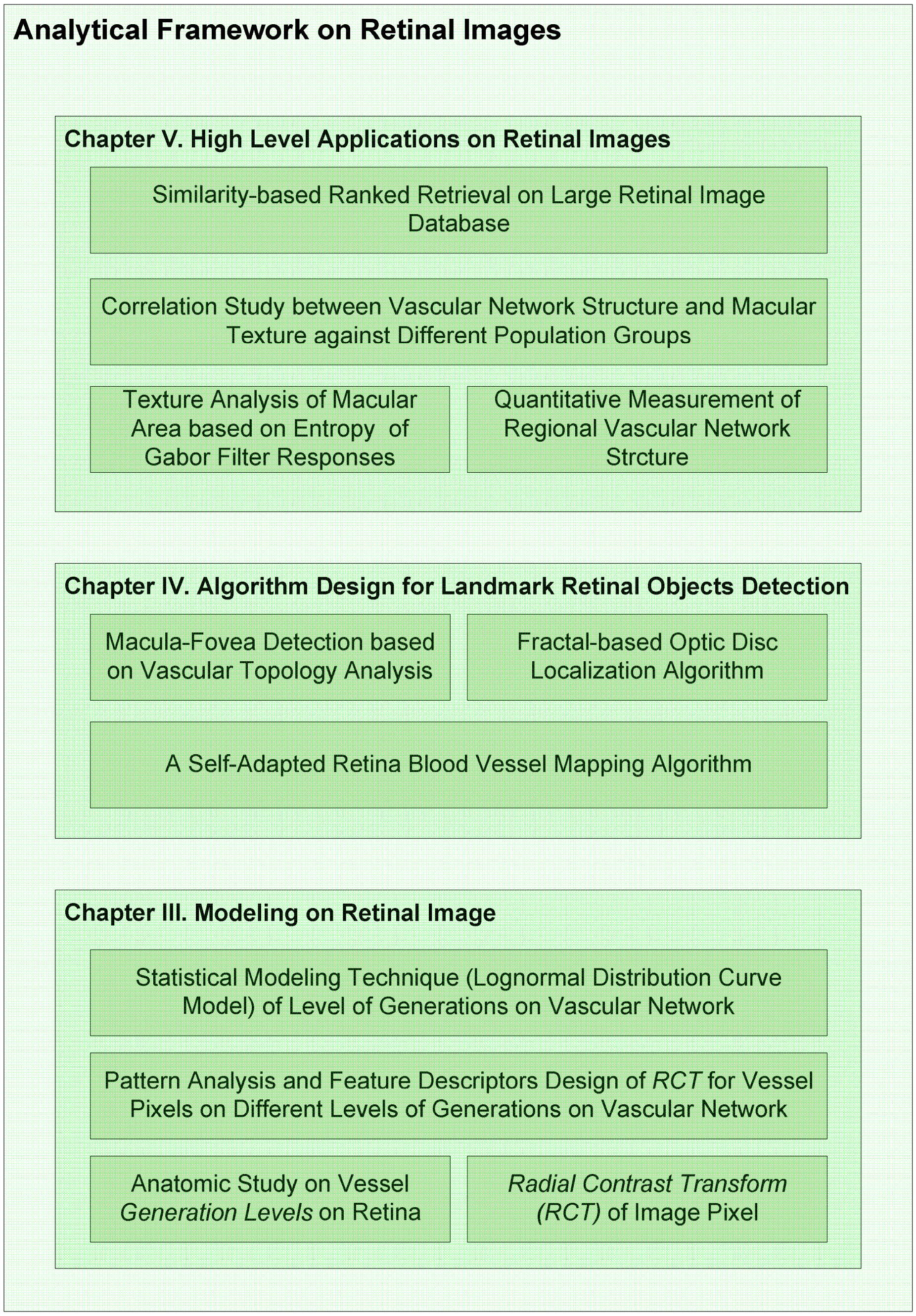

Figure 1: Proposed analytical framework on retinal image.

properties of vessel pixels from center-line vessel to vessel boundary and from pixels on large vessel segment to small ones. The proposed modeling technique provides us a simple yet effective tool in tradeoff analysis between sensitivity and specificity in vessel detection analysis on retinal images.

Continuing on our modeling technique, in Chapter IV, the second major element of our framework is to design algorithms for automated identification of major landmarks on retinal images. Color retinal images can be affected by many factors in flash settings, disease conditions, field clarities, etc, which make accurate segmentation of retinal objects an even more complicated process. Our purpose is to push the limit for less parameter adjustment, resilience to imaging factors, reduction in noise and false detection and reduction in computational cost. Based on the proposed modeling of vessel generation levels, we first present a fast and accurate vessel mapping algorithm. We further utilize the fixed relationship between the vascular network and macula-fovea area as well as the optic disc to locate both macula and optic disc area based on vascular topology analysis. Our algorithms are tested on both two benchmark retinal image databases, STARE [2] and DRIVE [3] as well as the collected data from the clinics. A desirable performance in terms of both accuracy and computational cost is achieved compared to the state-of-art algorithms.

Landmark objects detection facilitates our analysis and data-driven of retinal images by establishing a frame of reference on retinal images. In Chapter V, by means of feature extraction and quantitative measurement, we further develope high level applications on retinal images. The first application involves texture analysis and classification of cropped macular areas. Textures are the main changes manifested in macular areas of people in different ages and health groups. Using the entropy statistics from the Gabor responses of the macular area as their texture features, we are able to classify macular images belonging to three different population groups (healthy young, normal middle age and diseased retinas) reliably. Furthermore, even though qualitative medical studies confirmed that degradation of the vascular network caused by diseases or aging lead to deteriorations of the macular functions, as of now, there are few known quantitative techniques which characterize the relationship between changes in the macular texture from that of the vascular network structure based on retinal images analysis. We take a correlation analysis technique to investigate the relationship between changes in macular textures and changes of blood vessel structures. We conclude the chapter by applying our analytical feature analysis result to the design of a ranked retrieval method on large retinal image database. Initial results on our ranked retrieval algorithms have demonstrated the effectiveness of our method.

B. Overview of Fundus Retinal Image

Fundus color photography has its uniqueness of rich color representation, low cost and non-invasive nature against many other image modalities such as the fluorescein angiography, indocyanine green angiography, scanning laser ophthalmoscope, etc.,. Fundus retinal images are mainly described by their image resolutions, angle of views and field type [4]. Image resolution determines the pixel resolution of the physical size of retina tissue. Based on the camera specification, commercial fundus camera models like Canon 20D or Canon 40D can obtain retinal images of size 3504x2336 or similar, whose pixel resolutions are of 6~10 μm in physical size. For computation efficiency, full resolution images are often downsized to 700x605, 720x480 or similar in research community on retinal images. Our discussion below will be accordingly based on the downsized image, if not particularly specified. Angle of view is the setting of the optical angle of acceptance of the lens on fundus camera, from the narrow-angle of 20 degrees or less, normal-angle of 30 degrees to wider-angle between 45 and 140 degrees. The greater the angle of view, the larger the retinal area is contained in the photograph. Field types of retinal images are defined by ophthalmologists to image and asses different areas on retina. Seven standard fields are utilized as the protocols for retina photography in clinical trials. Most often used retinal images for academic research and in our discussion are of field-1 and field-2 types and have viewing angle of 45º and 60º. Figure 2(a) and (b) shows respectively typical field-1 and field-2 type retinal images of 60º viewing angles. The former one has its field of view (FOV) centering on optic disc area while the latter on the macula-fovea area.

We introduce three landmark retinal objects, including retina blood vessels, optic disc and macula-fovea area on a field-2 type retinal image (See Figure 2(b)). Retina blood vessel (BV) network is the major visible retinal object that covers the whole area of the retinal image. The circulation system of blood vessel supplies nutrients needed for the appropriate work of retina cells. At the same time, the blood supply removes wastes that the cells have produced [5]. The optic disc (OD) is characterized as a bright yellowish disk. It is an important organ on retina from which blood vessels and optic nerves emerge [6]. Macula is another important area near center retina. At the center of the macula is the fovea, which is responsible for sharp central vision [7]. The macular-fovea (M-F) area is a darkened, circular, avascular structure in healthy, normal retina. Anatomical study notes that it is approximately 2~2.5 optic disk diameter away from optic disk center along the raphe of the retina (the line passing through the optic disc and fovea).

(a)

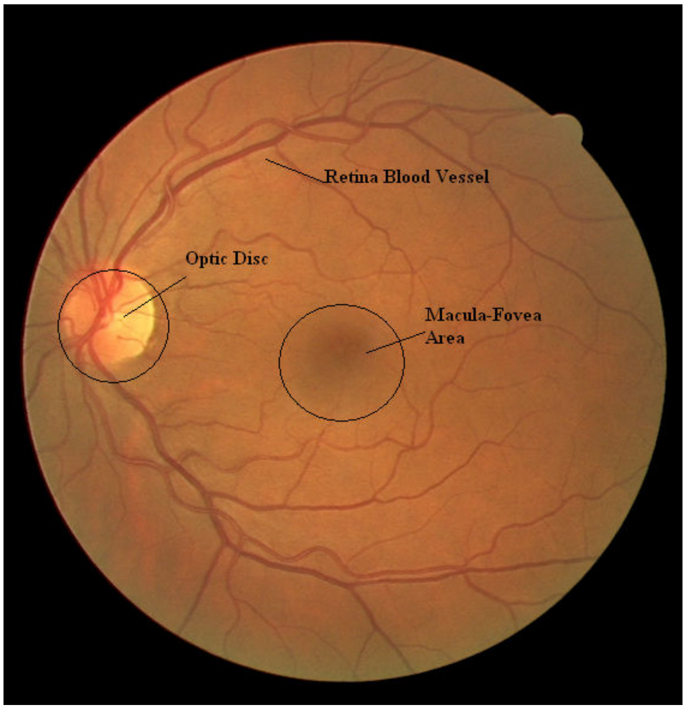

(b)

Figure 2: (a) A field-1 type retinal image. (b) A field-2 type retinal image.

Disorders in retinal objects have been related to retinal implications, which include hypertension, cholesterol, diabetes, glaucoma, age-related macular degeneration (ARMD), etc. Correspondingly, retinal images affected by diseases are laden with different patterns of shapes and sizes. In Figure 3, we show several examples of diseased retinal images. Figure 3(a) is a sample image of neovascularization disease [8]. On it, proliferation of the retina blood vessels is of a different kind than usual with severe occlusions in vessel curvatures. Figure 3(b) shows the occurrences of spot-like patterns of microaneurysms and patches of hemorrhages on retina images, which are caused by blood leakage [9]. Medical studies find that they are usually the early symptoms of diabetics. Figure 3(c) contrasts the change in cup-to-disc ratio within the optic disc through the development of glaucoma diseases [10], where the cup is defined to be the brightest spot within the optic disc area. Figure 3(d) is an example of retina with ARMD, where there are bright yellowish deposits of drusen and hard exudates within and around the macular area.

The main purpose of computer-aided analysis of retina images is to do retina screening which enables image comparison based on automated computer programs and supports disease tracking.

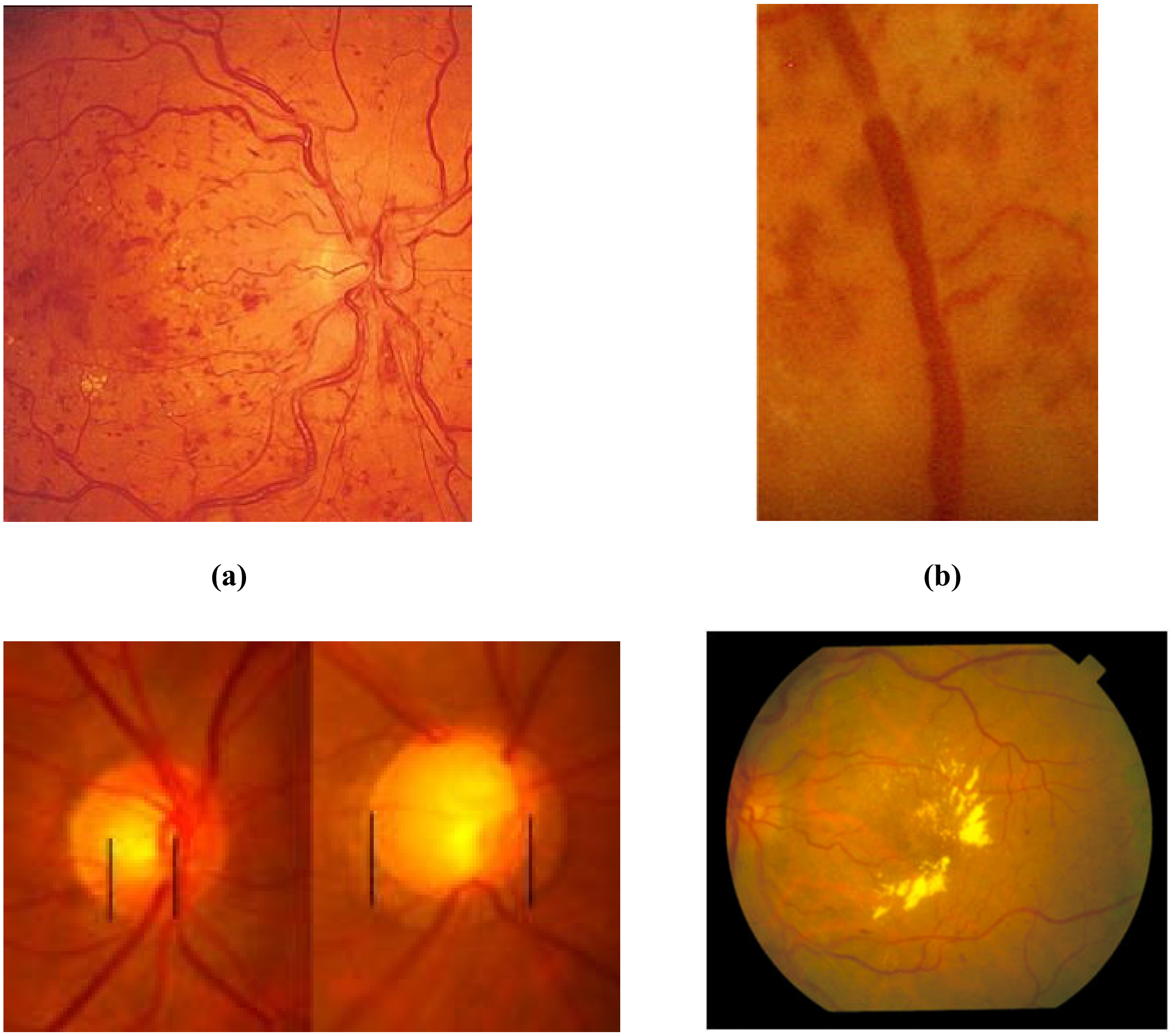

(a)

(b)

(c)

(d)

Figure 3: (a) Occlusion of retina blood vessels due to neovascularization disease (Source: [8]. Courtesy of Dr. S.N.Patel). (b) Occurrences of microaneurhysms (Source: [9]. Courtesy of Dr. Z.Ockrim). (c) Change in cup to disc ratio due to glaucoma disease (Source: [10]. Courtesy of Dr. C.M.Gibson). (d) Example of retina with age related macular degeneration (im0001 from STARE).

C. The Organization of This Dissertation

The rest of this dissertation is organized as follows. In Chapter II, we will review related work in the field of study. In Chapter III, we will introduce our statistical modeling technique on retinal image. In Chapter IV, we will present our algorithms design for retinal objects detection of retina blood vessels, optic disc and macula-fovea area. In Chapter V, we will discusse our high level applications on retinal images including texture analysis, correlation study and ranked retrieval in large retinal image database. We will summarize the dissertation in Chapter VI.

CHAPTER II

RELATED WORK

Numerous research efforts have been made in the area of automated computer-aided analysis of retinal images. State-of-art research in this topic is split into two major areas. One focus is on the detection of main retinal objects which includes algorithm designs for segmentation of retina blood vessels, optic disc and macula-fovea areas. Another more current research focus is content-based retrieval from retinal image databases. A major application in this area is disease screening using retinal images and separation of diseased retinas from healthy ones. In this chapter, we introduce both and discuss briefly the related state-of-art algorithms along with their methods and challenges.

A. Retinal Objects Detection

1. Retina Blood Vessel (BV) Mapping

Many blood vessel mapping algorithms have been proposed. Classical matching filters, e.g., Gaussian distribution, second order derivative Gaussian or Gabor, etc., have been successfully used to match shapes of BV cross sections [11][12][13][14][15][16][17][18][19]. Mathematical morphology operators [20][21][22] have been applied to extract the linear crest lines of BV segments. Continuity in the flows of BV has been widely used for the design of BV flow tracking as a post-filtering step [14][23][24]. It is also essential to the design of intensity threshold probing techniques [25][26]. Unsupervised and supervised learning algorithms [27] [28][29][30][31][32][33][34] have also been proposed to capture BV pixels from their high dimensional features. Despite of the numerous efforts on blood vessel mapping algorithms, few of these addressed algorithmic performance in terms of boundary issues, small and shallow BV detection, and tradeoff analysis between sensitivity and selectivity.

2. Macula-fovea (M-F) Area Segmentation

Direct detection of the M-F area becomes unreliable when the M-F area is of small size and weak contrast. As such, it is more reliable to detect other retinal objects (such like the optic disc or blood vessels) and then use them as a reference to detect M-F area. [35] estimated the optic disk location by a Gaussian tracking strategy and uses it as the vertex of a parabolic curve. This curve wass fitted to blood vessel trajectory using a trained, modified active shape model. It predicted the fovea to be the darkest area that is about 2 disc diameter away from the optic disc center along the main axis of the parabolic curve. Similarly, [36] detected the optic disc in a probabilistic manner. Then, it used a parabola with an axis rotation between +24º to -17º to define the search region of the M-F area to cope with the tilting angle between the raphe and the horizontal line. [37] used the circular Hough transform for optic disc localization. An ellipse obtained from training sets was used to fit the main vessels. A total of 45 parameter sets were defined for different ellipse aspect ratio and inclinations. [38] used a Gaussian intensity template to search for the fovea. On angiographic images, [39] also proposed a Bayesian statistical approach for fovea detection. Existing methods mainly defined or trained their BV trajectory models using images that have adequate field clarity [40], i.e., the optic disc, M-F area and vessel arcades on both superior and inferior sides are all within the field of view. They first detected the OD, and then used it to position the M-F area. However, this approach, as we will discuss in the next session, is subject to interference of diseased objects like hard exudates, drusen, etc, which may have brighter intensity than the OD. Also, retinal images acquired from the field may have inadequate field clarity, e.g. only partial optic disk is included in the image or the superior/inferior side BV arcade is not photographed. The general detection performance for those images is not well known, except that [41] illustrated some false detection outcomes due to parameter selection problems.

3. Optic Disc (OD) Localization

Due to its similar color tone to some other lesions such as hard exudates and cotton wool, accurate OD identification is a critical contributor to reduction of the false positive rate of algorithms designed to detect those lesions. Early detection schemes aimed simply to find the largest clusters of pixels with the highest intensities. However, this simplistic approach was compromised when large hard exudates coexist in the retinal image. Differentiating the two is a challenge. To overcome this, Li and Chutatpe [42] applied principal component analysis to each bright region. Based on images in a training set, eigenvectors of a typical OD were calculated. A new retinal image was projected onto the eigenvectors according to the eigenvalues. The point with the minimum distance between the retinal image and its projection was chosen to be the center of optic disc. This method depended, to a large extent, on the training images, which would affect its correctness for images of different contrast or resolution. Other proposed techniques exploit the information provided by optic disc contour and vessel structure. Lalonde [43] relied on pyramidal decomposition and Hausdorff-based template matching techniques for large scale object tracking. However, this method had difficulty differentiating the optic disc from other large bright round objects such as spot artifacts or hard exudates that are close to the same size as the OD. Similar approach was presented in [44], which detects the OD based on wavelet processing and ellipse fitting. Representation of the OD was mainly based on an intensity template. The algorithm presented in [45] used a geometrical directional pattern to model the OD position as the convergence point of all vessels. It provided a fitting model with respect to the entire vascular structure. It used parameters determined by the vessel directions in the whole retinal image to minimize the weighted residual sum of squares. The algorithm removed local minima by introducing a global stochastic simulated annealing optimization procedure, at the cost of a heavy computational burden. [46] proposed an ultra-fast algorithms for OD localization to boost the computational efficiency of OD localization. It located the optic disc by splitting the screening process into two 1D problems by projecting the image features onto two perpendicular directions. Extraction of the image features included the directionality of vessels and brightness and the sizes of OD. It achieved 87.6% detection rate on STARE with 0.8 seconds per image. Similar to M-F localization, their detection performance on retinal images with poor field clarity were not well discussed.

B. Content-based Image Retrieval in a Retinal Image Database

The concept of content-based image retrieval (CBIR) was proposed in the past two decades [47][48][49][50]. By its name, it refers to the concept of retrieving images from a library based on similarities in image contents. Techniques developed in CBIR differ in mechanisms used to define image contents and in metrics used to measure similarity. For different analysis purposes, image content is usually described by a feature vector, which may be developed into several levels of image features. Commonly used features can be developed into several different semantic levels [51]. The lowest level consists of primitive image features that include color, texture, shape or the spatial location of the image elements [52][53][54]. Higher levels address object level features and rely on the reliable segmentation of target objects in the image [55][56][57]. More advanced ideas derive abstract attributes that characterize the segmented target objects [58][59]. Similarity usually refers to the distance measure defined in the extracted feature vector space, which includes Euclidean distance, geodesic distance, weighted sum of vector distances, Hausdorff, Mallows, etc. A survey of prototype CBIR systems can be referenced in [60].

CBIR from a retina image database is a newly developed research area. Current work mainly focuses on the retrieval and classification of diseased retinas for automated diagnosis and population study purposes. Developed algorithms for CBIR from retina image systems usually rely on screening of disease objects on retinas, which include mainly microaneurysms, hard exudates, drusen, etc. [61] proposed an algorithm to detect and count microaneurysms in angiographic images around the macula area using top-hat filter and shading correction. [62] used a multi-stage neural networks approach to detect microaneurysms. [63] used histogram-based approaches to decide an appropriate local threshold for localization of drusen. [64] and [65] used Gabor filters and wavelet frames for drusen detection, respectively. [66] presented a method to segment drusen using multi-level analysis starting from pixel to region, then area and image level. Candidate drusen pixels were selected at the pixel level and drusen detection results were refined based on detection rules when going into higher conceptual levels. A key challenge in disease object detection is the irregularity of shapes, sizes and counts. Formation of disease objects can take several different aspects like spotty, patchy or lacelike patterns, based on the gradation of diseases

[67]. Moreover, image interference like illumination condition, lens dust and image noise, like white nerve fibers found in retinas of younger patients, make the aforementioned detection approaches less reliable and increase the false detection rate. Other CBIR approaches do not rely on the domain specific features of diseased objects. Instead, they extract global features on images for image classification. [68] and [69] used the distribution of wavelet coefficients in each subband of the decomposition of retinal images as the signatures to characterize retinal health. [70] built a biometric system to give signatures to the human retina based on pattern analysis of the segmented retina blood vessels. CBIR is still a promising and immature research area on retinal image analysis. As with the common challenges in CBIR, research efforts are to be focused on semantic representation of retinal information with maximum retrieval throughput.

C. Summary of the Open Problems

Though the aforementioned research has successfully applied their algorithms in their area of study, several open problems are to be addressed or improved, which drive the direction for computer-aided analysis in its future development. Firstly, many of the existing work rely on high dimensional feature extraction for retinal object detection. Due to the "curse of dimensionality" problem, this complicates the process of learning the physical properties of retinal objects given the low number of trained data samples. It thus needs a succinct representation of the physical property of retinal object. Secondly, many algorithm designs are related to empirical parameter settings. As a result, their performances may vary for different types of images. As such, we are in pursuit of algorithms design which enables adaptive parameter adjustment. Thirdly, imaging factors in illumination conditions and field clarities compromise the performance of accurate target object detection. Continuing research study need to test and discuss their results on images under low illumination and incomplete field clarity conditions, which are often found in clinical practice. Fourthly, besides quantitative measurement of retinal features, extension of the study pushes the need for an analytical framework that bridges the gap between the low-level image segmentation and high-level retinal image analysis. Such high level studies will be related and extended to population statistics in age, race and health conditions. Finally, with the demand for retinal image retrieval on a large image database, we still lack of a systematic approach to feature extraction and weighting to optimize the retrieval throughput. Our following discussions will cover these open problems in more details and aim to address them by our proposed approaches.

CHAPTER III

MODELING OF RETINAL OBJECT ON RETINAL IMAGES

A. Overview of the Chapter

Key issues to purse in order to improve algorithmic performance are to explore the physical properties of retinal objects on retinal images and to relate these to our algorithm design and performance analysis. Among the many retinal objects on a typical retinal image, retina blood vessel (BV) network is the main and only main visible retinal object that covers the whole area on retinal image. Pattern of vascular network generation is the key pathological indicator of retinal health. And knowing its statistics is critical in many algorithmic designs and analyses for BV mapping. Besides, due to its fixed locations to other retinal objects such like the optic disc (OD) and macula-fovea (M-F) area, it is an important image cue to OD and M-F localization. As such, we propose the modeling of retina blood vessel in terms of its levels of generation on the whole retinal image.

The essence of the proposed anatomically-driven modeling technique of blood vessel network is based on observation of *generation levels* [1] of blood vessel branches, which capture the morphological relationships between BV segments at different locations. Figure 4 shows the different levels of vessel generations from small to large marked with different colors by medical doctors on a retinal image. In our work, we propose to use pattern analysis and statistical modeling techniques to characterize the properties of vessels at different generation levels, and generalize the statistics of vascular network pixels based on their levels of vessel generations.

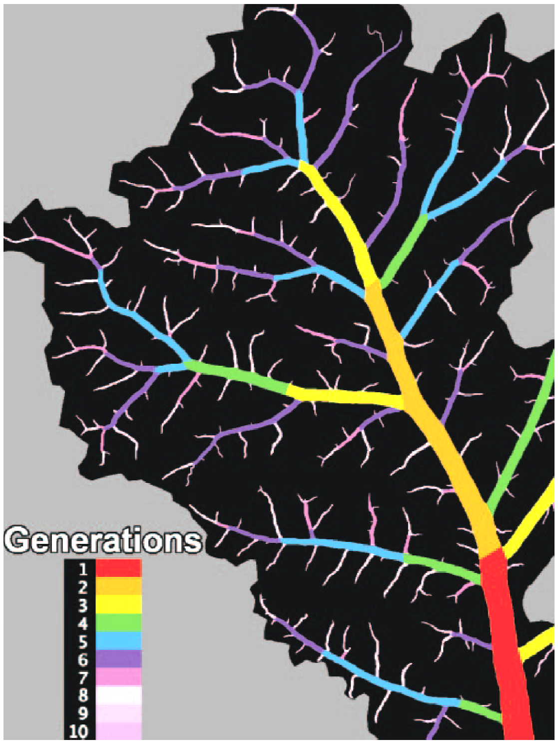

Figure 4: Vessel generation levels from small to large marked with different colors by medical doctors. (Source[1]: Courtesy of Dr.McKay).

Key idea behind our modeling technique originates from our observation that vessels at different generation levels in their widths, lengths and locations have different transitional properties in their boundaries. Figure 5 shows the intensity transitions of image pixels on a large and small BV cross section profile respectively. Comparing the two, it can be concluded that large BV segment has much wider and sharper boundary transition as compared with that of small BV segment, which is much narrower and much less sharper. As such, by exploring the difference in the boundary transition property for large and small BV segments, we approach designing a quantified measure for each pixel on the image so as to indicate if it is a BV or non-BV pixel, if it is on small or large BV segment and if it is near center-line or BV boundary. Given this quantified measure, further, by doing statistics on it for all the vessel pixels, we aim to characterize the count of vessels at different generation levels using statistical modeling technique.

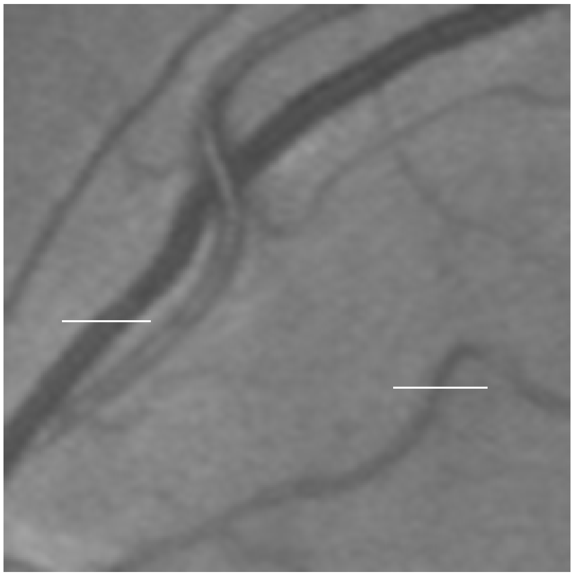

(a)

Figure 5: (a) Image pixels on cross section of large and small BV segment respectively. (b) Their corresponding intensity transitions.

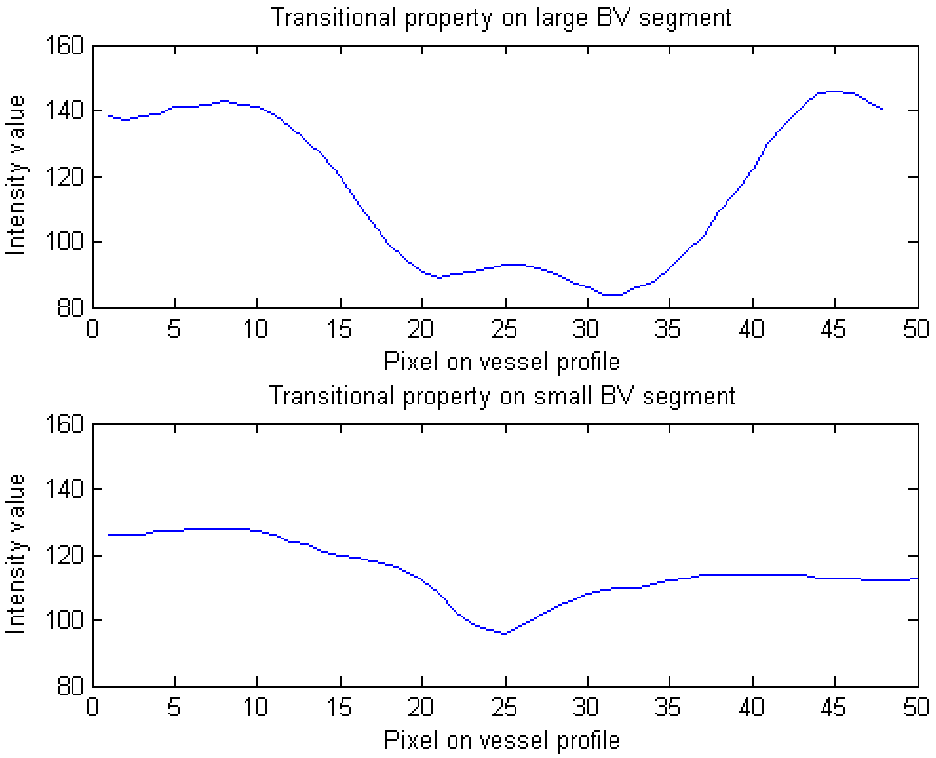

(b)

Figure 5 continued.

In achieving the goal, in the following sessions, we will address the following issues.

- A succinct representation of BV pixel.
- Quantified reasoning of BV pixels at different generation levels.
- Test of the model fitness against different factors.

B. Daisy Graph Representation of Image Pixels and Its Feature Descriptors

We first use a visualization technique called daisy graph representation developed in our previous work [71] to approach the physical property of image pixel. Daisy graph representation results from the technique of *rotational contrast transform (RCT)* [71] of image pixels. *RCT* is a contrast based filter, which, when applied to the green channel of a color retina image, obtains readings along different orientations. Here, the contrast of a pixel is defined as the ratio of its intensity against the average intensities of its surrounding area (the analysis window) [72][73]. Let p be a pixel with intensity I_p, based on the contrast definition in [74] , *RCT* of p along direction θ can be defined as:

$$C_p^{(\theta)} = \frac{I_p - \bar{I}_p^{(\theta)}}{\bar{I}_p^{(\theta)}},$$

where $\bar{I}_p^{(\theta)} = \frac{1}{r}\sum_{q \in N_p^{(\theta,r)}} I_q$, is the average intensity of $p's$ neighbors along direction θ , and *r* the distance span of the neighborhood. The neighborhood of p along direction θ with size *r* is defined as:

$$N_p^{(\theta,r)} = \{(x_q, y_q) | x_q = \lceil x_p + k\cos\theta \rceil, y_q = \lceil y_p + k\sin\theta \rceil,\ k = 1..r\}.$$

The neighborhood of p along direction θ is shown in Figure 6. The *RCT* vector of p, $C_p = \{C_p^{(\theta 1)}, C_p^{(\theta 2)}, C_p^{(\theta 3)} \ldots\}$, denotes the set of *RCT* values along different orientations. The number of orientations *N* for the *RCT*, is determined based on the angular resolution $\Delta\ \theta = \frac{360^\circ}{\mathrm{N}}$. For image resolution of 584x565 or similar, *r=21* and *N=32* can serve the purpose adequately.

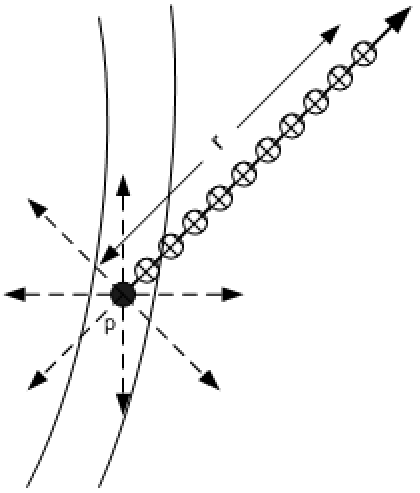

Figure 6: Illustration of the neighboring pixels of p along direction θ.

In a daisy graph, each $C_p^{(\theta i)}$ value is denoted by a directional arrow, whose length represents its magnitude, and positive and negative values are represented in the red and blue color respectively. A BV pixel has strong continuity along the BV flow, yet sharp negative contrast across the BV boundary. On its daisy graph, this observation translates into two negative lobes and a gap between them (see Figure 7 for the daisy graphs of four different BV pixels, which are the in-line BV pixels well within the BV boundary). The maximum of *RCT* values for a BV pixel occurs at the orientation which is perpendicular to the BV flow. Generally speaking, pixels on small, shallow BV (pixel 3 and 4) have small magnitudes than their large counterparts (pixel 1 and 2), and therefore also smaller lobes on their daisy graphs. In Figure 7, the unit in daisy graphs of pixels 1 and 2 are 0.5, yet that of pixels 3 and 4 are 0.1 and 0.2, respectively.

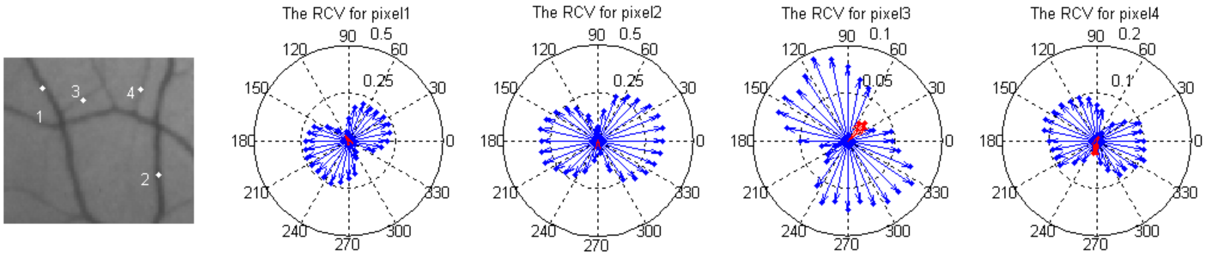

Figure 7: Daisy graphs of four different BV pixels, which are well within the BV boundary.

Using the daisy graph representation, we demonstrate the transitional properties of pixels when moving from in-BV, BV boundary to non-BV area. The lobe patterns in daisy graphs for sixteen pixels which are marked across the BV in Figure 8(a) from left to right are given in Figure 8(b), in the left to right, top and down order. BV pixels numbered 9-14 have strong negative *RCT* values (blue color), and the symmetry of two lobes for a daisy graph increases as the pixel moves to the center of the BV. An abrupt change in the daisy graph pattern occurs when the pixel moves out of the BV boundary, e.g., pixels 8 and 15, which do not have symmetric negative RCT daisy graph pattern any longer.

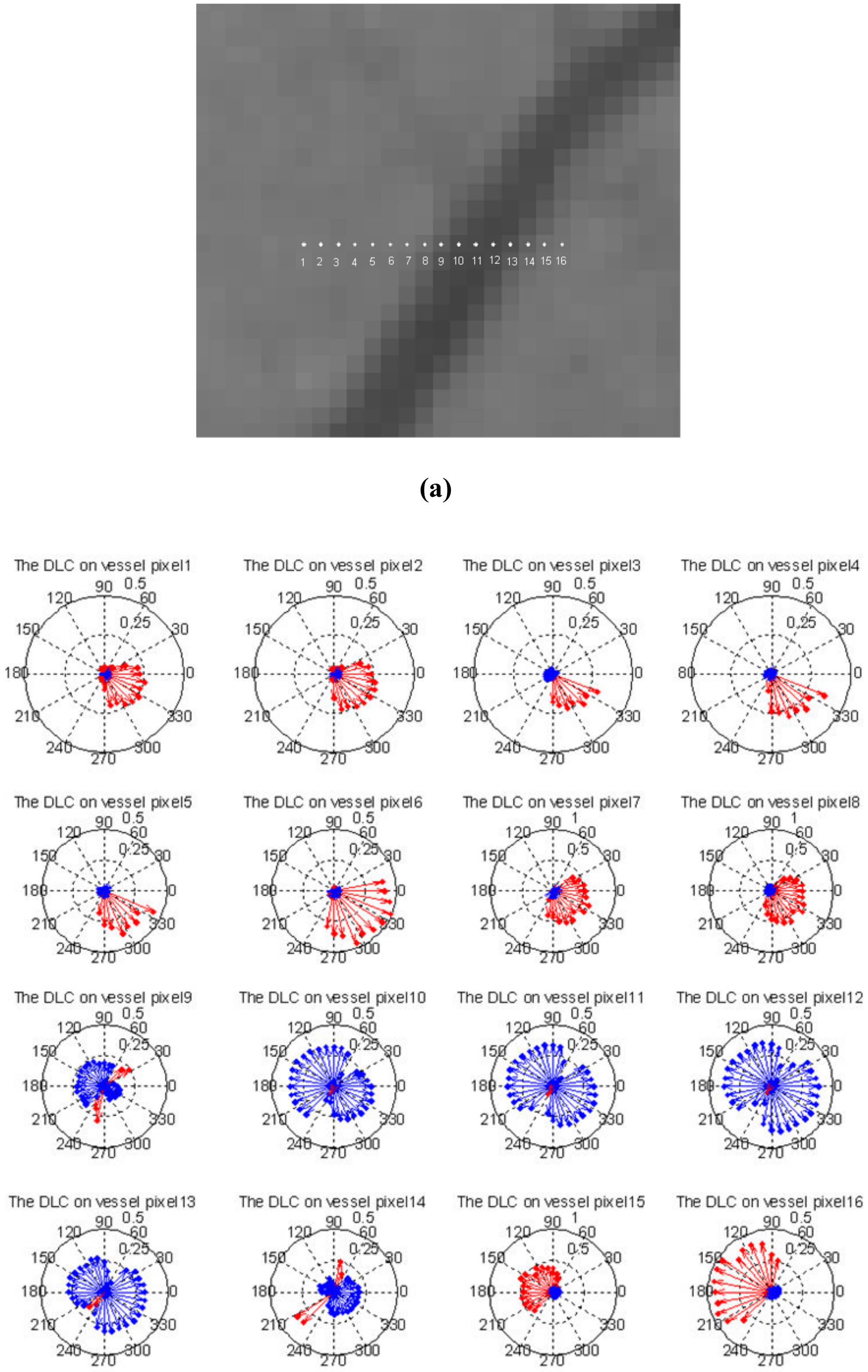

(a)

(b)

Figure 8: (a) Sixteen pixels along the cross section of a BV. (b) Daisy graphs of the sixteen pixels.

Daisy graph representation provides us a qualitative representation of the morphological property of image pixel. To explore the relationship between shapes of daisy graph patterns with respect to BV, we propose two feature descriptors of daisy graphs, *energies* and *symmetry-difference*, for pattern and statistics analysis of BV, BV boundary, and the background pixels. Given the designed feature descriptors, our goal is that differentiation between BV and non-BV pixels, BV pixel on small and large BV branches and center-line BV and BV boundary pixels can all be quantified.

For a pixel *p*, its energy descriptor E_p and symmetry-difference descriptor S_p are defined as follows. The energy E_p is the sum of *RCT* values of image pixel along different directions.

$$E_p = \sum_{m=0}^{N-1} C_p^{(\theta_m)}.$$

where $C_p^{(\theta_m)}$ is the *RCT* values along θ_m, $\theta_m = 2\pi \frac{m}{N}$. BV pixels have lower intensity than the background, and thus in most cases BV pixels have negative values for the sum of all *RCT* elements.

The symmetry-difference S_p is the sum of the symmetry difference between a *RCT* value along an orientation and that of the opposite direction.

$$S_p = \frac{\sum_{m=0}^{\frac{N}{2}-1} \left| C_p^{(\theta_m)} - C_p^{\left(\theta_{m+\frac{N}{2}}\right)} \right| / |\overline{C_p}|}{|Max(C_p) - Min(C_p)|},$$

where $C_p^{(\theta_m)}$ and $C_p^{\left(\theta_{m+\frac{N}{2}}\right)}$ are the *RCT* values at opposite directions along θ_m. $\overline{C_p}$ is the mean of contrast magnitudes. $|Max(C_p) - Min(C_p)|$ denotes the maximal variation in the contrast along different directions. By its design, the numerator part denotes the symmetry property of the lobe pattern on a daisy graph, so that the more symmetric the lobe pattern is, the smaller the value of the numerator part is. At the same time, the denominator part denotes the maximum difference of contrasts for an image pixel against different directions. As such, vessel pixels on large BV segments have sharp contrast against their boundary areas while low contrast along the vessel direction. As a result, the value of $|Max(C_p) - Min(C_p)|$ is large. On the contrary, the term value for small BV segment is much smaller, due to their much shallower contrast against boundary areas. As a whole, S_p value increases as we move from the center toward the boundary of a BV, from large to small BV segment, with the decrease in the degree of symmetry of the two lobes of the daisy graph and decrease in contrast difference.

Proposition of S_p descriptor, therefore, provides a method so that we can establish an order of BV pixels at different locations on vascular network. For image pixels of same object types, their (E_p, S_p) values tend to have similar properties, and therefore when they are projected to a new feature space $\boldsymbol{F}$, they tend to cluster together. As a result, we may explore the statistical properties for BV and BV boundary pixels to establish more reliable relationships between them, than independent analysis of point observations.

C. Statistical Properties of BV and BV Boundary Pixels in *F*

We use the twenty hand-labeled images in DRIVE [3] by two human experts as the reference sets to explore the statistical properties of different types of image pixels on $\boldsymbol{F}$. The two hand-labeled BV maps (for each image) have some subtle differences, especially for BV boundaries and small/shallow vessels. In order to evaluate the robustness of statistical distribution against different detection sensitivity, we will use the double-marked BV maps, i.e., BV pixels marked by both experts and single-marked BV maps, i.e., BV pixels marked only by one expert, for our studies. Non-BV pixels are those both experts recognized as non-

BVs. To explore boundary properties of BV, we also obtain the BV boundary maps from both reference sets. Here, BV boundary pixels are generated by applying the Sobel edge detector to BV pixel maps. For an original retinal image in DRIVE [3] shown in Figure 9(a), its two hand-labeled BV maps are given in Figure 9 (b) and (c), respectively. Their “single-marked” BV map is given in Figure 9 (d), and the BV boundaries for the two hand-labeled BV maps are given in Figure 9 (e) and (f), respectively.

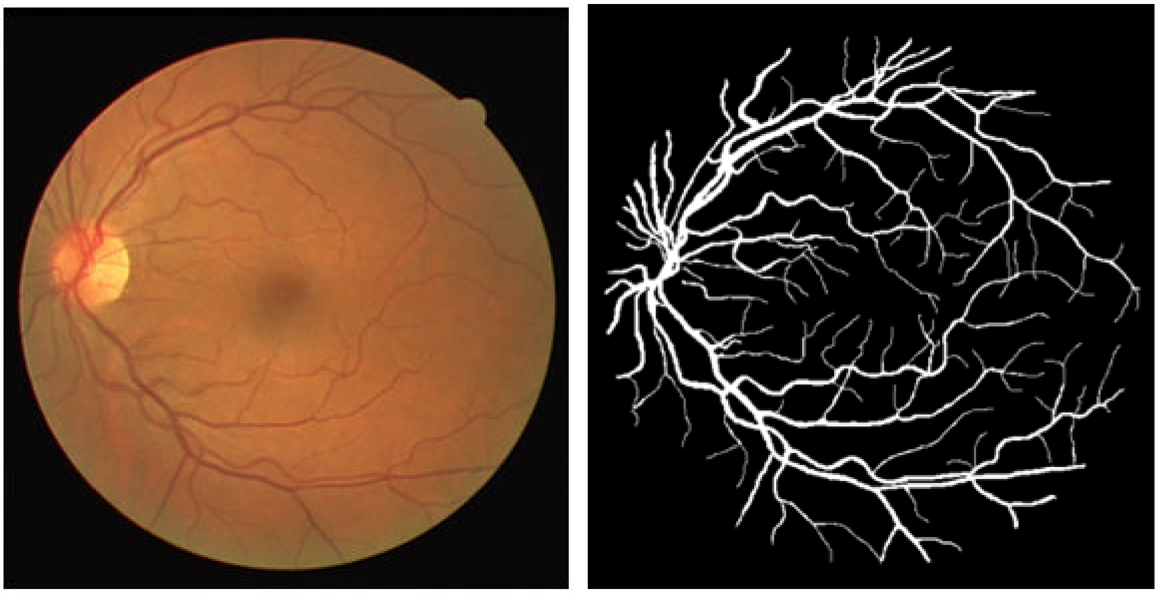

(a) **(b)**

Figure 9: (a) Original retinal image (im01 from DRIVE), its two hand-labeled BV maps are given in (b) and (c), respectively. Their “single-marked” BV map is given in (d), and the BV boundaries for the two hand-labeled BV maps are given in (e) and (f), respectively.

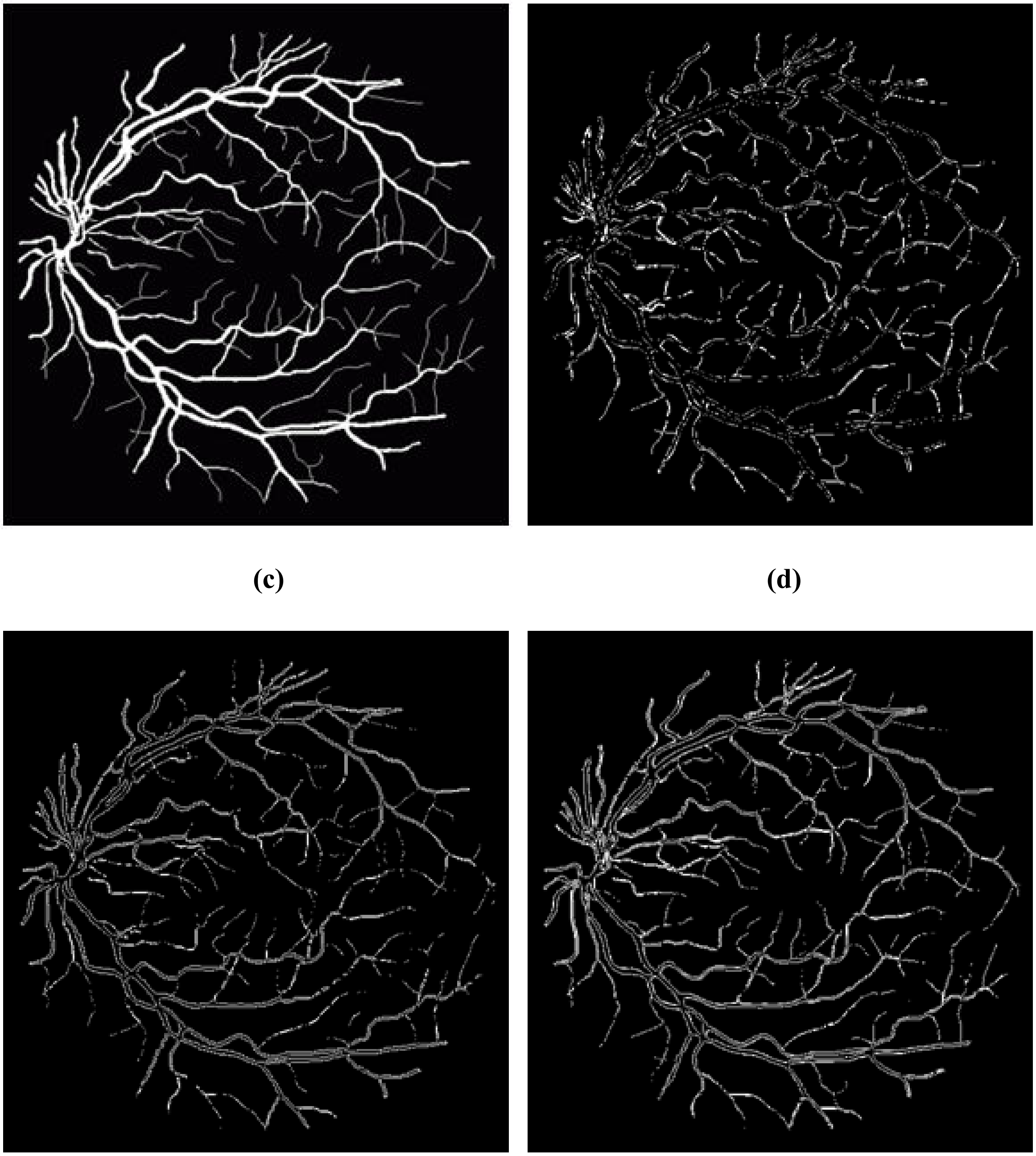

(c) **(d)**

(e) **(f)**

Figure 9 continued.

We then make some simple observations on the clustering properties of single-marked and double-marked BV pixels, non-BV pixels, and BV boundary pixels in ***F***, and they are plotted in Figure 10. The ratio between single-marked to double-marked BV pixels is roughly

1:2 for the 20 reference images in DRIVE. We note that the color code (to represent range of magnitudes) in these figures are based on relative scale, and the numerical ranges for each figure are labeled at its colorbar at the side. Generally speaking, double-marked BV pixels are most tightly clustered onto the area in ***F*** with small S_p and negative E_p values (in Figure 10 (a)). On the other hand, non-BV pixels are clustered onto area in ***F*** of positive E_p values or negative E_p values but with large S_p values (see Figure 10 (b)) and its cluster center is far apart from that of "double-marked" BV pixel area. S_p values of both the BV boundary pixels (see Figure 10 (c) and Figure 10 (d)) have similar clustering behavior with that of "double-marked" BV pixels. Their cluster centers are close to that of the "double-marked" BV pixels, while a portion of their pixels would have positive E_p values. S_p values of their outer-range pixels would overlap with that of non-BV pixels area. It is also noted that S_p values of "single-marked" BV pixels in Figure 10 (e) are relatively more scattered as compared with that of "double-marked" BV pixels and BV boundaries. Similarity in the outer range area of Figure 10 (e) with that of (c) and (d), suggests that most "single-marked" BV pixels are resulted from different interpretations of BV boundary by two human experts.

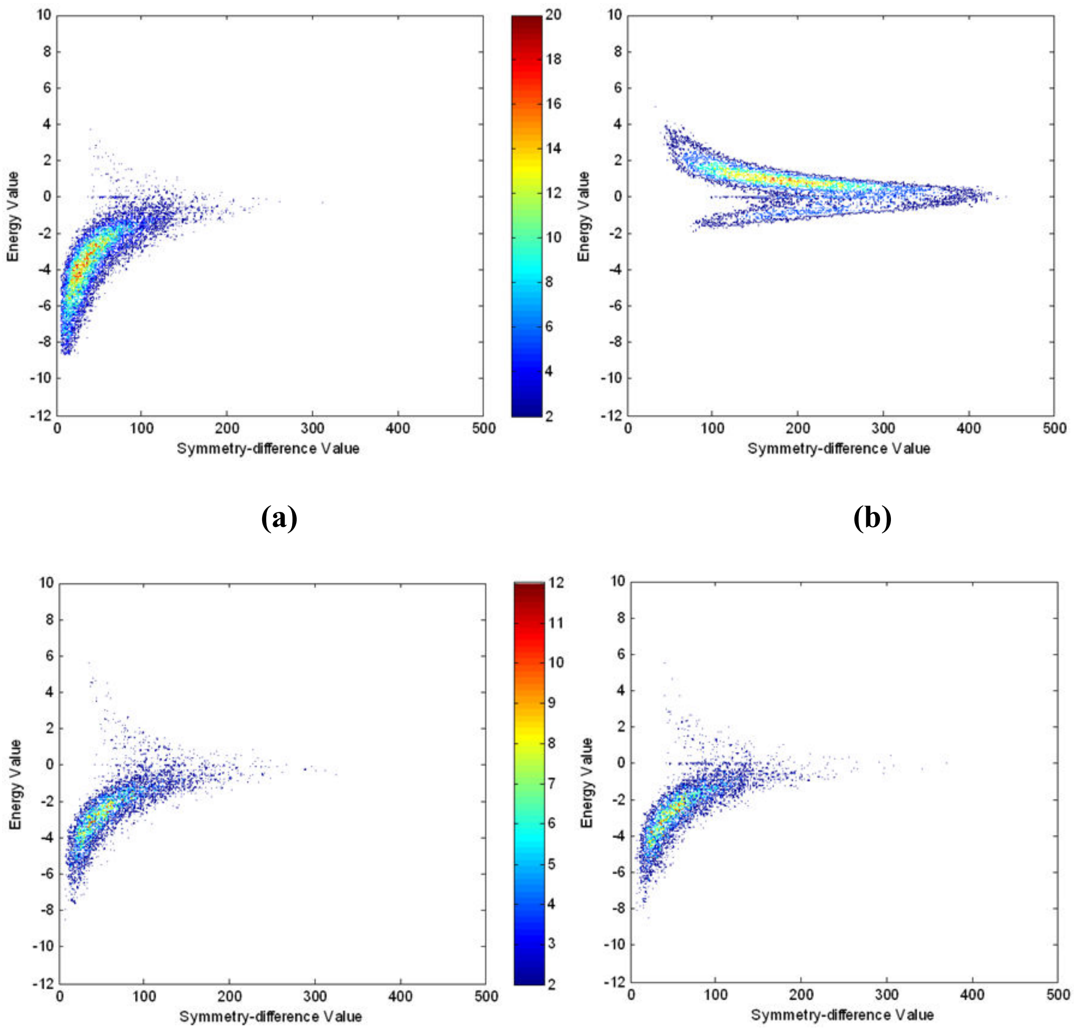

(a) **(b)**

(c) **(d)**

Figure 10: Clustering behavior of different types of image pixels. (a) "double-marked" BV pixels; (b) non-BV pixels; (c) and (d) the BV boundary pixels for two hand labeled BVs; (e) "single-marked" BV pixels. Note that the colorbars for the five figures have different ranges.

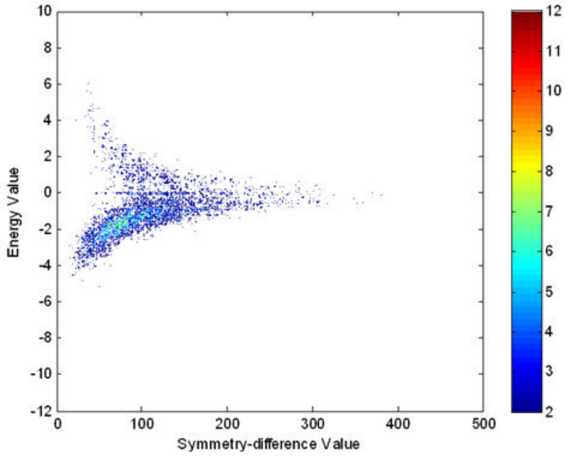

(e)

Figure 10 continued.

Next, we will apply rigorous statistical analysis on distributions for BV and BV boundary pixels and explore their relationships on ***F*** along E_p and S_p descriptors.

1. The E_p Descriptor for Different Types of Image Pixels

We do simple statistics to calculate the ratio of BV (both "double-marked" and "single-marked"), its boundary pixels, and non-BV pixels having negative E_p values for the two hand-labeled BV maps of the 20 images in DRIVE. On average, over 94% (68%) of the "double-marked" (single-marked) BV pixels have negative E_p values. For the first (second) reference set, 80% (84%) of the BV boundary pixels have negative E_p values. On the contrary, only 27% of the non-BV pixels have negative E_p values. The result suggests that a threshold near the zero-crossing of E_p values is a reasonable first indicator to eliminate a large number of non-BV pixels. We can control the false negative value by adjusting the threshold on the E_p. Any potentially false positive BV pixels would then be eliminated by subsequent analysis of their S_p values.

We further look into some examples (see Figure 11) of hand-labeled BV pixels that have positive E_p values. Figure 11 (a) is the original retina image cropped from Figure 11 (a), and Figure 11 (b) its corresponding hand-labeled BV maps (marked in white color). The blue and the red colored pixels denote the "double-marked" BV and "single-marked" BV pixels (mainly BV boundary pixels) that have positive E_p values, respectively. Those BV pixels with positive E_p values appear to be the result of either human interpolation or extrapolation of small and shallow BV boundaries based on continuity of BV flows, or filling the hollow area within the BV due to the light reflection. The differences in the interpolation or extrapolation outcomes reflect the personal judgments of the human experts. Knowing that the number of BV pixels with positive E_p values is very small, and most of them are located at the smallest BVs, we will take the zero cross point of E_p as a screening threshold to eliminate non-BV pixels from further analysis of BV pixels and BV boundaries in the subsequent discussions. We denote the area in F that has negative E_p values as $F_{neg\text{-}E}$.

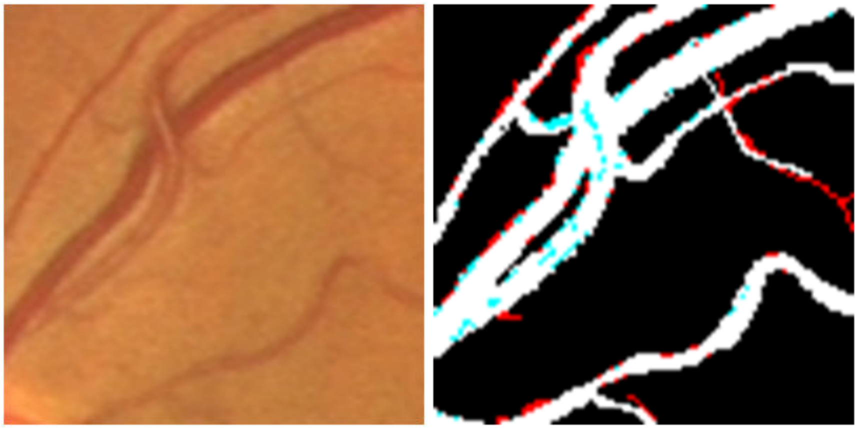

(a) **(b)**

Figure 11: (a) Cropped images from Figure 9(a). (b) BV pixels have positive E_p values. The blue and the red colored pixels denote the "double-marked" BV and "single-marked" BV pixels (mainly BV boundary pixels) that have positive E_p values, respectively.

2. The S_p Descriptor for Different Types of Image Pixels

Next, we discuss characteristics of different types of pixels along the S_p descriptor for the area of $F_{neg\text{-}E}$. Recall that from subsection B, BV pixels of similar locations on BV network have similar values in S_p. As such, S_p value represents a form of pixel type ordering, e.g., in-BV pixels would have the smaller S_p value than those located at BV boundaries. Small and shallow BVs have even larger S_p values. The anatomic study on human retina suggests that BV growth can be modeled as generation levels based on their widths, lengths and locations. Under normal conditions, their pattern of generation levels, such like BV width ratios, artery to vein ratio would conform to certain proportional laws, such as that described by fractal dimensions[75][76], etc.

The proportional law of BV growth pattern in terms of levels of vessel generations is also reflected in the distribution of S_p values in $F_{neg\text{-}E}$. Despite the differences between the two hand-labeled maps, we observe that the statistical behaviors of the S_p values for BV pixels on different retinal images exhibit highly consistent skewed shape on their histogram plots, as the blue curve example depicted in Figure 12 (a) and (b).

The majority of BV pixels have small S_p values on the histogram plot, and they represent pixels located around BV center-lines on the original image. The tail portion of the plot denotes BV pixels which have relatively larger S_p values. They represent the small number of small and shallow BV pixels. It is interesting to note that the histogram plot of S_p values for BV boundary pixels exhibits a very similar skewed shape (see the red plot in Figure 12 (a) and (b)) as that of the BV pixels. This is because boundary pixels located at large (small) BV trunks have smaller (larger) S_p values, and there are more boundary BV pixels for large BV segments than that of smaller ones. Comparing the two histogram plots for BV and BV boundary pixels, we observe that, despite the difference in their peak values, both curves closely resemble each other in their shape transitions. The plot of the BV boundary is enclosed within that of the BV and both plots tend to reach their peaks concurrently. In addition, when BV width is reduced to 1-2 pixels, both the BV boundary and BV refers to the same pixel due to the limit of image resolution. As a result, the two curves converge at their tails.

We use statistical model fitting techniques [77] [78] to analyze the two distribution plots. It is shown that both the BV (blue color) and BV-boundary (red color) histogram plots can be fitted to the lognormal distribution functions. Fitness of the lognormal distribution for the two histograms is given in the subsection 3.4, and the fitted distributions are marked in the green and yellow colors in Figure 12 (a) and (b), respectively, for the two histograms. The lognormal distribution has long been studied in population statistics in biology and life sciences [79][80]. In our study, the fitted lognormal distribution offers a simple yet efficient tool in analyzing the statistical properties of BV and BV boundary pixels, and the relationship between the two types of pixels along S_p. First, we exploit six important statistical measures {Ts1 … Ts6} [77] on these lognormal distribution curves,

- *Ts1: mode (the point of global maximum of the point density function of lognormal distribution),*
- *Ts2: median (the point where cumulative distribution function amounts to 0.5),*
- *Ts3: mean,*
- *Ts4: 1σ upper bound,*
- *Ts5: 2σ upper bound,*
- *Ts6: 3σ upper bound.*

Important statistical information can be inferred from these measures, such as the proportion of the area covered under the curve, curve shape, etc.

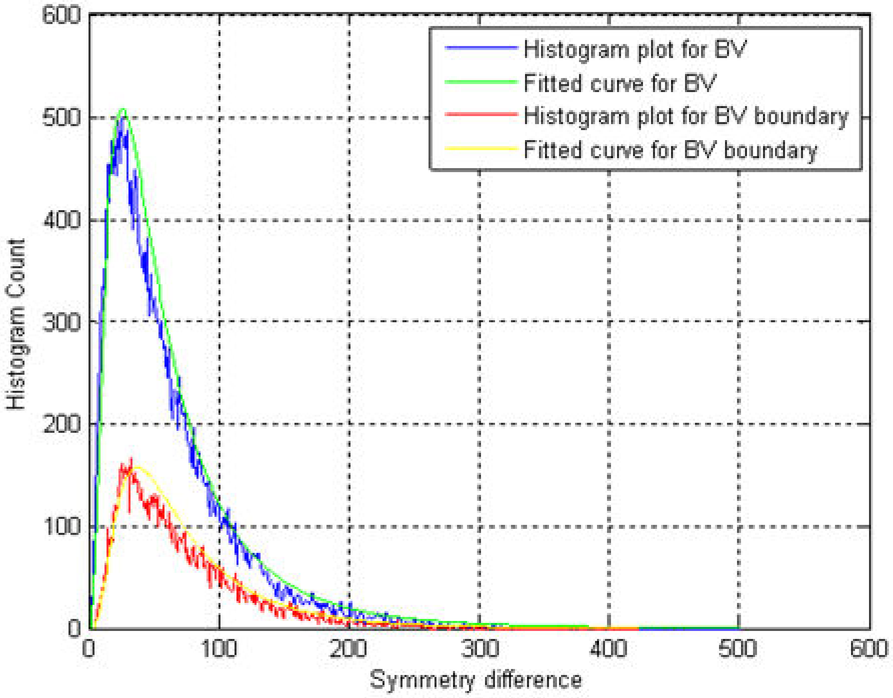

(a)

Figure 12: (a) and (b) are the distributions of BV and BV boundary pixels along S_p descriptors based on two hand-labeled results respectively. The blue and the red curves denote the histograms for the S_p values of BV and BV boundary pixels respectively. The green and yellow curves denote their corresponding fitted lognormal distribution curves.

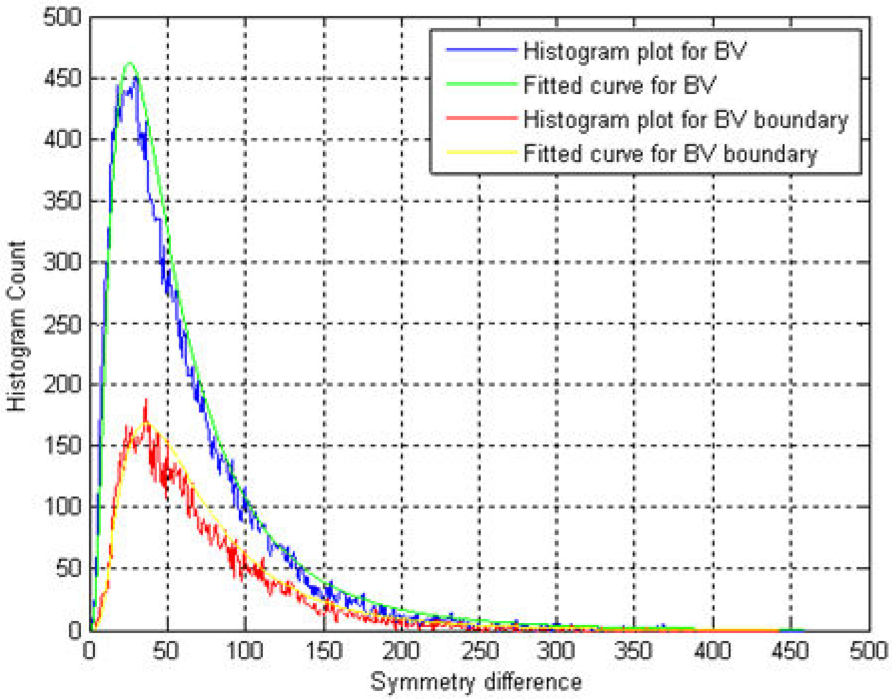

(b)

Figure 12 continued.

Let *{Ts_BV}* and *{Ts_Boundary}* respectively denote $\{T_{s1}, T_{s2}, T_{s3}, T_{s4}, T_{s5}, T_{s6}\}$ for fitted distribution curves of BV and BV boundary pixels. We then compare the paired measures of $T_{s1}, T_{s2} \ldots T_{s6}$ from *{Ts_BV}* and *{Ts_Boundary}* sets for all the images in DRIVE, and the results are shown in Figure 13, where the "x" axis refers to the values from *{Ts_BV}* and the "y" axis from *{Ts_Boundary}*. We observe that the paired measures from T_{s1} to T_{s5} values are highly concentrated along the "y=x" line. Only a few pairs of T_{s6} deviate from each other slightly. The result suggests that there exists a strong and linear correlation between the distribution of the statistical behavior of BV and its boundary pixels. As a result, with high statistics confidence we can use *{Ts_Boundary}* set to predict *{Ts_BV}* set values. It is the basis for us to use *{Ts_Boundary}* to develop the statistical behavior of BV pixels on F in the subsequent discussions.

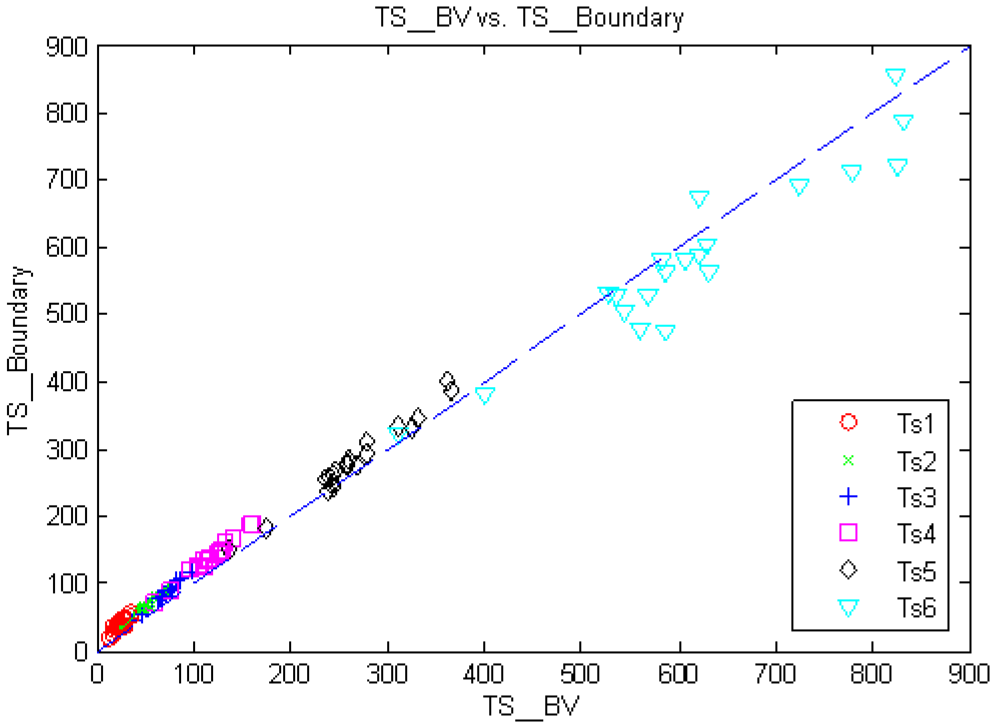

(a)

Figure 13: (a) and (b) are the *{Ts_BV}* and *{Ts_Boundary}* values derived from the two hand-labeled results respectively for all images in DRIVE. On both plots, the "x" axis refers to the *Ts1* to *Ts6* values from *{Ts_BV}* and the "y" axis from *{Ts_Boundary}*. Paired measures from the *{Ts_BV}* and *{Ts_Boundary}* sets are highly concentrated along the diagonal line on both plots.

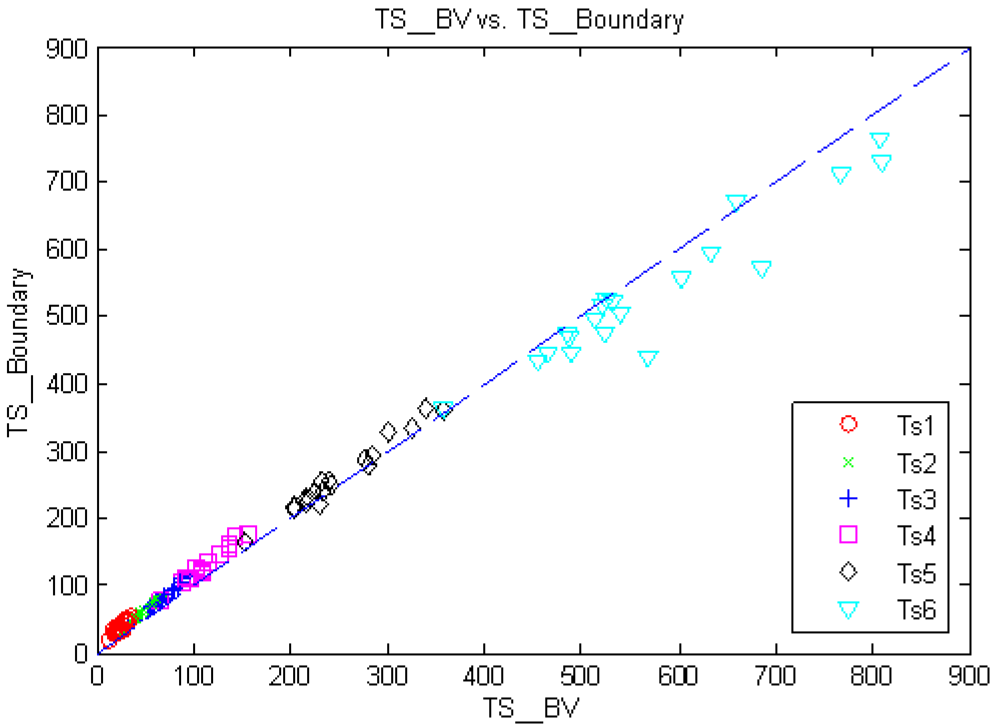

(b)

Figure 13 continued.

Next, we test the robustness of the derived *{Ts_Boundary}* values against different hand-labeled results by comparing their paired measures derived from the two reference sets for images in DRIVE in Figure 14. Similarly, the pairs of *{Ts_Boundary}* values concentrate along the diagonal line, except for the slightly dispersed pairs of T_{s6} values. The discrepancy in T_{s6} pairs reflects the difference in the tail regions on the two derived lognormal distribution curves, which is mainly due to the human's preferences in boundary delineations. In the following discussions, we may show that T_{s6} refers to the very shallow BV pixels, whose selection is more subjective. Except for the shallow boundary pixels, *{Ts_Boundary}* values are statistically stable against different hand-labeled sets. We could take any of the two *{Ts_Boundary}* sets to demonstrate its effect on BV pixel clustering.

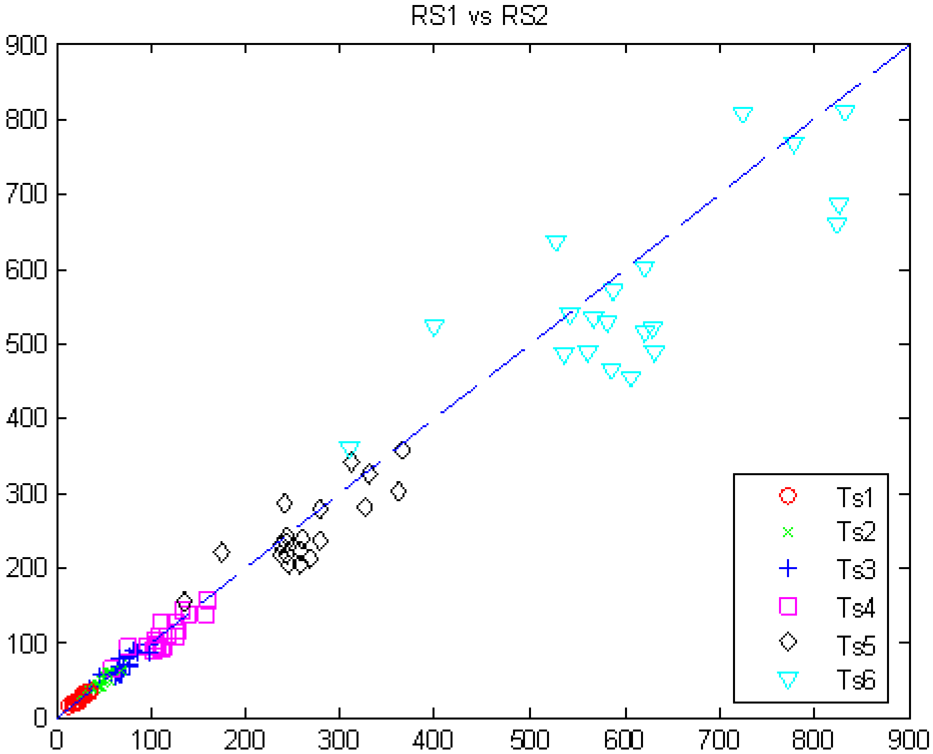

Figure 14: Paired values of *{Ts_Boundary}* values derived from two hand-labeled sets for all images in DRIVE. "x" and "y" axes denote the *{Ts_Boundary}*values from the two hand-labeled reference sets "RS1" and "RS2" respectively. The paired values are highly concentrated along the diagonal line.

Finally, we show the clustering behavior of image pixels in the $F_{neg\text{-}E}$ based on setting of different threshold values for *{Ts_Boundary}* of the S_p descriptor, and show the statistics of the averaged coverage ratio of BV (both "double-marked" and "single-marked") and the non-BV pixels for images in DRIVE. In Figure 15, (a) shows the calculated ratio with respect to the total number of pixels for each pixel type in $F_{neg\text{-}E}$, while (b) shows a similar ratio measure for F. We use the red and blue lines to represent the covered ratio of "double-marked" and "single-marked" BV pixels respectively, and the green color line for the non-BV pixels. The error bar on the curve is calculated by one standard deviation for each calculated covered ratio. In summary, when $S_p \leq T_{s1}$, only "double-marked" BV pixels are included. When the threshold is increased to T_{s4}, over 90% of "double-marked" BVs, over 50% of the "single-marked" BVs, and a very small fraction of non-BV pixels (ratio is less than 0.08 in $F_{neg\text{-}E}$ and less than 0.04 in F) are covered. When the threshold is increased to T_{s5}, almost all BV pixels (more than ratio of 0.95) in $F_{neg\text{-}E}$ are included, and more non-BV pixels are also inevitably included. When the threshold is increased to $S_p = T_{s6}$, the included ratio non-BV pixels would increase to 0.6 and that of BV turn to 1 in $F_{neg\text{-}E}$. A close look at these calculated ratios under different values in *{Ts_Boundary}* shows that they closely conform to the theoretical ratios of the covered area under the lognormal distribution curve, which in turn, demonstrates fitness of the lognormal distribution.

We further investigate characteristics of error bars of these statistic measures against different images. We observe that the error bar for the "double-marked" BVs is small under all *{Ts_Boundary}* values while that of the "single-marked" BVs is relatively a slightly larger. This reflects that fact that the statistical behavior of the fitted model for "double-marked" BV is highly consistent among different images while that of "single-marked" is less due to human preferences. Further, the error bar of the non-BVs would become even larger when S_p moves to T_{s5} and T_{s6}, which reflects the different physical properties of the retina background among different images.

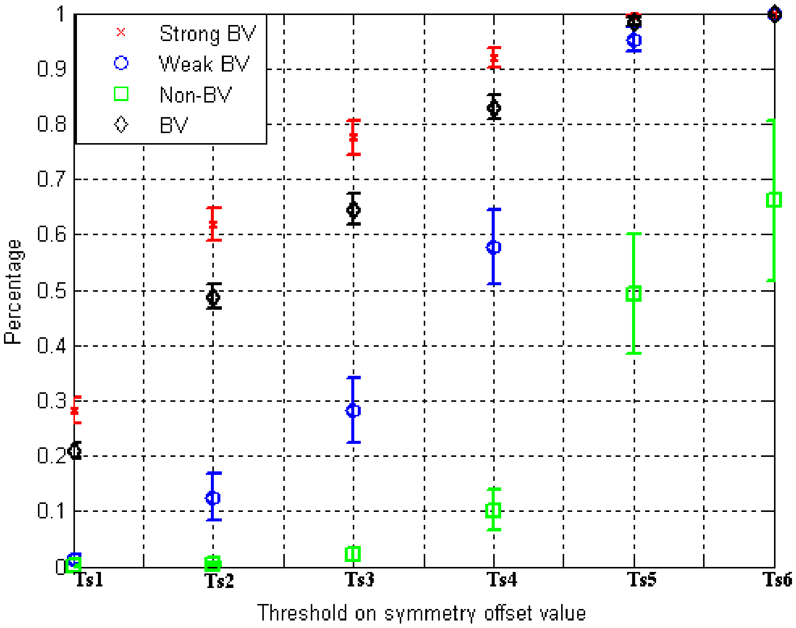

(a)

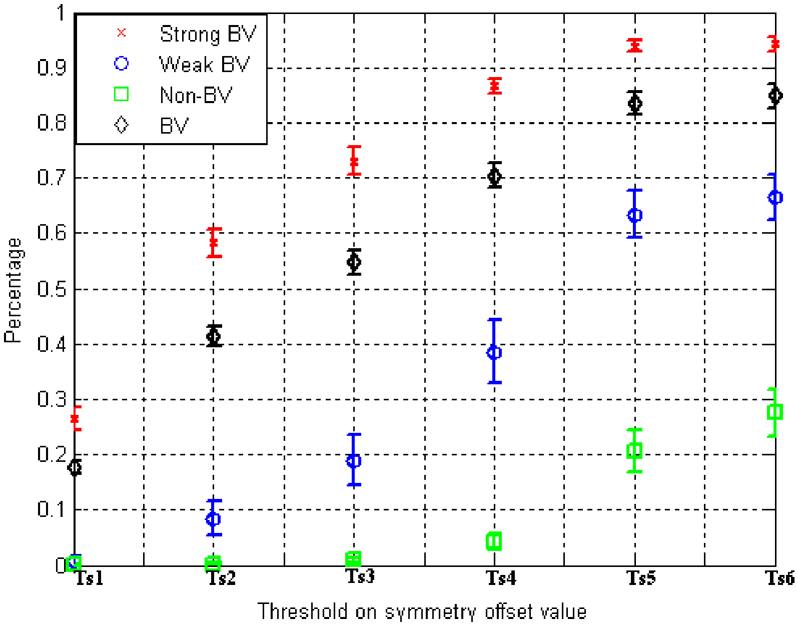

(b)

Figure 15: Statistics on the average portion of BV (both "double-marked" and "single-marked") and non-BV pixels (for images in DRIVE) under different thresholds using S_p values of *{Ts_Boundary}*. The result in (a) ((b))is calculated using the total number of pixels for each pixel type in $F_{neg\text{-}E}$ (F) as the denominator. The red (blue) color represents "double-marked" ("single-marked") BV pixels, and the green represents non-BV pixels. The error bar is calculated by one standard deviation for each calculated covered ratio.

In Figure 16, we show graphically BV and non-BV pixels being captured by using different S_p threshold values in a *{Ts_Boundary}* set. In these figures, the BV pixel map for a hand-labeled reference is marked in the white color. The red and blue colors denote the BV and non-BV pixels being covered for different threshold values. It is noted from Figure 16 (a) to Figure 16 (f), "sliding" the threshold on S_p value from "left" to "right" (T_{s1} to T_{s6}) leads to coverage of set of pixels which expand from ridges to boundaries of BVs. The "ridge to edge" region growth appeared to be highly consistent for large BVs, and most small BVs are included simultaneously when the growth reaches the boundary of large BVs. As expected, when the growth approaches BV boundaries, some non-BV pixels would also be included. When S_p value becomes larger than T_{s5}, nearly all BV pixels are included and only non-BV pixels would be increased. Comparing Figure 16 (e) with Figure 16 (f), it is noted that no more BV pixels except for the very shallow small BVs would be included when increasing S_p from T_{s5} to T_{s6}.

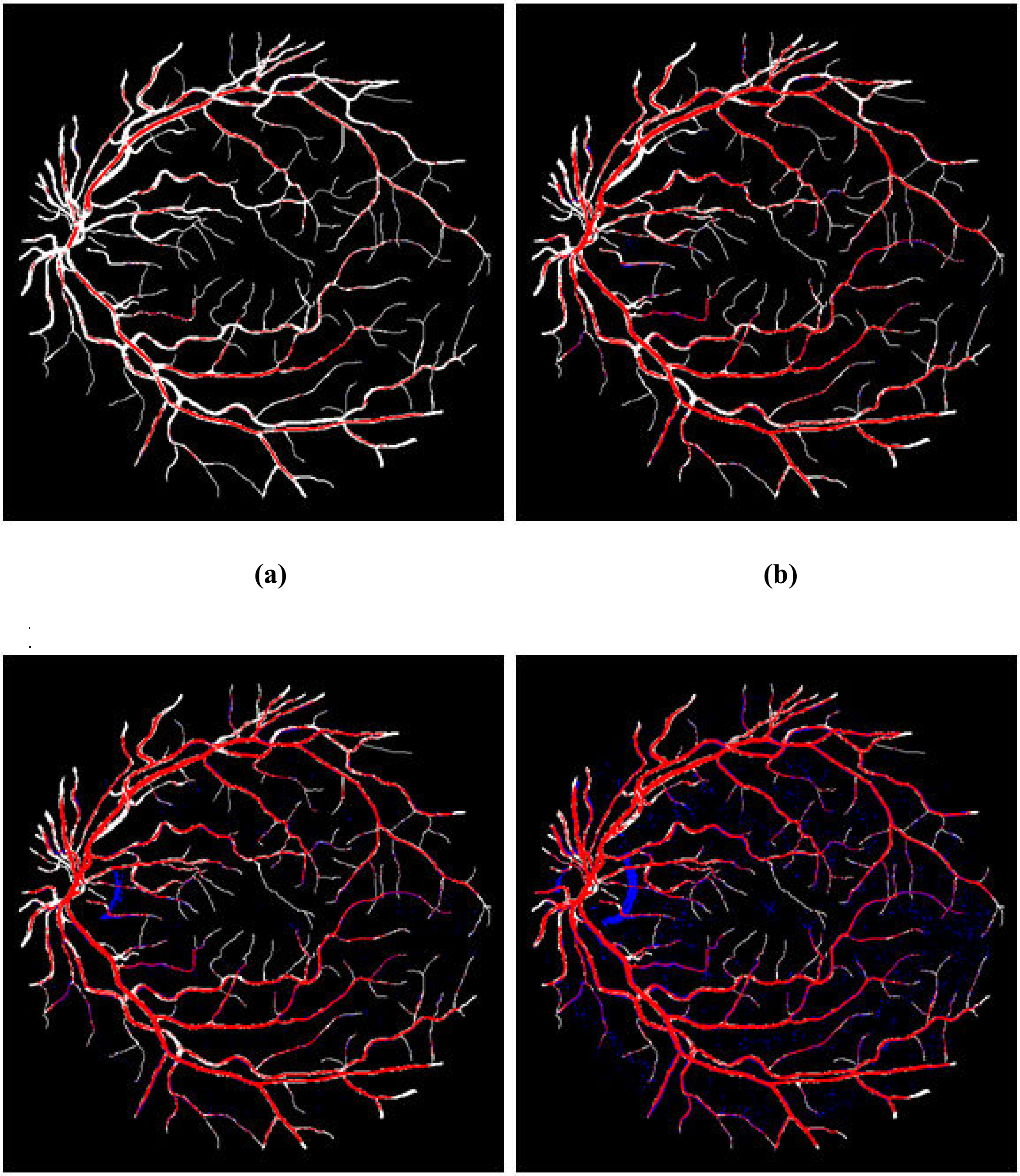

(a) (b)

(c) (d)

Figure 16: (a)-(f) refer to inclusion of BV and non-BV pixels under different threshold values in *{Ts_Boundary}* set from *Ts1* to *Ts6*. On each image, the white color denotes the reference from one hand-labeled result. The red and blue colors denote the included BV and non-BV pixels under different thresholds.

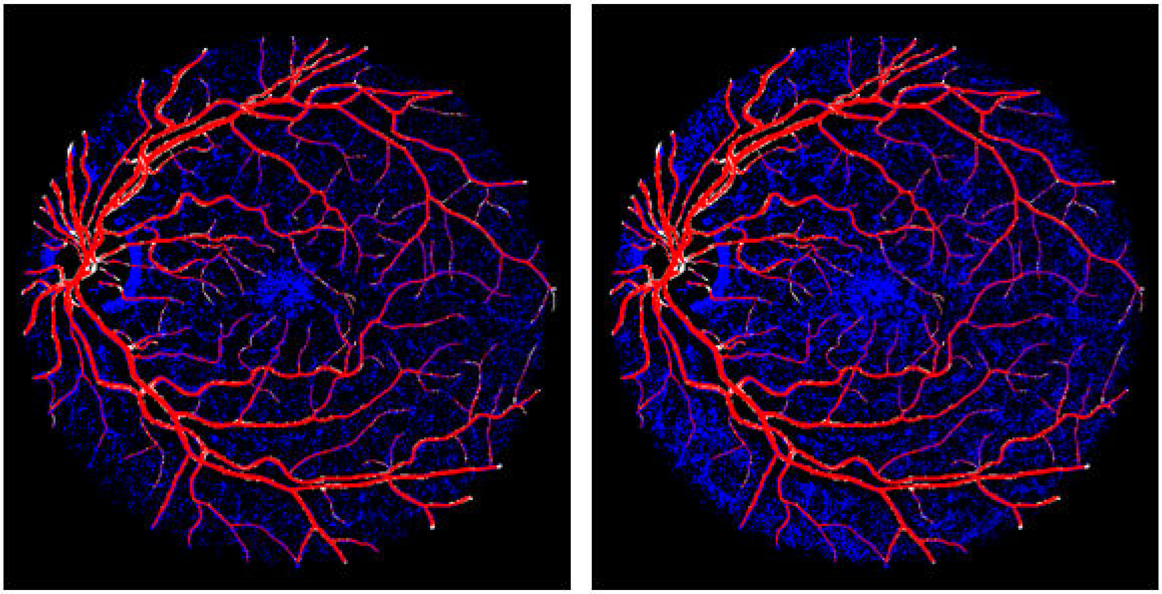

(e) (f)

Figure 16 continued.

D. Fitness of the Statistical Model

In this session, we show the fitness of the lognormal distribution (green and yellow curves respectively in Figure 12) to the histograms of S_p values of BV and its boundary pixels in $F_{neg\text{-}E}$.

The probability density function of the lognormal distribution has the form of

$$f(x;\mu,\sigma) = \frac{1}{x\sqrt{2\pi\sigma^2}} e^{\left(-\frac{(\ln x-\mu)^2}{2\sigma^2}\right)}$$

for x > 0, where μ and σ are the mean and standard deviation of the logarithm of x, i.e., ln(x), which by definition is normally distributed. Here, x represents S_p value of BV or BV boundary pixels in Figure 17 (a) and (b) respectively. To fit the data set, we need to estimate μ and σ, based on the observed datasets. Using the maximum likelihood criterion, we get

$$\hat{\mu}=\frac{1}{n}\sum_k lnX_k\ ,\ \hat{\sigma}^2 = \frac{1}{n}\sum_k (lnX_k - \hat{\mu})^2$$

where, X_k is the observed S_p value for each BV (or BV boundary) pixel and n the total number of hand-labeled BV (or resulted BV boundary pixels).

Theoretically, to demonstrate the fitness of the curve model to the empirical histogram plots, we can take a rigorous statistical hypothesis test of the normality of ln(x) (with the estimated $\hat{\mu}$ and $\hat{\sigma}$) using the Kolmogorov-Smirnov Test [77]. We performed the normality test of ln(x) by the Matlab library function "kstest.m", using 1000 randomly sampled pixels for BV and BV boundary respectively as the dataset. With the significance level of 0.05, we perform a one-sided test on the sample data. The null hypothesis for the Kolmogorov-Smirnov test is that $(\ln(x) - \hat{\mu}) / \hat{\sigma}$ has a standard normal distribution. The alternative is that it does not have that distribution. The null hypotheses on the sample data are all tested to be 0 for both BV and BV boundary pixels, which indicates that we cannot reject the hypothesis if the test is significant at the 5% level. By visual inspection, plots in Figure 17 also show that empirical curves (of the normality tests) for both BV (Figure 17 (a)) and BV boundary (Figure 17 (b)) closely match the normal distribution. A close examination on the original image areas that correspond to the unmatched area (mostly located near the tail) in Figure 17 (a), shows that they were mostly due to subjective human interpretation of the BV boundaries of small BVs. The testing results are consistent for all the images in both STARE and DRIVE. One thing worth noting is that in performing the test, we choose only a relatively small portion of samples (1000 pixels) from the large number of BV or BV boundary pixels (estimated over 20,000 and 8,000 pixels, respectively, for 700x605, 584x565 or similar images) for model fitting. The reason is to avoid the oversampling problem. Otherwise, when the sample set is too large, the Kolmogorov-Smirnov Test will reject the null hypothesis, because of the “fallacy of p-value” issue [77] [78], even though the empirical CDF plot closely matches that of the normal distribution.

In practice, however, rigorous proof of the fitness of data to lognormal distribution is not required or even needed for its practical usage in modeling fitting. Lognormal distribution curve model with its estimated $\hat{\mu}$ and $\hat{\sigma}$ provides us a closed form in calculating the cumulative distribution function (CDF) of the function. As such, to test the fitness of the model, we can compare the empirical and its corresponding standard quantile values on CDF to determine the fitness of the model. With this, we find the quantile value of $X_{99\%}$ on the empirical histogram curves for is very close to $T_{s2} = \mu_{geo}\sigma_{geo}^3$ of the fitted lognormal distribution. Similar results of other quantile values can be derived. It thus, can be used to test the fitness of the model.

Finally, use of the lognormal distribution fitting method provides us a way to indicate the levels of generations on the vessel map with succinct parameter representation. It can therefore be further used as a characteristic curve for each vessel map and in comparing the vessel generations on different retina images. Knowing that the essence of the skewed shape of lognormal curve is determined by the underlying physical property of ratios of vessel pixels among different generation levels, it can be used as a good indicator of vessel diseases as is with the case of neo-vascularizations. Such study will be conducted in our follow up research when more data are available.

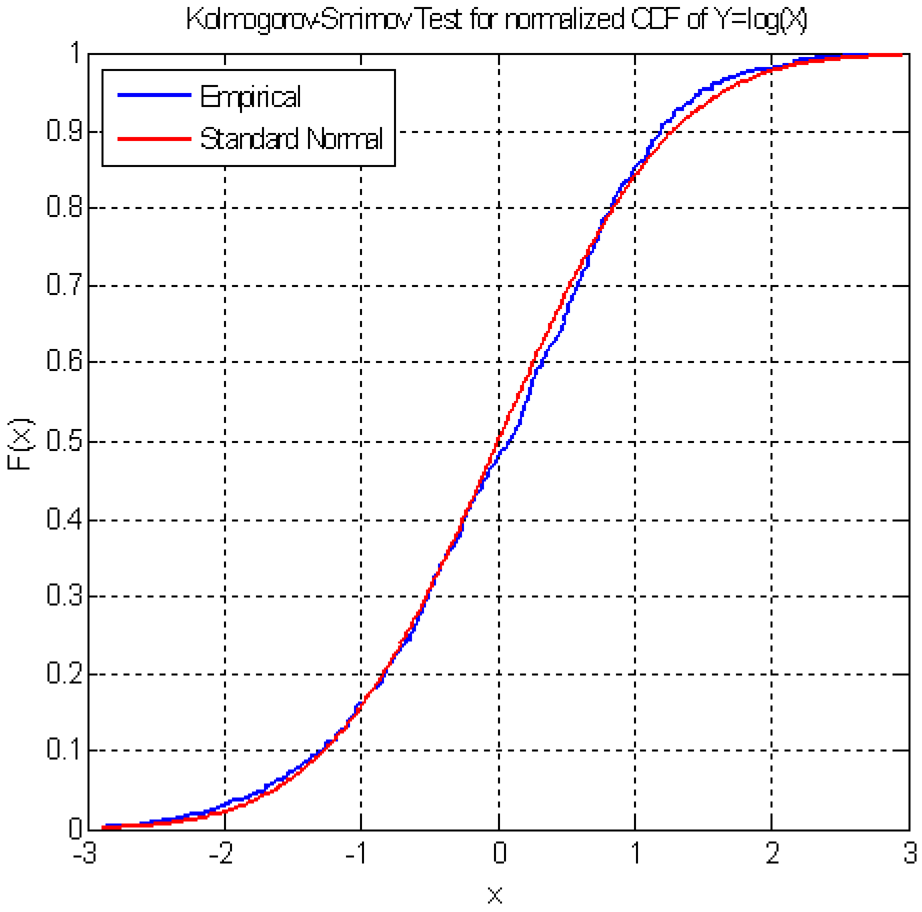

(a)

Figure 17: The CDF plots of ln(S_p) values of (a) BV and (b) BV boundary pixels v.s. their fitted normal distributions. Taking the logarithm of the original S_p value and normalized by estimated $\hat{\mu}$ and $\hat{\sigma}$, it can be seen that the converted data samples match the normal distribution.

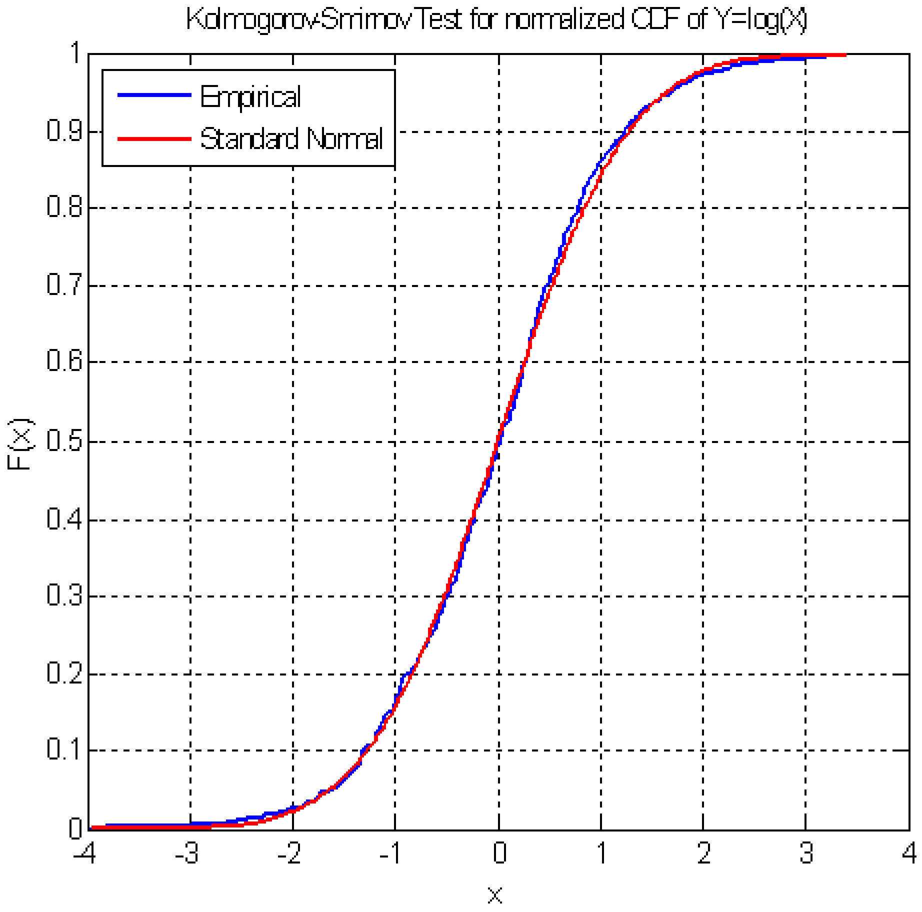

(b)

Figure 17 continued.

E. Summary of the Chapter

In summary, this chapter presents a novel technique to characterize the statistical distribution of BV and its boundary pixels in a feature space *F* of the daisy graph representation of the *RCT* outputs. The relationship between BV and its boundaries can be effectively represented by two fitted curve models along S_p descriptors. We can draw the following conclusions:

Regardless of the interpolated BV boundary pixels on hand-labeled results, negative E_p value is a statistically sound attribute to characterize the BV and the boundary pixels along E_p descriptor.

Histograms of both BV and BV boundary pixels along the S_p descriptor can be effectively fit to the lognormal distribution. The S_p value of the BV and BV boundary pixels is indicative of the generation levels of the vascular network. Their distributions are highly correlated against different images in DRIVE based on the comparison between paired measures from *{Ts_BV}* and *{Ts_Boundary}*. As a result, we are able to use *{Ts_Boundary}* to infer the BV pixel distribution on *F*.

The fitted curve model offers a simple yet efficient tool in tradeoff analysis between sensitivity and specificity for pixel classifications. Using the derived statistic measures, we are able to capture the dynamics between in-BV, the BV boundary and non-BV pixels.

The derived statistical results are important clues to pixel classifications for BV mapping operations. Using these results, we will further propose our BV mapping algorithm in the following chapter. Fitness of the model is substantiated by extensive tests on retina images in both DRIVE and STARE databases. That being said, a closer look into retina images on DRIVE and STARE shows that few of them have vascular diseases such as neovascularizations [81][82], for which the ratio of large to small BV pixel count may differ significantly. Our ongoing study will aim to capture the change in the distribution that may correlate to the vascular disease patterns. We also aim to use the fitness of the lognormal distribution model for BV segmentation map as the metric for automated retinal vascular disease analysis.

CHAPTER IV

RETINAL OBJECT DETECTION ALGORITHMS

A. Overview of the Chapter

In this chapter, we propose algorithms for automated segmentation of the three landmark retinal objects on retinal images. In practice, imaging conditions like illumination, field clarities as well as diseased objects make the reliable detection of these objects an even complicated process. The purpose of our study is to design accurate and reliable detection algorithms with adaptive parameter adjustment and less susceptible to field clarities and diseased objects.

Our BV detection algorithm derives from our statistical model of the BV statistics in our previous chapter. The lognormal distribution models of BV pixels for BV and BV boundary are critical for the design of a self-adaptive BV mapping algorithm against different image factors. In this technique, we use the Sobel edge detector [83] as an approximation of the BV boundary to derive a fitted lognormal distribution. Based on statistical measures of the fitted curve, one can reliably estimate the adaptive threshold for BV detection on different retinal images. We further develop the BV mapping operation into a few stages. Using increased threshold values in S_p derived from the fitted curve at each stage, we grow the vascular network by including candidate BV pixels followed by a continuity checking rule to suppress the noise artifacts. The resulting algorithm achieves high performance compared with the state-of-the-art algorithms and is much more computational efficient.

We also propose a simple yet robust unsupervised algorithm for automated localization of macula-fovea area on retinal images. The small sizes and weak contrast of the macula-fovea area on retinal images make it unreliable to detect it directly. As such, one can extract the retina blood vessel network topology based on local energy function of blood vessel widths and densities and use it as the main image cue to position the macula-fovea area. Regardless of the severity of most retinal diseases as well as variations in field clarity, the high level topology of the retina blood vessel flows remains fairly predictable. Compared with conventional algorithms, our method can effectively localize the macula-fovea area on retinal images with inadequate field clarity and diseased conditions.

We further propose novel algorithms to detect optic disc location on retinal images. Optic disc is a bright disc area and all major blood vessels and nerves originate from it. Due to the similar color tone in diseased objects like hard exudates and drusen, they will introduce false positives in reliable detection of OD area. We find optic disc can be more reliably differentiated from other bright regions with its high fractal dimension of vessels in its local area. As such, similar to the idea used in M-F location, we first use the topology of BV network to determine the search region of OD. Further, we combine the use of fractals dimension and bright spot detection to locate OD based on a divide-and-conquer strategy. Both our M-F and OD localization algorithms are tested on benchmark image databases STARE and DRIVE and gained satisfactory detection results.

B. Blood Vessel Mapping

1. Algorithm

Knowing that in the feature space *F* statistical behaviors of BV and BV boundaries and their relationships are highly stable against variations in different images, we are able to design a highly effective BV mapping algorithm based on its boundary statistics. We use a

Sobel edge detector to probe the boundary statistics. The detected edge pixels are highly correlated with the true BV boundary pixels on retinal image laden with vascular network, which have been studied in several BV mapping algorithms [11][84]. Among the detected edge pixels, we determine those with negative E_p values to be the BV boundary pixels. Despite of the chance of inclusion of few non-BV boundary pixels, their effects on the boundary statistics can be ignored due to the small number of artifacts in most cases. We fit the S_p values for the obtained boundary pixels to lognormal distribution and derived *{Ts_Boundary}* set values from the fitted distribution. When sliding the threshold values in S_p from T_{s1} to T_{s6}, we aim to detect the BV pixels by capturing the dynamics in BV generations, i.e., from "ridge to boundary, large to small BV branches", with minimal inclusion of non-BV pixels.

Based on the above discussion, we develop our BV detection algorithm into six stages. At each stage, we use one of the six threshold values from T_{s1} to T_{s6} in *{Ts_Boundary}* to generate a set of candidate BV pixels in $F_{neg\text{-}E}$. When $S_p = T_{s1}$, only BV ridge pixels would be included, and they are used as the seed ridge pixels for growing the vascular network. When S_p becomes larger, more BV boundary and small BV branches are included, but in the mean time some noise artifacts would also be added. As such, at each subsequent stage, we grow the vascular network by including only candidate BV pixels that are at close proximity of the vascular network obtained from the previous stages. Further, we suppress the artifacts by exploiting the continuity property of BV flows for each included candidate BV pixel. It is observed that when approaching the limit of the optical resolution, it is no longer reliable to take a per-pixel analysis technique for BV mapping. On the other hand, BV flows exhibit continuity even when they become very shallow and clouded while the included non-BV pixels are usually isolated from each other [25][26]. We explore the BV continuity property by similarity checking on the daisy graphs for neighboring candidate BV pixels along each probing BV direction. We observe that pixels along the BV flow would all have similarly negative sharper contrast perpendicular to the probing direction of the BV flow (illustrated in Figure 18). For smeared or fragmented BVs, usually only a small fraction of severely blocked BV pixels (so as non-BV pixels) do not conform to this property. Based on the above observation, we derive our probing rule as follows.

Let p be the candidate BV pixel included under the S_p threshold value from *{Ts_Boundary}* set for each stage. p would be labeled as a BV pixel if the following conditions are all met.

(1) For pixel p, test if there exists a flow direction θ , such that the two opposite *RCT* components perpendicular to the flow direction are negatively sharper than a threshold C_{min}, i.e., $C_p^{(\theta\pm\frac{\pi}{2})} \leq C_{min}$.

(2) If yes, test if $C_q^{(\theta\pm\frac{\pi}{2})} \leq C_{min}$, for γL pixels in the neighborhood of p along the probing direction θ, where γ is an error tolerance parameter for smeared or fragmented BVs.

(3) If among the γL pixels, there exists a pixel on the vascular tree developed from the previous stage.

Among the γL pixels, there exists a BV pixel on the vascular tree developed from the previous stage so that the determined BV pixel is close to the vascular network.

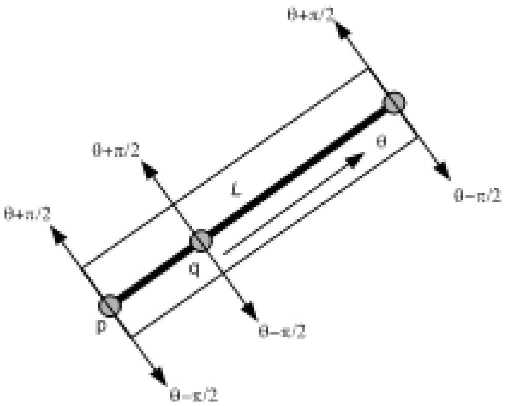

Figure 18: Illustration of the continuity probing of BV flow.

Selection of parameters in *γ, L* and the number of probing directions is mainly based on image resolution. Also, C_{min} is determined by the minimum contrast that is discernible by human eyes [73]. Settings of these parameters for image resolution of 584x565 or similar will be discussed in the following subsection.

Finally, we summarize our BV mapping algorithm in Table 1:

Table 1: BV mapping algorithm.

Objective

Map Retina Blood Vessels on Retina Image

Algorithm

Step I: Pixel Classification on *F*

(i) Edge detection using the Sobel operator to obtain the edge pixels.

(ii) Compute S_p values for the obtained edge pixels that have negative E_p values and fit their histogram plot to log-normal distribution curve.

(iii) Derive the *{Ts_Boundary}* set for the fitted lognormal distribution and use them as the threshold values on S_p descriptor.

Step II: Construct the vascular network by continuity checking on the original image for the candidate pixels included under different S_p threshold values.

(iv) Obtain the BV ridge seed pixels by setting $S_p = Ts1$ from *{Ts_Boundary}*.

(v) Use different S_p threshold values from T_{s2} to T_{s6} in *{Ts_Boundary}* to include candidate BV pixels with negative E_p values for each of the following stage. Grow the vascular network by flow continuity check. A new pixel p is added to the BV vascular network if the following conditions are all met.

- a) For pixel p, test if there exists a flow direction θ , such that the two opposite RCT components perpendicular to the flow direction are negatively sharper than a threshold C_{min}, *i.e.,* $C_p^{(\theta \pm \frac{\pi}{2})} \leq C_{min}$,
- b) If yes, test if $C_q^{(\theta \pm \frac{\pi}{2})} \leq C_{min}$, for γL pixels in the neighborhood of p along the probing direction θ, where γ is an error tolerance parameter for smeared or fragmented BVs.
- c) If among the γL pixels, there exists a pixel on the vascular tree developed from the previous stage.

2. Experimental Results and Discussions

Next, we test the performance of BV detection scheme based on the analytical model of pixel distribution on ***F***. The algorithm is implemented in C# and is tested on both DRIVE and STARE databases. For images in both databases, we use the same parameters for C_{min}= -0.02 , γ=0.8, L=10. C_{min} is based on the minimum contrast that is discernible by human eyes [73][85]. For image resolution of 705x600 or similar, L is determined by the shortest BV segments which are approximately 10 pixels in length and γ is the error tolerance for BV continuity. Besides, in using the Sobel edge detector for probing the boundary statistics, we choose a quantile threshold Q_T on the resulted edge map to label the corresponding edge pixels on each image. Q_T is set to be 0.92 in the following discussions. Effects of edge detector on the detection results would be discussed later.

We note that the evaluation of the BV segmentation is more difficult, because of lack of a reliable ground truth set. Besides, different evaluation metrics [19] [24] [86] may be needed for different applications. Performance of the algorithm may vary significantly under different evaluation metrics. The most common conventional method is to select one human segmented result as the ground truth set and measure the algorithm performance using the receiver operating characteristic (ROC) curves. ROC curve is a graphical plot of the true positive rate (TPR) vs. false positive rate (FPR). By true positive, we mean the image pixel which is identified as the vessel pixel by both the detection result and the ground truth set. While false positive is the pixel which is determined to be the vessel pixel by the detection result but not by the ground truth set. The TPR is calculated by dividing the total number of true positives by the total number of vessel pixels in the ground truth set. The FPR is calculated by dividing the total number of false positives by the total number of non-BV pixels in the ground truth set. For conventional binary classification problems, the closer a ROC curve approaches the top left corner, the better the performance of the method is and the area under the ROC curve is to be the largest equal to 1.

To compare with several of the state-of-the art algorithms, we show the performance of our BV detection algorithms under the ROC measure. The calculated TPR and FPR were obtained over all the images in DRIVE and STARE. Paired values of the TPR vs. FPR for our detection algorithm are obtained under different threshold values (from T_{s1} to T_{s6}) on F for each stage. Paired measures for other detection algorithms were obtained based on different parameter settings reported. Results for the ROC curves for different methods on DRIVE and STARE databases are plotted in Figure 19(a) and (b) respectively. Like many others, we also include the hand-labeled results from another observer into our discussion and use it as the human observer performance. It is observed that, due to the disagreement in human judgments on “single-marked” BV pixels, the human observer performance is not located at the top-left corner on the plot. Human observer performance is important in setting up the criterion for evaluating the BV detection performance. It can thus be inferred that the algorithm performance that produces the largest area under the ROC curve may not necessarily be the optimum. Instead, we may estimate the statistically optimal region on the ROC plots referring to both the human observer performance and the ground truth set.

In terms of the ROC measure using the ground truth set from the first human expert in both DRIVE and STARE databases, our algorithm achieves similar performance with the Staal’s methods[87] and outperforms Chauduri et al.’s[11] and Jiang’s algorithms[26]. Staal’s methods is among the state-of-the-art algorithms that produce high area under the ROC curves. However, our detection scheme has much less computational cost as compared with Staal’s method (25~30 seconds on a 1GHz CPU for our algorithm compared with 15min on a 1GHz CPU for Staal’s method).

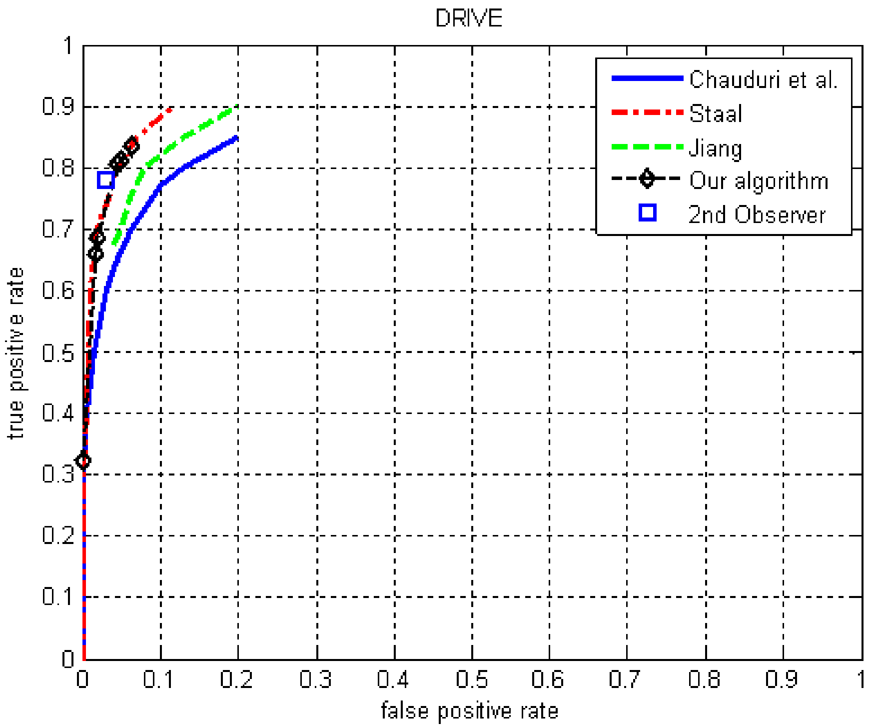

(a)

Figure 19: ROC curves for comparing the detection results in both DRIVE and STARE databases between our algorithm and some state-of-the art algorithms. (a) DRIVE databases. (b) STARE databases.

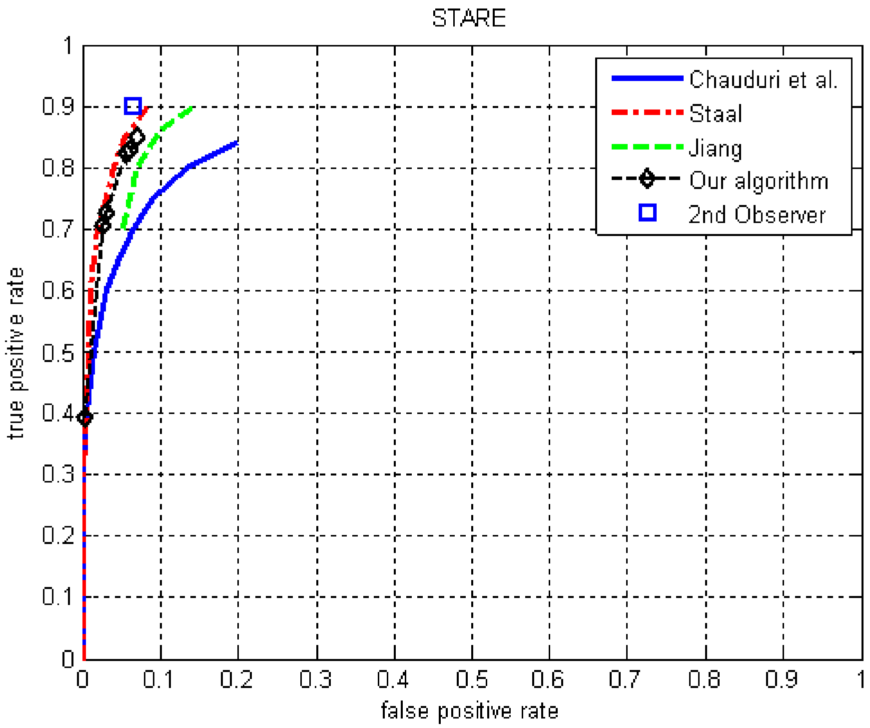

(b)

Figure 19 continued.

Illustrative detection results for images from each database under different iterations along with the hand-labeled results are shown in Figure 20. Different from other detection outcomes, sliding the S_p values from small to large values, the detected BV pixel map mimics the dynamics in BV generations (from ridge to boundary and from large to small branches).

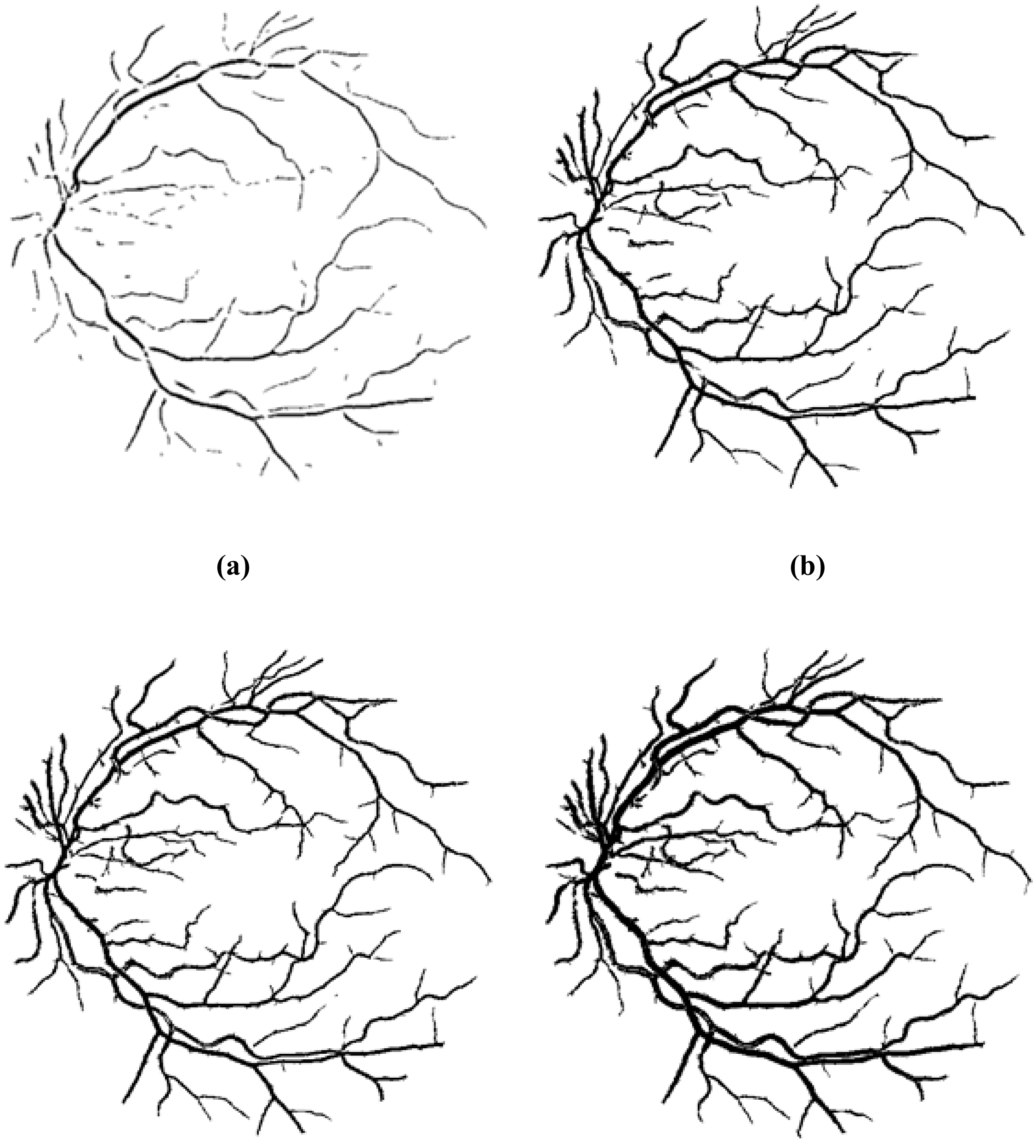

(a) **(b)**

(c) **(d)**

Figure 20: BV mapping results for a retina image in DRIVE. (a) to (f) show detected BV pixels at each stage by including candidate pixels on F using the six threshold values for *{Ts_Boundary}*. (g) and (h) are the hand-labeled reference BV maps.

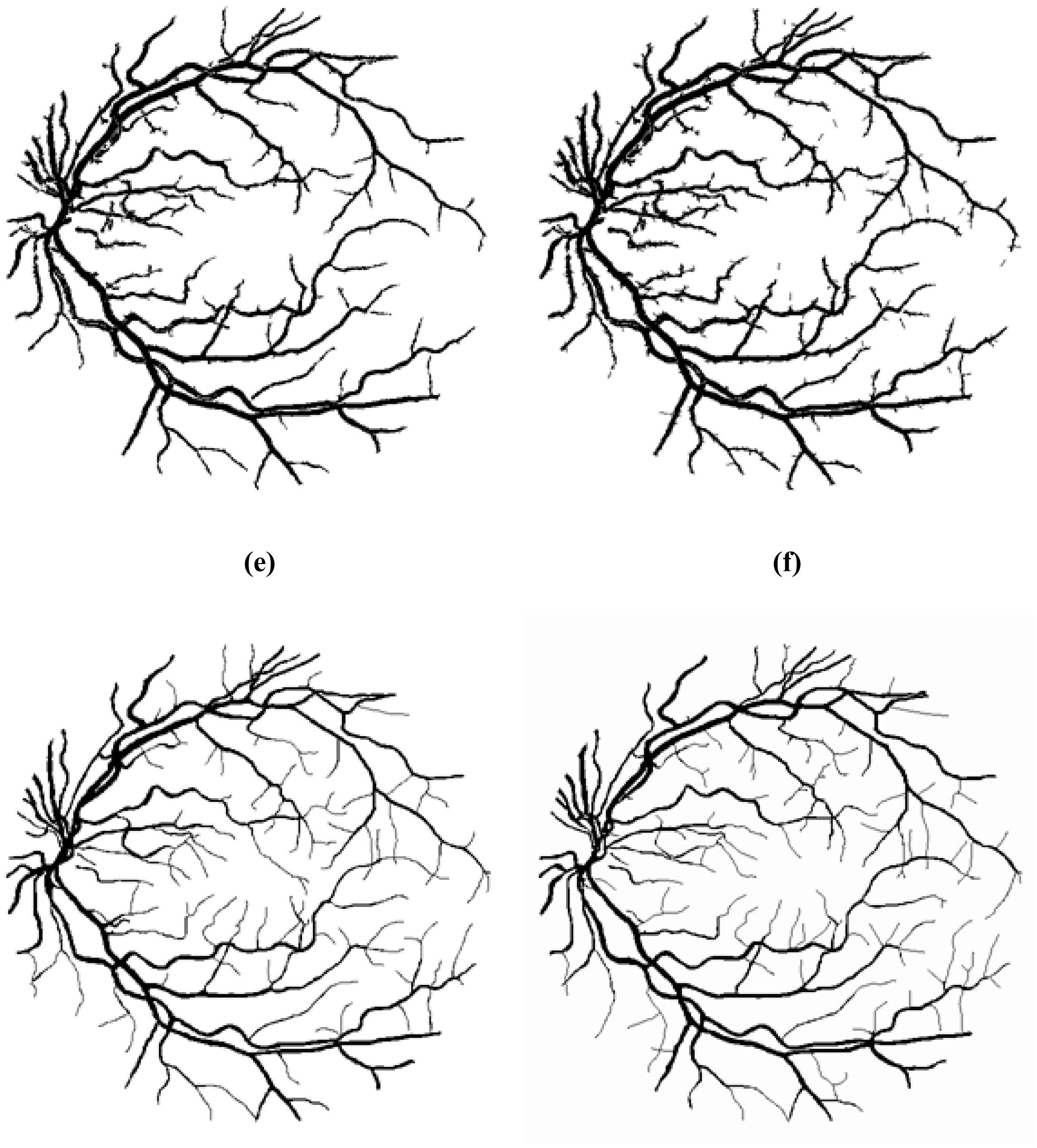

(e) **(f)**

(g) **(h)**

Figure 20 continued.

The main contribution of this algorithm is a novel analytical model to characterize the distribution of BV and BV boundary pixels in the feature space *F*. The universality of the pixel distribution for BV and BV boundary pixels on *F* and their relationships was tested using retina images for both DRIVE and STARE databases. Some informal observations show that the S_p descriptor is quite consistent with the BV generation order of BV pixels. This may suggest that why the S_p histograms for BV and BV boundary pixels can be fit to the lognormal distribution effectively. The highly consistent relationship between the two curves is validated using images in both databases.

The proposed analytical model on the feature space F is highly effective for design of a BV detection algorithm by probing of the boundary statistics. BV pixels at different generation levels can be differentiated stage by stage using different statistic measures derived from the fitted curve model. We use the Sobel edge detector on the original retina image to probe the boundary statistics, and then use the results to predict the BV pixel behavior on F. The quantile threshold Q_T on the resulted Sobel edge map is set to be 0.92 to obtain the edge map. Empirical results show that it serves well for extracting the BV edges with minimal side effects caused by severe noise or artifacts in highly diseased retinas (shown in Figure 21(a) and (b)). The choice of the Q_T also implies the detection sensitivity in probing the most small and shallow BV boundaries. We test the effects of Q_T of different values within range of 0.9~0.95 on the curve fitting results. The results shown in Figure 21(c) suggest that the S_p descriptors for edge pixels captured using different Q_T values can all be fit to lognormal distribution with small errors. The resulted *{Ts_Boundary}* sets under different Q_T's do not change much in small S_p values (less than T_{s5}) (see in Table 2). Therefore, it has negligible effects on detection of the BV "ridge pixels", nor on the growth of vascular tree for the first four to five iterations in BV detection algorithm. On the other hand, their T_{s6} values would be different due to the differences in their tail extensions on different fitted curves due to the different detection sensitivity by using different Q_T's.

Therefore, it would include different amount of candidate BV pixels for the last one or two iterations, and may serve different purposes for small and shallow BV detection.

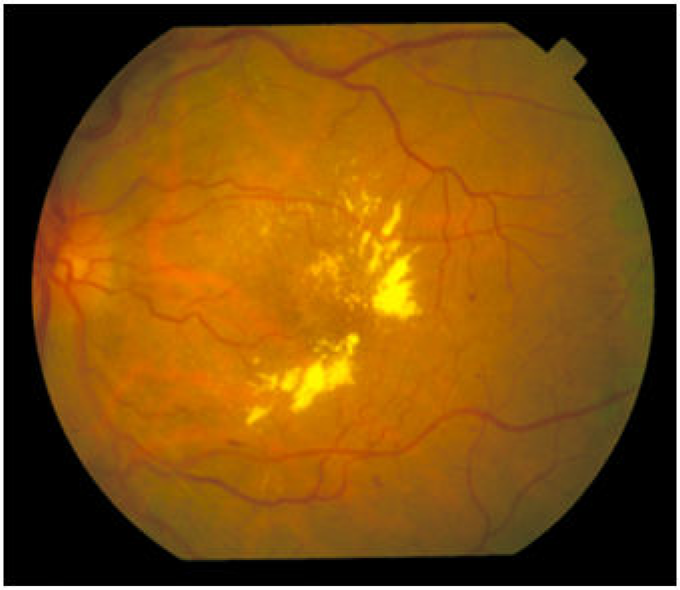

(a)

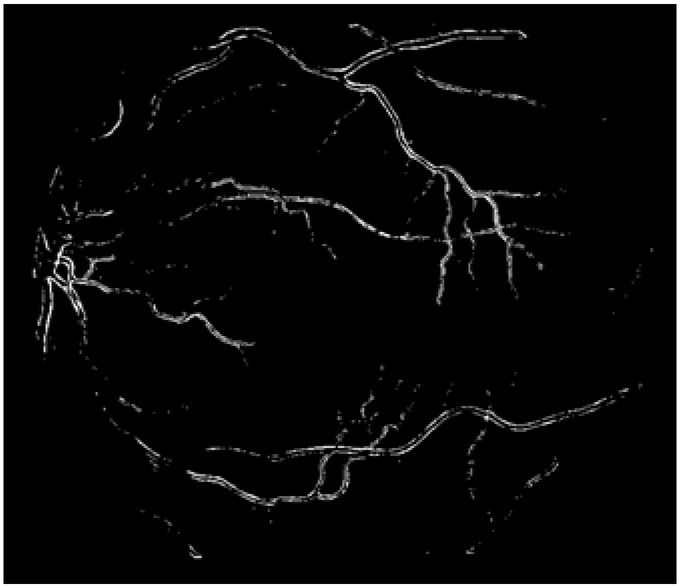

(b)

Figure 21: Effects of different Q_T thresholds on fitted curves for detected edge pixels. (a) Original image. (b) Edge pixel map by choosing Q_T=0.92. (c) Fitted lognormal distribution curves for Q_T values ranging from 0.9 to 0.95.

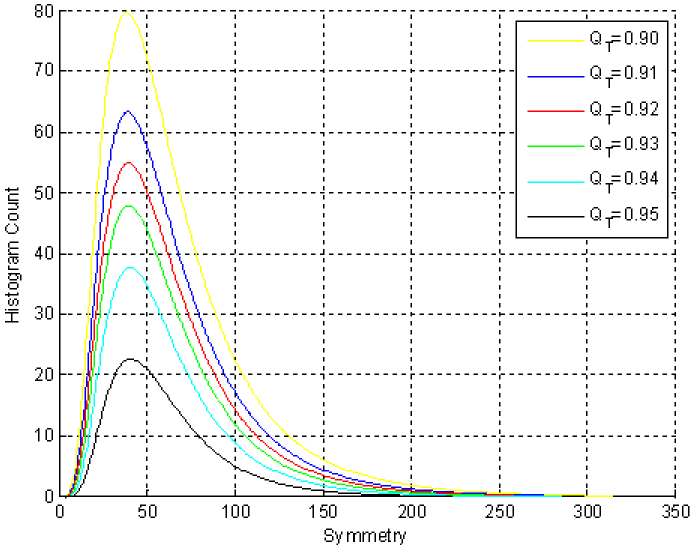

(c)

Figure 21 continued.

Table 2:*{Ts_Boundary}* set values under different Q_T thresholds.

	Q_T=0.90	Q_T=0.91	Q_T=0.92	Q_T=0.93	Q_T=0.94	Q_T=0.95
T_s1	38.544	38.9791	39.4013	39.6726	40.3312	41.0913
T_s2	55.2319	54.7907	54.4769	53.9265	53.5402	53.4585
T_s3	66.116	64.9598	64.0565	62.8721	61.6878	60.9748
T_s4	100.6172	98.2033	96.2518	93.8467	91.1675	89.2863
T_s5	183.2968	176.0133	170.0612	163.3187	155.2388	149.1259
T_s6	333.9159	315.4749	300.4704	284.2188	264.3386	249.0699

In general, the algorithm is fast, self-calibrated to the optimal detection parameters of each image itself, sensitive, robust and with strong ROC results. It can suppress some artifact by picking linear segments near the BV ridge pixels, some objects that strongly resemble BV segments may still be mistaken for BV pixels, e.g., the outer ring of the optic disc, cracks between the hard exudates, hemorrhages, etc. These issues are most common for images laden with severe diseases and artifact (see example in Figure 22). These types of issues can be improved by techniques like the one proposed in [88].

Figure 22: Detection result for the diseased images in Figure 18. Cracks between the hard exudates patches are mislabelled as BV segments due to their nearly identical linear shape and negative contrast against the neighboring areas.

In summary, the analytical model for the BV pixel distribution on *F* provides the basis in characterizing the statistical attributes for BV pixels at different generation levels. It is well incorporated into our design of BV detection algorithms. The algorithm is simple, fast, self-calibrated, and its ROC performance results are highly competitive against existing algorithms.

C. Macula-fovea Area Localization

1. Introduction

Existing methods mainly defined or trained their BV trajectory models using the images which have adequate field clarity [41], i.e., the optic disc (OD), M-F area and vessel arcades on both superior and inferior sides are all within the field of view. They first detect the OD, and then use it to position the M-F area, but this approach is subject to interference of diseased objects like hard exudates, drusen, etc, which may have brighter intensity than the OD. It is also very common that retinal images acquired from the field may not have adequate field clarity, e.g. only partial optic disk is included in the image or superior/inferior side BV arcade is not photographed. The general detection performance for those images is not well known, except that [89] illustrated some false detection outcomes due to parameter selection problems.

Our M-F area localization algorithm is aimed at attacking aforementioned problems. We propose a simple yet robust unsupervised algorithm for M-F area localization by extracting the vascular network topology. The proposed algorithm consists of three major steps. In step 1, we map the blood vessels and form a vascular topology map (*VTM*) based on vessel width and density. We adjust the detection sensitivity at the vessel mapping step to suppress the potential interference of small and anomalous vessels (neovascularization and large hemorrhages). In step 2, we fit the main vessel arcade pixels on the high energy band on *VTM* to a circle model so as to determine the search region for the M-F area. We also use the fitting error as an inference of the field of clarity of the original image, and use it to label the image as either field-1 or field-2 type. In step 3, for each pixel *X* within the circle, we design three features to reflect the presence of blood vessels around *X*, its spatial relation to the extracted arcade pixels and its intensity respectively. We use the former two features to position a candidate M-F area and propose a weight assignment rule among the first two features based on a logistic function of the fitting errors, in order to offset the effects of field clarity. Finally, we use the intensity feature as a complement to refine the detection results. This way, one can reliably locate the M-F area.

2. Algorithm

As introduced in chapter one, field-1 and field-2 (see Figure 23) are the two common types of retinal images acquired in clinic settings. The former centers the optic disc area and the latter centers the macula area [4]. Field-1 images may either not contain the macula or have it at the very left or right side in the field of view (FOV). On the basis of a conservative design principle, field-1 images are excluded from the step of automated localization of the M-F area due to the poor illumination at the side area around the FOV on most field-1 images, which would lead to inconclusive localization results even for human judgment. Accordingly, we design a detection rule that automatically separate field-1 images from the field-2 types and locate M-F area on the separated field-2 images.

(a) (b)

Figure 23: Illustration of M-F area on field-1 and field-2 images. (a) Field-1 image. (b) Field-2 image (Fovea and macula are circled).

2.1. Vascular Topology Map (VTM)

The vessel arcade in the retina represents the collection of thickest blood vessels flowing from the optic disc to the whole retina area. On the other hand, the macula area has the least amount of large blood vessels. In this section, we separate the (large) blood vessel rich areas from the rest of the retina by a pixel level energy function map using local vessel widths and densities. We map the blood vessels using the algorithm proposed in previous subsection and adjust the detection sensitivity at the vessel mapping step to suppress the potential interference of small and anomalous vessels (neovascularization and large hemorrhages). By taking moving average of the energy function map with an $(N_w+1)x(N_w + 1)$ kernel ω, we generate the *VTM* to quantify and visualize the vascular network topology . For images of size 700x605 or 565x584, we set N_w to be 64, based on a rough estimation on the sizes of the whole macular area.

The energy function $WDD(x,y)$ for each pixel is the normalized product of the local BV width $W(x,y)$ and density $D(x,y)$ in ω.

$$\mathrm{WDD(x,y)} = \frac{\mathrm{W(x,y)\ x\ D(x,y)}}{\mathrm{Wmax\ x\ Dmax}}$$

where $Wmax$ and $Dmax$ are respectively the largest *W(.)* and *D(.)* values in the whole image. Let I_B denote the binary BV map of a retinal image, the *D(.)* value for each pixel p is calculated by simple counting of BV pixels in ω. The *W(.)* value of p is the average of the width measurements $C_T(x,y)$ for pixels in ω on I_T (the binary thinning on I_B) based on a rotational search routine on the I_B by counting the number of consecutive BV pixels along the lines of 16 different directions from 0° to 180° going through (x,y). The smallest value of the sixteen different observations is used for $C_T(x,y)$. In summary, the *W(.)* and *D(.)* values for a BV pixel located at (x,y) can be respectively expressed as:

$$W(x,y) \quad = \frac{\sum_{\mathrm{i}=-\mathrm{N_w}/2}^{\mathrm{N_w}/2}\sum_{\mathrm{j}=-\mathrm{N_w}/2}^{\mathrm{N_w}/2} I_T(x+i,y+j)*CT(x,y)}{\sum_{\mathrm{i}=-\mathrm{N}/2}^{\mathrm{N}/2}\sum_{\mathrm{j}=-\mathrm{N}/2}^{\mathrm{N}/2} I_T(x+i,y+j)},$$

$$\mathrm{D(x,y)} = \frac{\sum_{\mathrm{i}=-\mathrm{N_w}/2}^{\mathrm{N_w}/2}\sum_{\mathrm{j}=-\mathrm{N_w}/2}^{\mathrm{N_w}/2} I_B(x+i,y+j)}{(\mathrm{N_w}+1)*(\mathrm{N_w}+1)}\,.$$

Figure 24 shows two examples of the calculated VTM maps (b) and (e) on field-1 and field-2 images respectively resulted from the BV mapping results (a) and (d).

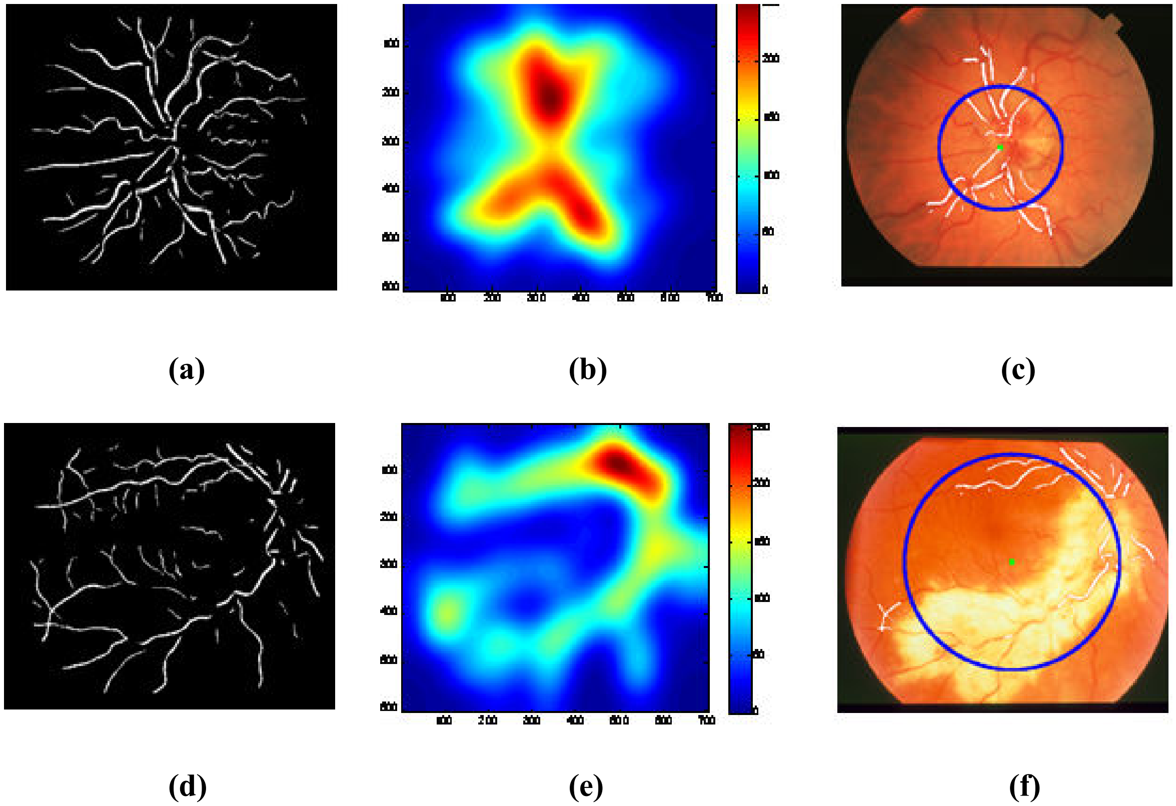

Figure 24: (a),(d) are the segmented BV maps. (b),(e) are the VTM maps resulted from (a) and (d) respectively. (c),(f) are the circle fitting results, on which, the white color denote the vessel pixels extracted on the high energy band in (b) and (e), the green dot denotes the fitted circle center and the blue the fitted circle.

2.2 Circle Fitting of the Main Vascular Arcades

Field-1 images usually have an *X-shaped* high energy band pattern on the *VTM* whereas the band is horseshoe-shaped enclosing the M-F area on field-2 images. We are to model vessel arcades on field-2 images by extracting the vessel pixels in the high energy band area on *VTM* and using a circle model to fit the extracted pixels. On the other hand, the same circle fitting method would result in comparatively large fitting errors for field-1 images. We could therefore use the fitting error as an identifier for the field types of the retina image.

We choose a quantile threshold Q_T on *VTM* to label a corresponding high energy band area and use Kasa's method [90] to do the circle fitting. Let *Arcade_Circle* denote the fitted circle, whose center and radius are respectively denoted as *CtSrh(Xc,Yc)* and *RadSrh*. Fitting error is represented as the mean squared error *(MSE)* of the differences between the fitted circle radius and the Euclidean distances from the circle center to the extracted BV pixels. In comparing the fitting error among different images, we normalize the *MSE* by their fitted radius *RadSrh* and denote it as *fit_Err*. We also use a simple enumerative comparison of fitting errors for a range of Q_T values, and pick the one with the smallest *fit_Err* as the best fitted circle model for the image. In our experiments, the Q_T value set in the range of 0.9 to 0.7, at 0.05 increments gave satisfactory results to cover the possible circle models.

Fitted circles as well as the extracted BV pixels are shown in Figure 24 (c) and (f). Comprehensive statistics on the fitting errors demonstrates that most small *fit_Err* results from field-2 images with adequate field clarity (less than 0.1), where the fitted circle center is very close to the fovea. *fit_Err* increases (within the range 0.1~0.2) when the image does not have good field clarity. Circle center on these images would deviate from the fovea. Empirically, we find that *fit_Err* = 0.25 is a reliable threshold value to separate field-1 from field-2 images.

An alternative method for the extraction of vessel arcade pixels can be derived from our log-normal curve model of detected vessel map presented in previous chapter. By setting the threshold on S_p equal to *Ts1* from *{Ts_Boundary}*, it is more computational efficient. Using the same *fit_Err* to indicate field-1 and field-2 image, the results are almost the same. This further substantiates the practical use of our model of vessel generations.

2.3 Macula-Fovea Localization

We are then to locate M-F in *Arcade_Circle* on field-2 images. On normal retina, fovea is a dark circular shape. However, intensities within the M-F area would become high when there exist retinal diseases such like age-related macular degeneration, hard exudates, etc. On the other hand, the blood vessel network topology is more resilient to diseased conditions. Regardless of the severity of most retinal diseases, the high level topology of the retinal blood vessel flows remains fairly predictable. Therefore, we use the vessel topology as the primary image cues and use the intensity as a complement for M-F localization.

Accordingly, we use two features $F_{std}(.)$, $F_{avas}(.)$ to quantify the BV topology for each pixel (x, y) within *Arcade_Circle* with respect to its spatial relation to BV arcades pixels and the amount of vessels around it respectively. Its intensity feature is denoted as $F_{int}(.)$ In details,

$$F_{std}(x, y) = 1 - \frac{\sigma(x,y) - Min\{\sigma\}}{Max\{\sigma\} - Min\{\sigma\}},$$

$$F_{avas}(x, y) = 1 - \frac{WDD(x,y) - Min\{WDD\}}{Max\{WDD\} - Min\{WDD\}},$$

$$F_{int}(x, y) = 1 - \frac{I_G(x,y) - Min\{I_G\}}{Max\{I_G\} - Min\{I_G\}},$$

where, $Max\{.\}$ and $Min\{.\}$ denotes the maximum and minimum operators for the corresponding features within *Arcade_Circle*. $\sigma(x, y)$ is the standard deviation of distances between (x, y) and BV pixels in the segmented arcade area. Pixels near the center of the fitted circle would have small values on $\sigma(x, y)$ and thus large $F_{std}(x, y)$. $I_G(x, y)$ denotes the green channel intensity value. All the $F_{avas}(.)$, $F_{std}(.)$ and $F_{int}(.)$ are normalized to be within range [0,1]. Normal retina with adequate field clarity would have large values for all the three features. Feature maps are shown by example in Figure 25 (a),(b),(c).

We first use $F_{avas}(.)$ and $F_{std}(.)$ to predict a candidate M-F area. We propose a weight adjustment rule between the two using a logistic function of *fit_Err* to offset the field clarity as was illustrated in our previous discussion, so that $F_{std}(.)$ is assigned more weights when *fit_Err* is small and is suppressed when *fit_Err* is large. Weights on F_{avas} and F_{std} are denoted as w_{avas} and w_{std} respectively. The logistic function is formulated as follows:

$$\mathrm{w_{std}} = \mathrm{A} - \frac{\mathrm{A}}{1+\mathrm{e}^{-(fit\_Err\,*\mathrm{B}-\mathrm{C})}}$$

$$\mathrm{w_{avas}} = 1 - \mathrm{w_{std}},$$

where A sets the range for the maxima function response, B and C are parameters that determines the slope and cut off point of the logistic model respectively. Empirically, we set A=1, B=40, C=4. The resulted logistic function is depicted in Figure 24(d), on which $\mathrm{w_{std}}$ is suppressed when *fit_Err* is larger than 0.1. Our candidate M-F area is on the pixel with the largest $F_{Combined}(x, y)$ within the search region where

$$F_{Combined}(x, y) = w_{avas} * F_{avas}(x, y) + w_{std} * F_{std}(x, y).$$

Finally, we use $\mathrm{F_{int}}(.)$ to search for the dark pixels around the candidate with a search radius to be *RadSrh*/3, determined by the fixed distance between OD and M-F, which is of three disc sizes. Dark fovea pixels are those with both their $\mathrm{F_{int}}(.)$ and $\mathrm{F_{avas}}(.)$ greater than 0.95 in order to exclude the BV pixels. The average location of the found dark pixels is the final localized M-F area. If no dark pixel is found, we use the original candidate to be the final result. (See Figure 24 (f)). Algorithm for M-F localization is summarized in Table 3.

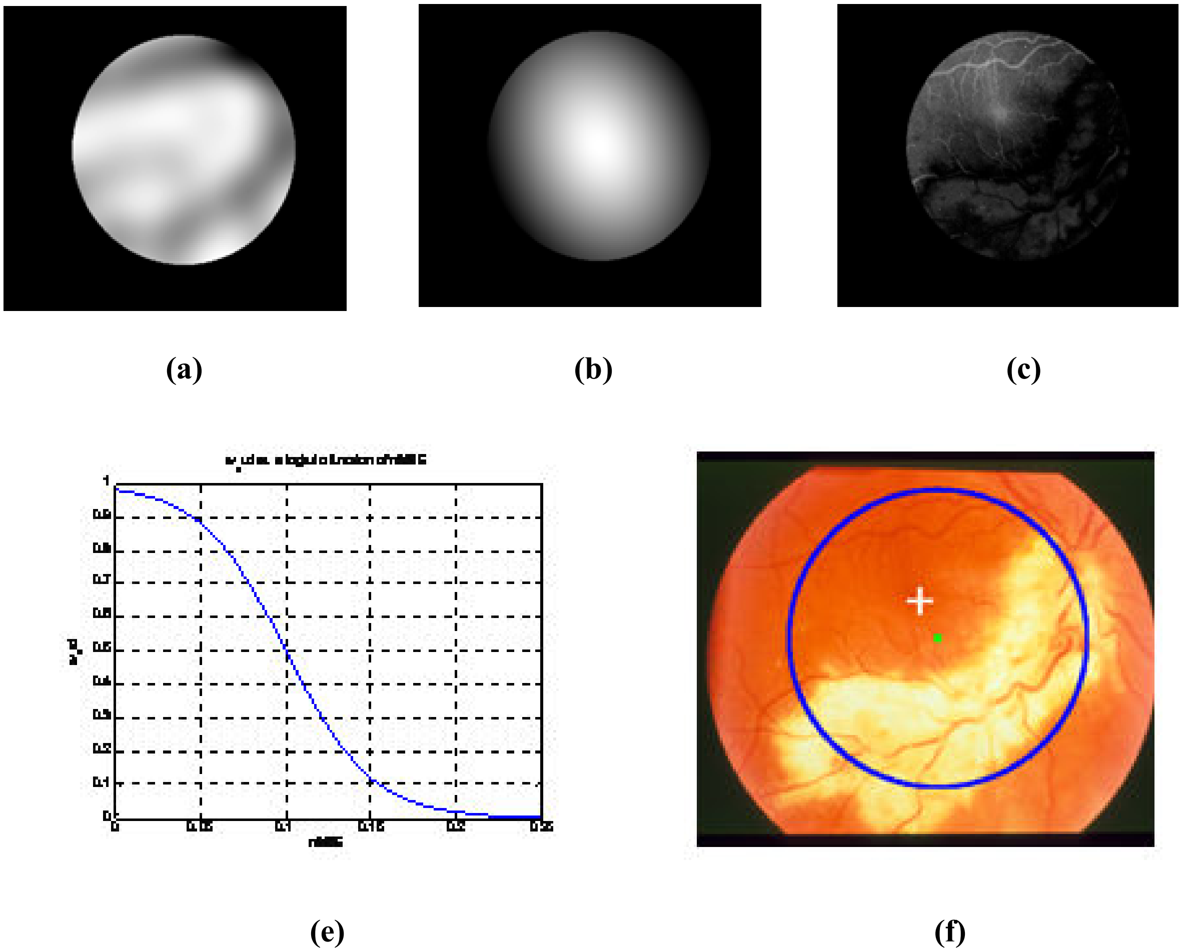

(a) (b) (c)

(e) (f)

Figure 25: (a), (b), (c) are the generated feature maps in C corresponding to $F_{avas}(.)$, $F_{std}(.)$ and $F_{int}(.)$ respectively where bright pixels correspond to large values. (d) is the logistic function of nMSE (e) is the final located M-F denoted as "+".

Table 3: M-F localization algorithm.

Objective

Locate Macula-Fovea(M-F) Area on Retinal Image

Algorithm

➢ Determine the search region of M-F on retinal image

1. Map blood vessels on retinal image.
2. Form a *vascular topology map (VTM)* based on vessel width and density.
3. Fit the main vessel arcade pixels on the high energy band on VTM to a circle model to determine the search region for M-F area. Use the fitting error *fit_Err* to label images as field-1 or field-2 images.

➢ Locate M-F within the search region

4. For each pixel X within the fitted circle, design three features to reflect the presence of blood vessels around X, its spatial relation to extract arcade pixels and its intensity.
5. Use adaptive weighting scheme among the features to locate M-F.

3. Experimental Results and Discussions

We evaluate our detection accuracy using the following criteria: (1) Separate the field-1 images from field-2 types. (2) For normal M-F area, the located M-F area should be within the contour of the fovea. (3) For diseased M-F area, the located M-F area should be within the vessel-free macula area. For situation (3), fovea area is usually hard to be recognized even for trained human eyes due to the deteriorated macula area.

We tested our algorithms on two public retina databases, DRIVE [2] and STARE [3] as well as our collected retina images from clinics. Their detection outcomes are shown in the Table 4. DRIVE images mostly have healthy conditions and adequate field clarity. However, STARE has more than half diseased images and many are poorly illuminated and have inadequate field clarities. DRIVE contains 40 retina images with 3 field-1 and the rest field-2 images. Our scheme correctly differentiates the 3 field-1 images and has a detection rate of 100% for the rest 37 field-2 images. STARE contains altogether 81 retinal images.

22 are field-1 and 59 are field-2 images. Using our scheme, 20 among the 22 field-1 images are correctly separated. For the rest 61 decided field-2 images, we have a detection rate of 93.4% (57 out of 61). Performance of our algorithm on the retinal images collected from on-site clinics shows a detection rate of 95.75% (857 out of 895).

Table 4: Performance evaluation of M-F detection algorithm.

DATABASE	Detection Rate on Field-2 Type Retinal Images
DRIVE	100% (37 out of 37)
STARE	93.4% (57 out of 67)
Our Database (from clinics)	95.75% (857 out of 895)

Several examples of the detection results for images of different field clarities and disease conditions are illustrated in Figure 26. In Figure 26, (a) is a typical normal retinal image with adequate field clarity. Fitted circle center is close to the fovea. (b) is a special case where field-1 image is not excluded from our detection system. However, M-F is correctly located. Different from other field-1 images, M-F area on this image can be clearly recognized and is located toward the image center so that the vessel arcade can be also well fitted to a curve. (c) has inadequate field clarity where the superior vessel arcade to the temporal side is not included. In (d), blood vessels in the inferior side are not detected due to the poor illuminations. Both M-F on (c) and (d) can be correctly localized where the circle is fitted to the half arcade. (e), (f) have severe macula diseases within the macula area and fovea can be barely recognized. However, their locations can still be predicted using BV topology.

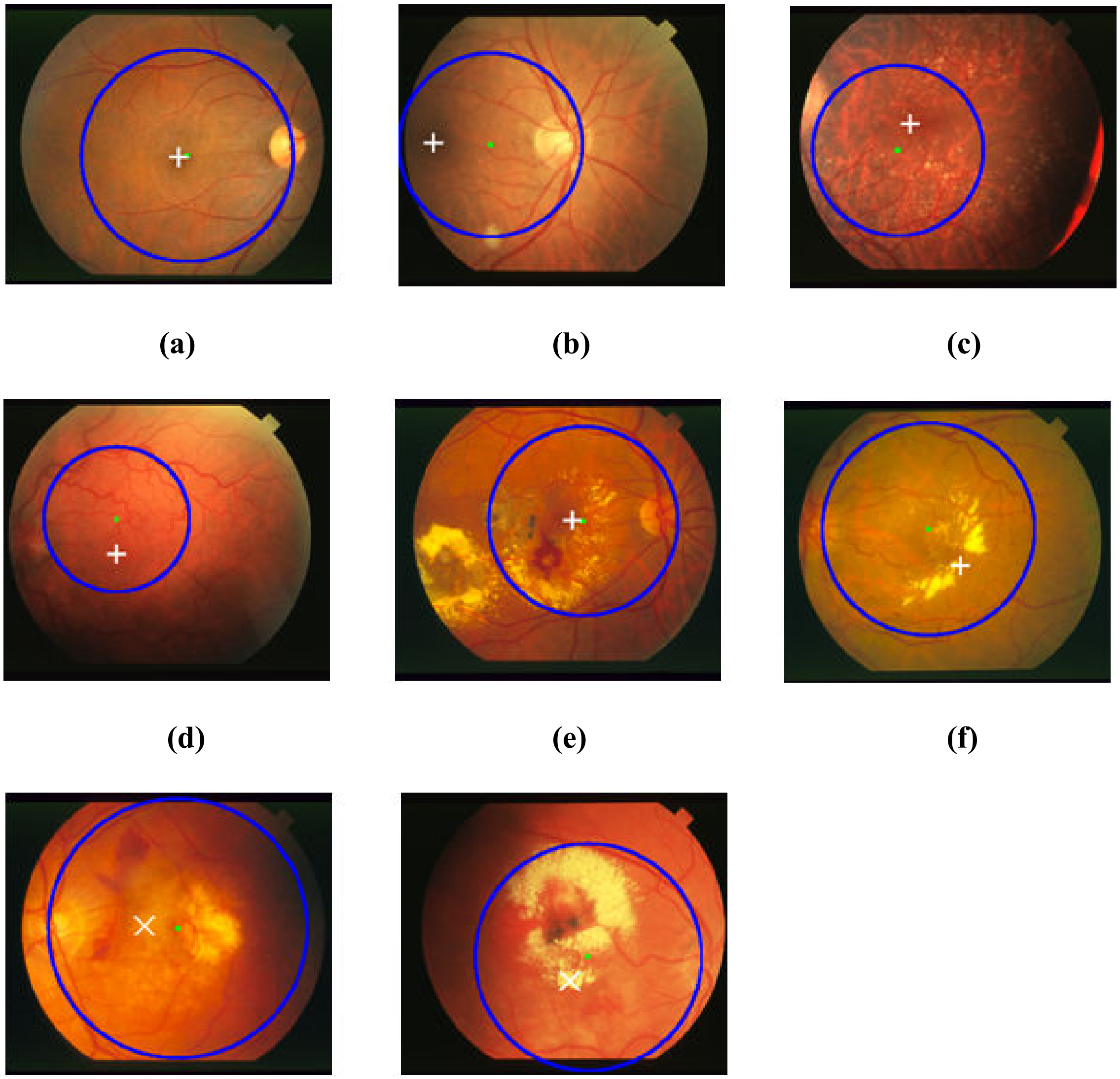

(a) (b) (c)

(d) (e) (f)

(g) (h)

Figure 26: M-F localization results. The green dot is the fitted circle center and the blue the fitted circle. White "+" and "x" signs denote the correct and false detection results respectively.

Two falsely detected cases are illustrated in Figure 26 (g),(h). Our results deviate from the true M-F area (within the bright patches). Both images are complicated with retina diseases of choroidal neovascularization and age related macular degeneration. In such cases, blood vessels grow into the macula. This is contrary to our basic assumptions on the vessel-free M-F area and thus results in false detection. However, we find these the extreme diseased cases in the late stage of retinopathy that would have already caused blindness and therefore, could be set apart from the early computer-aided retinopathy screening purposes.

In summary, we propose an unsupervised algorithm for the localization of M-F area by extracting the vessel network topology. Compared with conventional methods, our method can reliably separate field-1 images from the field-2 type and overcome the difficulties in M-F localization on images with inadequate field clarity and diseased conditions. Our scheme can be expanded for other retina objects segmentation such like the optic disc area, which will be discussed in the next session.

D. Optic Disc Localization

1. Introduction

Existing methods for OD localization mainly used its color tone or its relation to the global vessel directions as the main image cues. In practical clinic images, however, some optic discs are found not to be of bright colors. Also, in images with incomplete field clarity, partial vessel arcades are not captured. These, together with the diseased objects like hard exudates, drusen and artifacts, make reliable detection of OD even more difficult. As such, in this work, we propose a divide-and-conquer strategy for accurate and reliable localization of optic disc on retina images, which is resistant to incomplete field clarity, shallow appearances of OD and interferences of diseased objects.

Similar to our technique used in M-F localization, we first determine the field type and search region of OD area based on the circle fitting of vessel topology. Next, we narrow down the candidate OD areas based on feature detections of bright spot areas as well as fircation points of vessel segments. Within each candidate area, we apply local fractal analysis to characterize the concentration of blood vessels. Finally, our divide-and-conquer strategy is adopted to locate OD area considering all factors of local intensities, fractal dimensions and vessel topology.

2. Algorithm

2.1 Determine the Search Region for OD Area

Similar to our method used in M-F localization, we first determine the search region of OD area based on its relation to vascular topology. The vessel arcades are first extracted from *VTM* or derived log-normal curve model of detected vessel pixels using circle fitting method. The fitted circle is denoted as *Arcade_Circle*. Likewise, we used the fitted error *fit_Err* = 0.25 as a reliable threshold value f_T to separate field-1 from field-2 images. If the calculated *fit_Err* is smaller than f_T, it is determined as field-2 images. Otherwise, field-1 type. Then we determine the search center and search radius for OD denoted as *CtSrh* and *RadSrh* respectively. For field-1 image, *CtSrh* is determined to be the center of *Arcade_Circle*. For field-2 image, the optic disc is either on the left or on the right side of the fitted circle. Side location of OD can be further estimated from the comparison of number of detected BV pixels on each side, inferred from the fact that optic disc area is where the major retina blood vessels emerge. As such, if left side of the *Arcade_Circle* has more detected BV pixels, the search center is at leftmost side of *Arcade_Circle*. Otherwise, it is at the rightmost side of *Arcade_Circle*. We further determine the search radius *RadSrh* to be 1/3 of *Arcade_Circle*, in that optic disc is usually 2~3 disc sizes away from the M-F area.

2.2 Select Candidate OD Area

Two types of candidate areas are included for discussion for OD localization. One is the bright spot area. The other is the area where the blood vessel branches fircate.

Bright spot are detected using the daisy graph representation introduced in Chapter III. Pixel within bright spot area has positive contrasts against background areas along all probed directions. Figure 27 shows 25 pixels running across a bright spot area and their corresponding daisy graph representation. Brightness of the spot can be represented by the sharpness of its contrast against the background areas. Consequently, for a give pixel, let $Count(\theta|C_p^{(\theta)} \geq C_{pmin})$ denote the number of directions having positively contrasts sharper than C_{pmin}. $C_p^{(\theta)}$ is the calculated directional contrast along θ and C_{pmin} denotes the smallest noticeable positive contrast to define a bright spot area. We set C_{pmin} =0.03 in all our experiments and let the number of directions in contrast calculation to be N=32. Neighborhood size in contrast calculation is determined by the size of optic disc. On image resolution of size 700x605 or similar, we choose the neighborhood size to be 60. We further use an error tolerance parameter α to relax the threshold so that if $Count(\theta|C_p^{(\theta)} \geq C_{pmin}) \geq \alpha N$, the pixel is then determined to be a bright spot. α is set to be 0.8. Finally, we cluster the detected bright spot pixels to determine the locations of bright spots. Figure 28 shows the example of bright spot area detection on a diseased retina image with hard exudates.

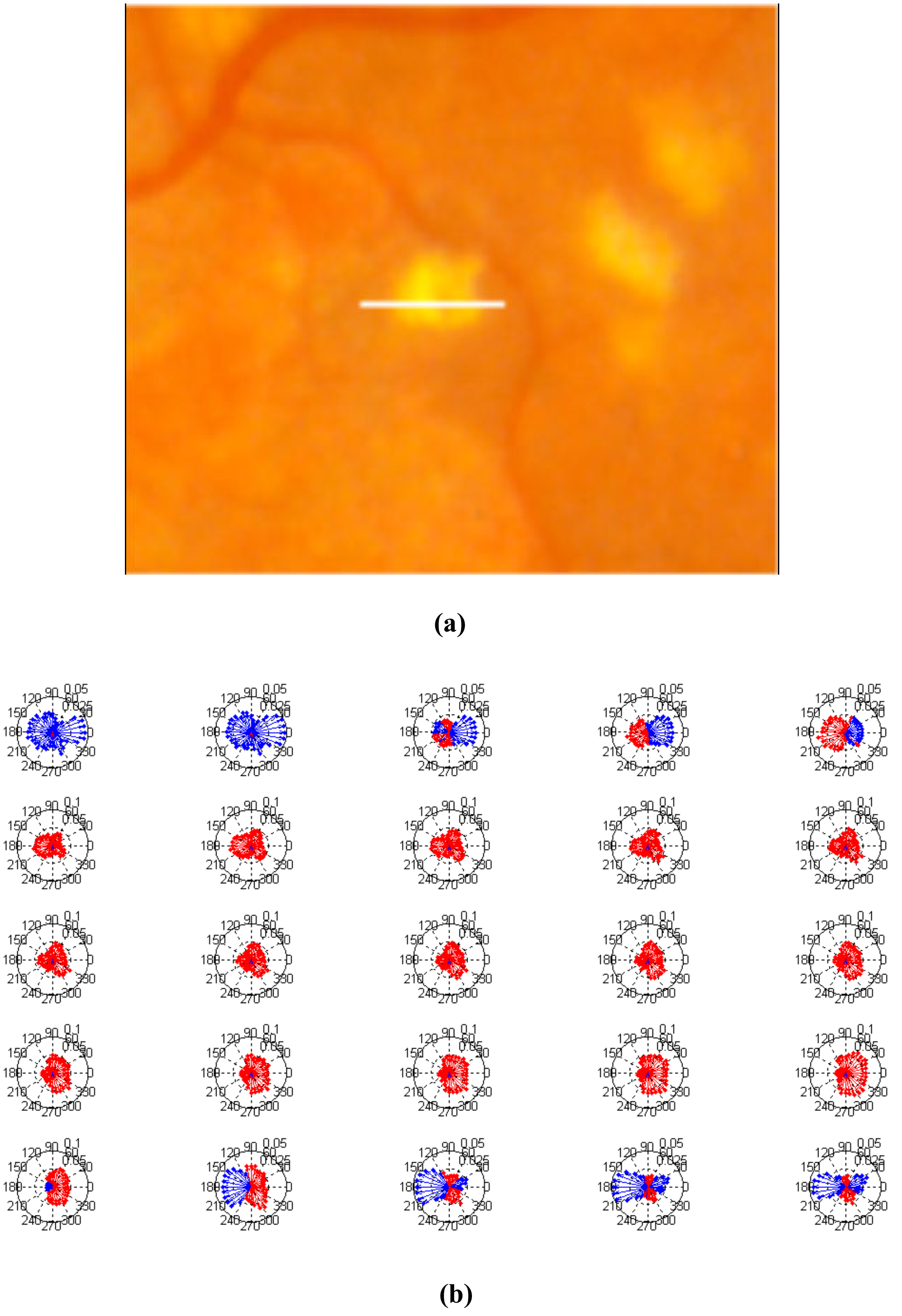

Figure 27: (a) 25 pixels running across a bright spot area. (b) Their corresponding daisy graphs.

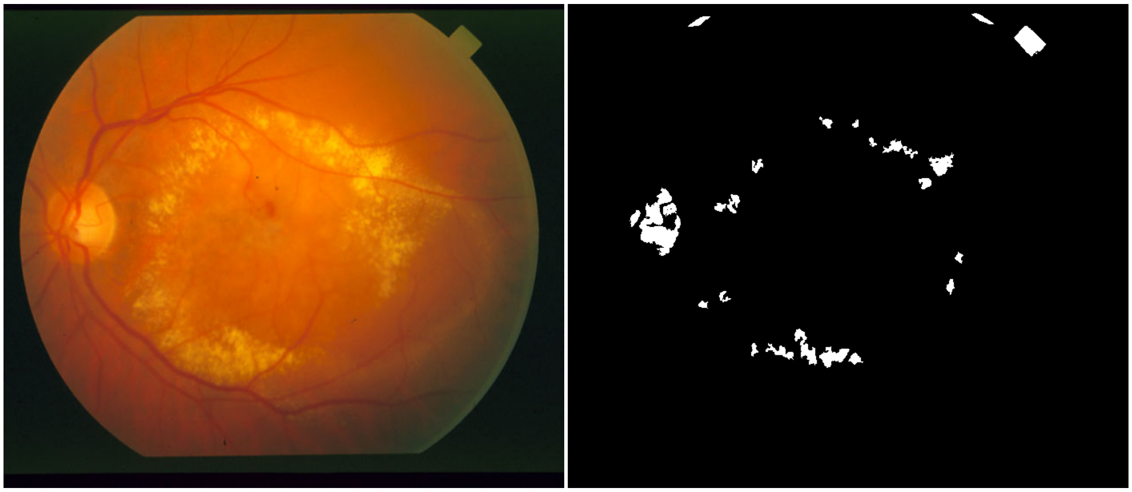

Figure 28: (a) Original retina image with hard exudates (im0002 from STARE). (b) Bright spot detection outcome.

Vessels fircations denote the junction area where large vessel branches furcated into small branches. To detect the fircation areas, we use thinning algorithm on the detected binary vessel map. For each vessel pixel on the resulted thinning map, we count the number of its neighboring vessel pixels within an eight-neighborhood. Vessel pixels having three or more neighboring vessels pixels are extracted as the fircation points. Finally, we cluster the neighboring fircation points together based on their Euclidean distance, such that two or more fircation points within 5 pixels distances to each other are identified as one fircation area. Figure 29 shows the detected fircation areas within the optic disc of a sample image.

Figure 29: Detected fircation area on cropped area around optic disc.

2.3. Feature Analysis of Candidate OD Area

Next we do feature analysis of the candidate OD areas. For each centroid of the candidate OD area, we first use its Euclidean distance to the search center *CtSrh* to characterize its relation to vessel topology. OD is more likely to be close to *CtSrh* due to its fixed relation to vessel network. As such, for each candidate OD area X_i, we denote its relation to *CtSrh* by the following equation.

$$w_{dist} = 1 - \|X_i - CtSrh\|/RadSrh$$

where $\|.\|$ denotes the distance between $X_i$and $CtSrh$. Consequently, the closer X_i is to $CtSrh$, the larger its w_{dist}.

Further, we apply fractal analysis within the candidate areas to identify OD. The identification criterion is justified by the fact that OD is the area where all major vessels merges, and thus presents the highest fractal dimension compared to other bright regions such as hard exudates and artifacts.

Fractal analysis has been widely used and demonstrated its effectiveness in spatial analysis of branching patterns in the fields of biology. Its key and fundamental concept, self-similarity, describes the geometric pattern which remains constant when viewed at different levels of scaling. Fractal dimension, D_f, is a widely accepted and useful quantitative measure of self-similarity for branching pattern object. Numerous medical studies have substantiated the fact that retinal circulation of the normal human retinal vasculature is statistically self-similar. It has been reported with strong evidence that the fractal dimension of the blood vessels within the normal human retina is approximately 1.7 [76]. At the present stage, fractal analysis studies in retinal images focus mainly on region-based quantitative analysis of early-stage vascular disease in the human retina. [91] used fractal analysis to characterize the neovascularisation process in diabetic retinopathy and [92] demonstrated the feasibility of fractal analysis of region-based vascular change in the normal and non-proliferative diabetic retina. In our scheme, fractal analysis is utilized to differentiate OD area from other large and bright regions in retinal images due to the fact that OD area is the converging point of all major vessels, thus presents much higher fractal dimension compared to other bright regions such as hard exudates that are yellow deposits developing after leakage from retinal capillaries [93] and have few blood vessels within and around them.

Fractal dimension is computed within a mask window centered at the centroid of bright spot or fircation area. The window size is selected to be 128 on a 700x605 or similar resolution image, based on the approximated OD size. Box-counting method is used in this paper to calculate the fractal dimension of the binary vessel skeleton for its easy implementation on computer [76]. In box-counting algorithm, the binary image is blanked repeatedly with square boxes of increasing side length (L=1, 2, 4, 8 …, 128). The number of boxes with side length L used (denoted by $N(L)$) are counted if and only if the box contains at least one white pixel. A linear least squares regression is applied to make a log-log plot of $N(L)$ versus L. The negative value of line slope is used as the fractal dimension, D_f.

Combining the two features together, we get a weight for each candidate X_i denoted by the following equation:

$$w_i = w_{dist} * D_f$$

2.4. A Divide-and-Conquer Strategy for OD Localization

Finally, we determine the location of OD area from the candidate areas. Our detection rule is based on a divide-and-conquer strategy according to three different cases.

- *Case 1: Bright spot areas are detected within the search region.*

Vessel topology analysis minimizes our efforts to remove the false detections of OD especially for those diseased objects, like drusens and hard exudates, which are of similar bright colors to OD area. As such, given bright spot areas are detected within the search region, we treat them as the most significant image cues for OD localization. In this case, OD is determined by the detected bright spot with largest w_i value.

- *Case 2: Bright spot areas are not detected within the search region.*

In case of OD is not of bright color, we locate the OD area by a weighting scheme among all the detected fircation areas. As a result, OD is determined to be the weighted average of all the fircation areas denoted by

$$\frac{1}{N}\left(\sum_{i=1}^{N} w_i * x_i,\ \sum_{i=1}^{N} w_i * y_i \right).$$

where, x_i and y_i are the x and y coordinates for X_i, N is the total number of candidate areas.

- *Case 3: Neither bright spot nor fircation areas are detected.*

In some extreme diseased cases, however, optic disc area is neither of bright color, nor there exist vessels around it. Under these circumstances, the only image cue left to use is based on the vessel topology. Consequently, we determine the OD location to be the search center of OD resulted from subsection 2.2.

Finally, we summarize our optic disc localization algorithm as follows in Table 5.

Table 5: OD localization algorithm.

Objective

Locate Optic Disc (OD) Area on Retinal Image.

Algorithm

- ➢ Determine the search area of optic disc.

1. Extract vessel arcade pixels based on *Vessel Topology Map (VTM)* or derived threshold on lognormal curve.
2. Fit vessel arcade pixels to a circle *Arcade_Circle*. Its search radius and center are noted as *RadSrh* and *CtSrh* respectively.
3. Use the fitting error *fit_Err* to approximate the search area of the optic disc.
   (1) If the *fit_Err* >f_T, the search center is around *Arcade_Circle* center.
   (2) Otherwise,
      If left side of the *Arcade_Circle* has more detected BV pixels, the search center is at leftmost side of *Arcade_Circle*. Otherwise, it is at the rightmost side of *Arcade_Circle*.
   For each case, *RadSrh* is decided to be 1/3 of *Arcade_Circle*.

- ➢ Detect feature pixels within *Arcade_Circle* and determine their weights.

4. Detect bright pixels and all the frication areas within the search regions.
5. For each detected feature pixels p_i, calculate its distance $dist(p_i, CtSrh)$ to *CtSrh*, and the BV fractal dimension D_f. The feature weights w_i for p_i is $(1 - dist(pi, CtSrh)/RadSrh) * D_f$

- ➢ Determine the location of optic disc.

6. If there are bright pixels detected, the optic disc is the bright pixel having largest w_i.
   Otherwise, it is determined to be weighted average of all the frication and endpoint pixels denoted by $\frac{1}{N}(\sum_{i=1}^{N} w_i * X_i, \sum_{i=1}^{N} w_i * Y_i)$, where X_i and Y_i are the pixel for each detected frication and end points.
   If neither bright pixels nor fircations, then use the search center as the OD area.

3. Experimental Results and Discussions

We tested our scheme in both DRIVE and STARE image. In DRIVE database, most images are of healthy retinas with bright optic disc areas. In Table 6, we show that our algorithm identifies 40 optic discs out of 40 images in DRIVE database. STARE has more than half diseased images laden with bright color spot areas of drusens and hard exudates. Our algorithm identifies 76 out of 81 images in STARE. We also test the algorithm on images with serious anomalies we collected in our projects and gained a detection rate of 92%.

Table 6: Performance evaluation of OD detection algorithm.

DATABASE	Detection Rate on both Field-1 and Field-2 Type Images
DRIVE	100% (40 out of 40)
STARE	93.83% (76 out of 81)
Our Database (from clinics)	92% (823 out of 895)

Our divide-and-conquer strategy shows strong ability in dealing with both normal and diseased retinas. Several examples of OD detection results are shown in Figure 30. (a) and (b) are the detection outcomes on field-1 images. (c),(d),(e) are images laden with deposits of hard exudates and drusens. (f) and (g) show the images whose OD are not of bright colors. (h) is an image whose vessels around the OD come to degenerate. Our divide-and-conquer strategy using both vessel topology analysis and bright spot detections enables us to locate OD of shallow appearances and greatly improve the false detection rates when diseased objects exist.

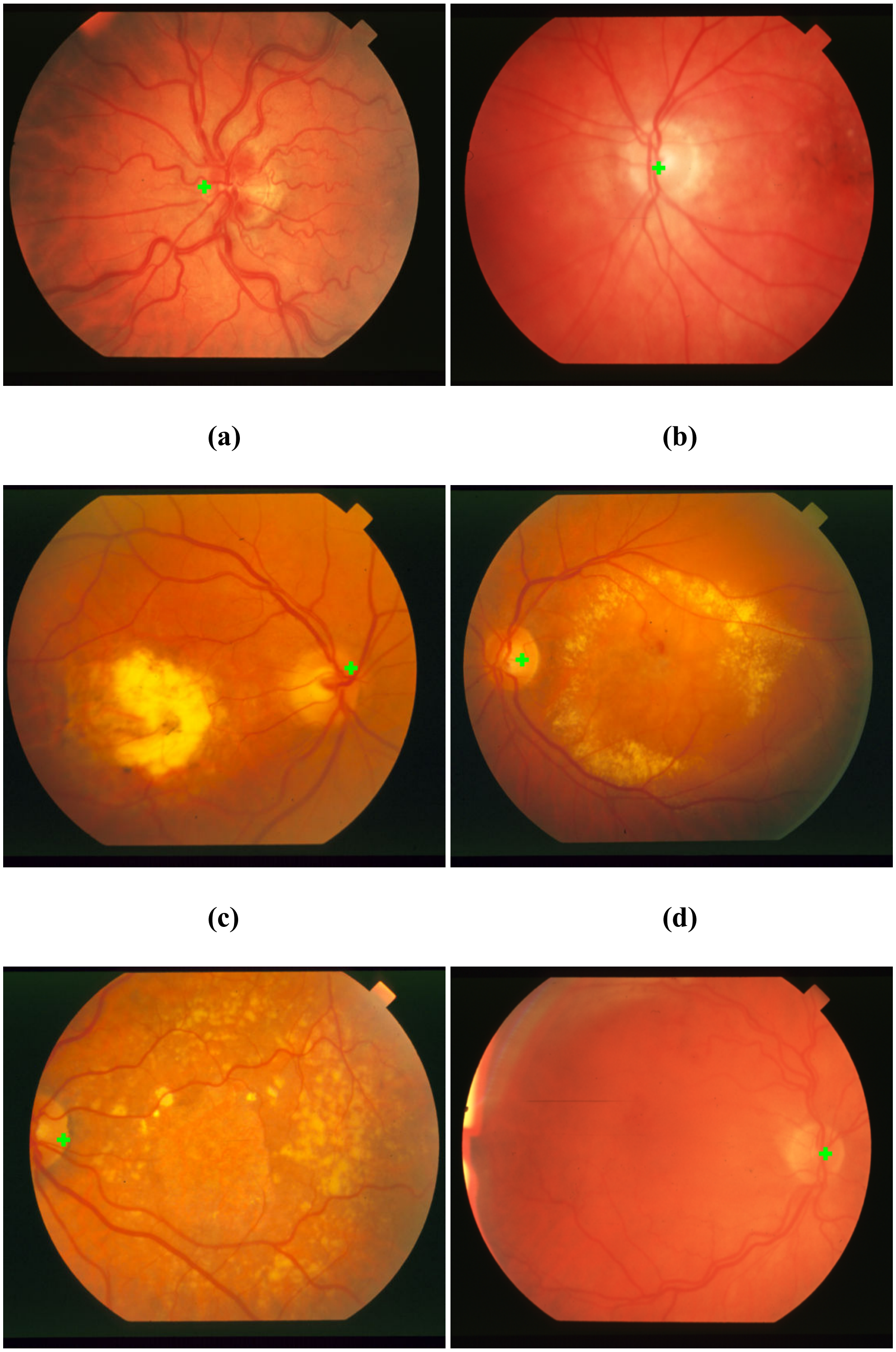

(a) (b)

(c) (d)

(e) (f)

Figure 30: OD localization results. The green "+" is the located OD.

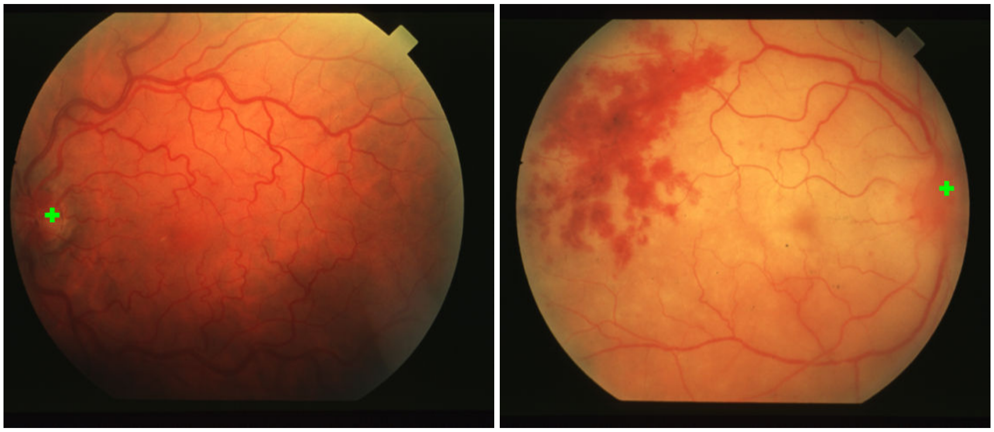

(g) **(h)**

Figure 30 continued.

The algorithm may fail in some extreme cases when the imaging condition of the image is too poor. Under these circumstances, the blood vessels are too shallow to be detected, given not manually adjusting the sensitivity level. It therefore makes the topological analysis of vessel network unreliable. On these images, our algorithm can not accurately locate OD. An example is shown in Figure 31. In this case, blood vessels around and within the optic disc area are not reliably detected if not increasing the detection sensitivity in BV mapping algorithms. Thus, our OD detection algorithm fails to accurately locate the search region of OD and make the false detection.

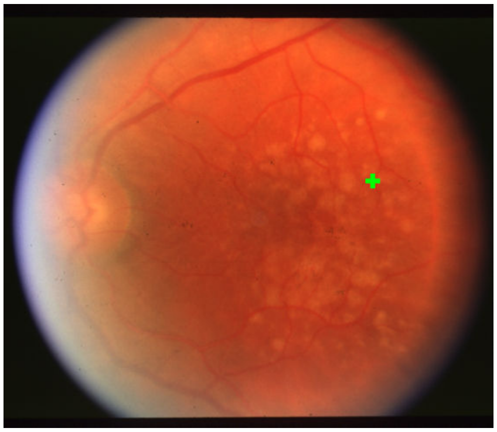

Figure 31: False detection of OD.

E. Summary of the Chapter

In this chapter, we introduce algorithms for the segmentation three landmark objects on retina images, blood vessel network, macula-fovea area and optic disc. Our BV detection algorithm derives from our modeling technique in the previous chapter. Using the modeling technique, we can adaptively tune the detection parameters by probing statistics resulted from Sobel edge detections on retina images. Based on their fixed locations to vessel network on field-1 and field-2 retina images, we can further locate M-F and OD area using vessel topology analysis. All our detection algorithms have been tested on both benchmark image databases as well as the images collected from on-site clinics and demonstrate high performance compared with state-of-art algorithms in terms of both detection accuracy and computational cost. In the next chapter, we further use the segmented landmark objects to develop high level applications on retinal images.

CHAPTER V

HIGH LEVEL APPLICATIONS ON RETINAL IMAGES

A. Overview of the Chapter

Based on the algorithmic results from the previous two chapters, in this chapter, we develop high level applications on retinal images in retinal image database. We start with the texture analysis and classification of the macula-fovea area on retinal images. People belonging to different population groups in their ages and retinal health conditions are related to different appearances within and around their macula-fovea areas. Texture analysis of macula-fovea area helps to group retinal images according to their population groups. We use the entropy statistics from the Gabor responses of automatically extracted macula areas as their texture features. By doing linear discriminant analysis (LDA), texture features belonging to three population groups (healthy young, normal middle age and diseased retinas) are well separated and classified on the resulted feature space. We continue to use LDA as the numerical feature values to represent the texture of macula-fovea area and develop an analytical method to quantify the correlation between the texture of the macula-fovea area and the structures of vascular network. With respect to the vascular network, we extract local features of furcation point count, lengths, curvatures, and fractal dimensions to characterize the morphological pattern of vessel structure. The correlation analysis between the two is performed based on a standard univariate correlation technique. The purpose of our data-driven approach is to identify where and how change of local vascular morphology is correlated to the change in macula-fovea texture. The analytical result is thus to contribute our knowledge of the underlying interaction between the two organelles. Finally, we apply our analytical results to the design of an algorithm for the similarity-based ranked retrieval of retina images on retinal image library.

B. Texture Analysis of Macula-fovea Area

People belonging to different population groups are associated with different appearances in their macular structures. In this work, we study retinas of three population groups, namely, normal middle-aged retina, healthy young retina and diseased retinas.

Figure 32 shows the typical samples of macula areas of each group. In general, different macular types differ in their spatial distributions of pixel intensities within the localized macula area. Normal middle aged macular areas present homogeneous spatial distribution of pixel intensities along different directions (see row 1). Macular areas in row 2 have white fiber-like tissues around the centered fovea areas, which are the reflections off the glossy surface of the retina that are typically observed in young retinas. In contrast to the healthy macular structures, degeneration in macular structures (see row 3) is usually accompanied with the appearances with diseased objects like drusen or hemorrhages. Intensity distribution within these structures is highly disordered due to the irregularities in disease formations.

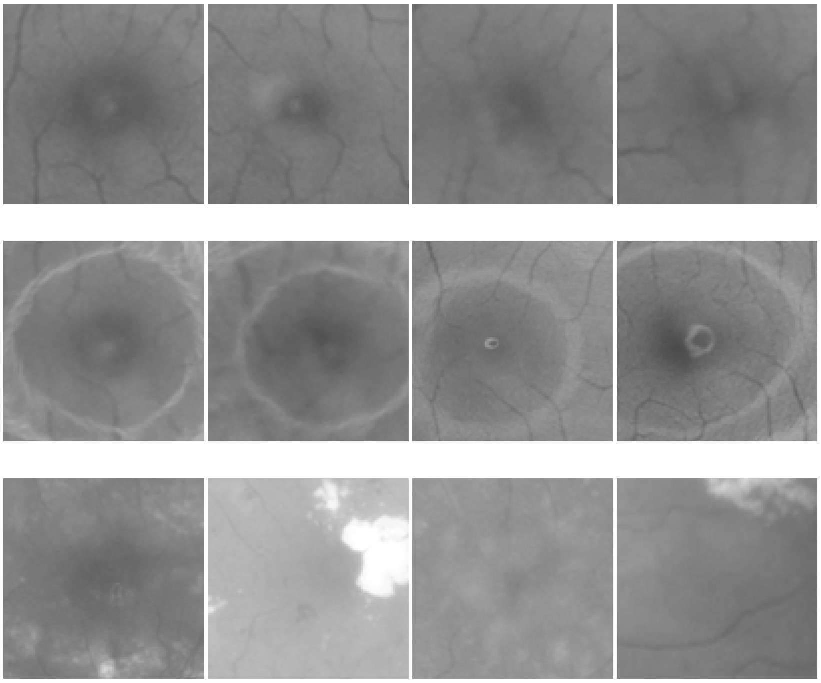

Figure 32: Macula structures for different population groups of normal middle aged retinas (row 1), healthy young retinas (row 2), diseased retinas (row 3).

We develop texture analysis technique to quantify and separate the macula-fovea areas belong to the three population groups. To represent the homogeneity in spatial distribution of pixel intensities, we extract features on macular areas based on the entropy statistics of two dimensional Gabor filtered response. A 2D Gabor filter is, basically, a Gaussian filter modulated by a complex sinusoid pointing toward a specified direction. It is denoted by the following equation.

$$G(x,y,\theta,f) = \exp\left\{-\frac{\left[\left(\frac{x}{S_x}\right)^2 + \left(\frac{y}{S_y}\right)^2\right]}{2}\right\}\cos\,(2\pi f x)$$

$$\mathrm{x}' = \mathrm{x}\cos\theta + \mathrm{y}\sin\theta$$

$$\mathrm{y}' = \mathrm{y}\cos\theta - \mathrm{x}\sin\theta$$

where, S_x and S_y are the variances along x and y directions respectively, f is the center frequency of the sinusoid and θ is the direction of the Gabor filter. Gabor filter has been widely used in algorithms design for object detection and texture analysis [93][94][95][96][97]. Typical use of Gabor filter is to tune its parameters so as to match the shape and size of the target object. Instead of direct usage of Gabor filter to do object detection, we use the entropy statistics of the Gabor filtered response macular images to characterize the homogeneity of the macular structures. Entropy [98] is denoted as:

$$-\sum_{\mathrm{i}} \mathrm{p_i}\log\,(\mathrm{p_i})$$

where, $\mathrm{p_i}$ is the probability that the texture image contains a specific intensity value i. In general, the Gabor filtered response image is of complex value. To use the entropy measure, we first do a quantization on the absolute value of the Gabor filtered image. We set 256 bins, with the bin integer values ranging from 0~255, which denote the intensity level i of the quantized filtered image. For the filtered image having Gabor response bigger than 255, we truncate the value to 255 and for the others we round the value to the nearest bin integer. $\mathrm{p_i}$ is used to denote the histogram counts for each intensity value i on the filter response image. For given set of the intensity values on the filtered image, the entropy measures the degree to which the histogram counts spread out over different possible response values. Intuitively speaking, macular areas of homogenous textures have more localized histogram distributions of filter responses as compared with that of diseases macula whose histogram distributions of filter responses would spread. Therefore, we can represent different macular structures by their entropy statistics. Tuning the Gabor filter to different frequencies and angles, we obtain the entropy statistics under different spreading and directional factors and compose a high dimensional feature vector. We choose S_x, S_y and f range in values 2, 7 and 12 and θ range in values 0, $\pi/4$, $\pi/2$, $3\pi/4$. Choice of values in S_x , S_y and f is based on our approximation of diseases patterns in different shapes, sizes and varying factors on the cropped image resolution of size 100x100 and on our empirical results of classification rates. Our proposed angular resolution for Gabor filter is $\pi/4$. Consequently, we obtain a high dimensional feature vector of dimension 3x3x3x4=108.

Feature vector derived from Gabor filter responses is of high dimension. Due to the curse of dimensionality problem [99], we further use Linear Discriminant Analysis (LDA) to perform dimensionality reduction while preserving as much of the class discriminatory information as possible. The main idea of LDA is to find an order of projections that maximizes the ratio of between-class discriminant measure to within-class discriminant measure [99]. Using LDA, we project the feature vector of dimension 108 to the two most discriminatory dimensions and obtain a reduced feature space of 2 dimensions.

There were 70 cropped normal middle aged, 75 healthy young and 35 diseased macula-fovea areas used as the training set for LDA of macular textures. Due to the shortage of diseased macula-fovea areas in our dataset, for each diseased macular area, we further cropped the areas on original retina images centered 50 pixels apart left and right, top and down from the original cropped center to increase the number of training images. Scatter plot of the LDA result for the training data is shown in Figure 33. Macula textures belonging to three different population groups are well separated from each other on the resulted scatter plot.

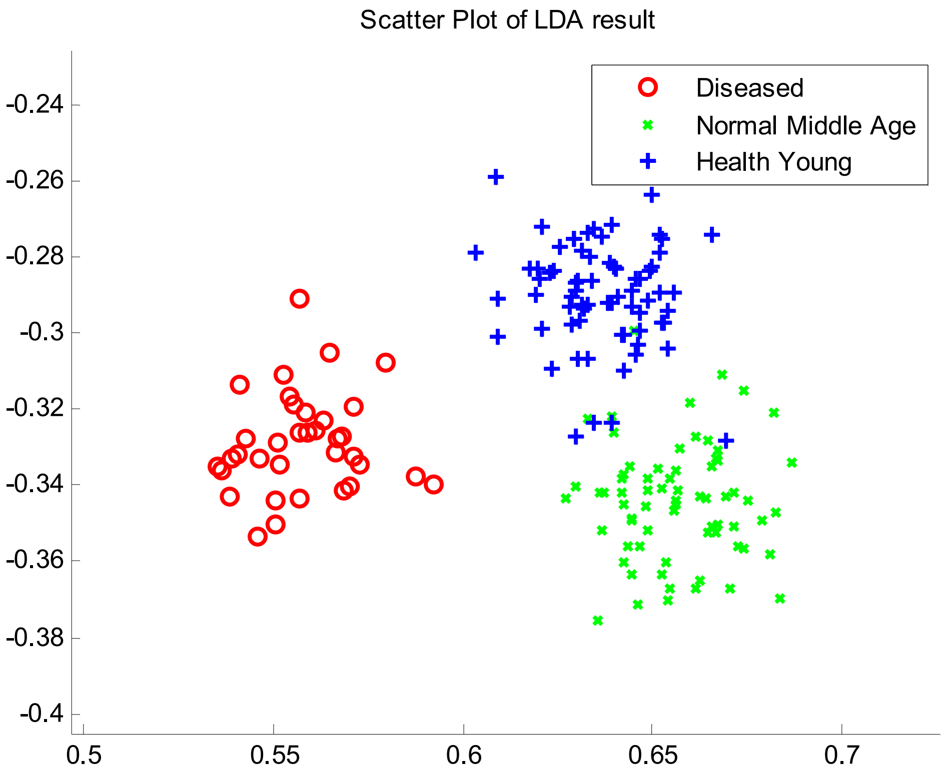

Figure 33: Scatter plot of the LDA result of texture analysis of macula structure.

To testify the capability of the LDA result on classifying unknown macula images, we use a test data set of 70 cropped normal middle aged, 75 healthy young and 35 diseased macula-fovea areas. We project the feature vector extracted from each unknown test image onto the derived feature space and do the classification based on k-nearest neighbor classifier. Table 7 shows the classification rate using different k numbers. Our approach reaches the highest classification rate of 85% on the test data set when k is equal to 3, 5 or 7. Empirical results also show that, given the increase number of dimensionality of the extracted feature vector by adding to the different values of S_x , S_y , f and θ, we will run into the typical over-fitting problem. That is, the clusters of macular textures belonging to different population groups are more separated from each other while the classification rates on the test data comes to be lower. Selections of parameters in S_x, S_y, f and θ are thus based on best empirical tradeoff results on both training and test data sets.

Table 7: Classification rate of macular texture using different k numbers.

	K=1	**K=3**	**K=5**	**K=7**	**K=9**	**K=11**
Classification Rate	84.44%	85.00%	85.00%	85.00%	84.44%	84.44%

On top of the classification of macular textures among different population groups, our proposed approach provides a numerical tool to quantify the difference between macular structures. In next session, we use it to continue our correlation study between macula-fovea textures and vascular network structures.

C. Correlation Analysis between Macular and Vascular Features

In a retina, the blood vessel network and the macular area are two of most noted organelles. The macula-fovea area is a small circular area responsible for sharp vision. The macular-fovea area is mostly connected to terminating points of the blood vessel network to receive nutrients and expel wastes permeated through capillaries. Despite of their tight relationship at the cellular level, the two organelles exhibit very different dynamics in response to diseases and aging. The macular area mostly changes in its textural appearances, with relatively subtle changes in shapes. On the other hand, vascular networks exhibit highly dynamic changes in widths, lengths, curvatures, furcation points and fractals, etc., with respect to aging or presence of diseases. Any (non-macular) disease that affects the performance of the vascular network will affect the functionality of the macular subsystem. On the other hand, when the macular subsystem is sick, it may also signal the blood vessel network to change its structure as a part of the biological feedback loop. Even though the clinical studies did confirm the existence such relationships [100][101][102][103][104][105], as of now there are few studies which quantify the nature of these relationships on retinal images.

The most precise clinical procedure to study this type of problems should have decades of follow up studies on individuals with controlled conditions. Given the very high cost of running this type of investigations, due to the ultra low rate of changes, it is critical that we first have some credible evidences to make pivotal decisions on how to research on most promising hypotheses. To achieve this goal, we formulate this problem from the viewpoint of population statistics. The first key issue is whether or not there exist strong, highly distinguishable patterns for the objects of interest such as blood vessels, macular-fovea textures, etc. for different population groups. Our investigation found that the answer is affirmative for selective blood vessel structures and macular-fovea textures.

Based on these observations, we propose a new technique to simulate changes of a subject's conditions in the population macula texture feature space with the feature distances from a sample S to centroids C_Y, C_M, C_D, of features from groups young-healthy (G_Y), mid-age healthy (G_M) and diseased (G_D). A (statistical) condition change is said to occur to the feature of a subject S in a particular group G_x, when its feature is not closest to C_x based on a feature distance function with respect to the three centroids.

The first inferred statistical change: *I1: "S is deviating from* G_x *to some other state".*

The objective of the correlation study is: *"Given I1, what are correlated changes in blood vessel structures?"*

This represents a case of general population study without excluding any subgroups from the study. In the second type of study, we are interested in finding more refined relationship between three groups based similarly defined (statistical) changes for "from G_Y to G_D", "from G_Y to G_M", and "from G_M to G_D". Without loss of generality, let us assume that S is known in G_Y, yet its feature distance functions for C_Y and C_M show that it is closer to C_Y, not C_M. We note that in this step, C_D is not used for evaluation of the distance functions.

In this case, make the statistical inference that "the feature of S likely represents change when a normal subject in G_Y begins to migrate toward the group G_M", or

I2: "from G_Y to G_M".

The objective of our statistical analysis problem is: *"Given I2, what are correlated changes in blood vessel structures?"*

A similar argument can be made to *I3: "from G_M to G_D",*

Its statistical analysis problem: *"Given I3, what are correlated changes in blood vessel structures?"*

Due to lack of data for the case of from G_Y to G_D, in this work we will concentrate on the two statistically inferred state migration cases only. To answer these interesting and challenging questions, we take a univariate correlation analysis technique to investigate the relationship between changes in macular textures and changes of blood vessel structures among different regions within the field of view of a retinal image, based on the field-2 type images.

Textural change within macula-fovea area can be quantified based on the derived LDA result in previous subsection. With respect to vascular network, its structural change is mostly manifested by the local change in vessel morphology, such like proliferation, degeneration, bending, etc, due to the blockage of blood and nutrients supply. As such, in the following we do regional analysis to characterize the structure of the whole vascular network.

1. Frame of Reference on Retinal Image

The presented correlation analysis is based on 96 sample images acquired from clinic study, which include 40 healthy young retinas, 41 normal middle age retinas and 15 diseased retinas with macula diseases. Resolutions of the studied retina images are all of 720x480 and all are of field type-2 with complete field clarity and 60º angle of view. Medical study rigorously defined nine regions, namely, optic disc, macula, temporal, superonasal, inferonasal, superior, inferior, superotemporal and inferotemporal on a field type-2 retina image, based on the fixed relations among the retina objects,. We automate the process of establishing a frame of reference on retinal images by the detection result of BV, M-F and OD. Using the M-F as the center and its distance to OD as the radius, we draw a circle on the retina image to track the extension of vessel arcades and identify the nine regions on retina images. Centers of each region are of 45º apart from each other along the drawing circle and window size of each region is of 256x256 (see Figure 34).

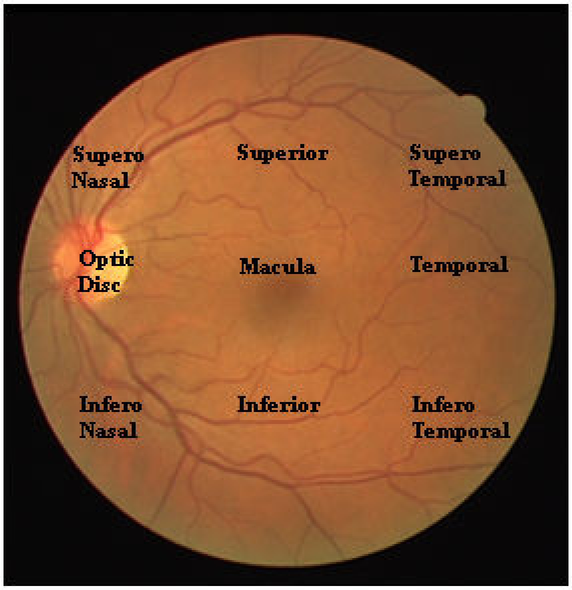

Figure 34: Frame of reference on retinal image.

2. Feature Extraction of Vascular Network

By the establishment of frame of reference, different field type-2 retinal images can be aligned with each for analysis. On each identified local area, we extract four feature types of vessel structures, namely, fractal dimension, number of furcation points, mean value of segment lengths and mean value of vessel curvatures.

(1) Fractal Dimension (D_f)

Similar to our discussion for OD detection in Chapter IV, subsection D, here we use fractal dimension as a geometric index to quantify the self-similarity of geometric object. Medical study substantiated its use in classification of population groups in terms of varying degrees of vessel degradations. We use similar approach of box-counting method to calculate the fractal dimension. The window size for fractal calculation is set to be of 256x256 with the maximum side length being equal to 256.

(2) Number of Fircation Points (N_f)

Fircation point denotes the junction area where large vessel branch furcates into small branches. Abnormality in the increase or decrease in fircation points is a significant sign of vessel proliferations or deaths. Extraction of fircation areas is same with the method discussed in OD localization. Within each identified local area, we use the number of its detected fircation points as the feature entry.

(3) Mean Value of Segment Lengths (M_l)

A vessel segment is the set of connected vessel pixels between the two neighboring fircation points on a skeleton BV map. We use the center of the vessel segment to denote its location. Length of the vessel segment denotes the continuity of its growth. It is calculated by the number of pixels in each vessel segment. We exclude the vessel segments which are of less than 10 pixels in length (minimal vessel segment length (*minSegLen*) defined, which will also be used in the curvature calculation in the following discussion), so as to minimize the noise effects in the vessel segmentation and thinning process. Within each local area, we calculate the statistical mean for all included vessel segments.

(4) Mean Value of Segment Curvatures (M_c)

Measurement of the bending property of the vessel segment is another important cue for retina blood vessel health. Normal retina blood vessels are usually slightly curved while under diseased condition, they change to be more tortuous due to the stretching and high congestion in vessel growth. [106] proposed their method in measurement and classification of the retina vascular curvature. We use their method to quantify the curved nature of vessel segments. The curvature of a point p on a curve is defined as the derivative of the angle of the tangent line $\alpha(p)$ at the point with respect to the arc length of the curve $s(p)$ within the calculated window size. The window size is chosen to be *minSegLen*=10, based on our definition of minimum segment length. The arc length *s(p)* is determined by summing the Euclidean distance of the neighboring pixels within the window size and *α(p)* by calculating the angle of the line connecting the neighboring pixel. Derivative of *α(p)* with respect to *s(p)* on p is the slope of a fitted line $f(x) = kx + b$ by minimizing the summation of the square error between *α(i)* and $f(i)$ using linear regression method, where i denote the index of points within the window size around point *p (p-minSegLen/2, p-minSegLen/2+1,...p+minSegLen/2-1)*. For each vessel segment, we use the highest curvature among the points on the curve to denote its bending property. Finally, within each region, we calculate the mean value of the segment curvature for all the included vessel segments to characterize its regional curvature.

3. Correlation Analysis

After obtaining the features characterizing both the vascular network pattern and macular textures, we do correlation study between the two organelles. Assume that number of sample data is N. Let X_1, X_2, … X_N be the vessel feature vectors of the N sample image, where X_i is a M x 1 column vector $[x_i^1, x_i^2, x_i^3, \ldots, x_i^M]^T$ and M the number of feature elements of the vessel feature vector derived from our previous discussion, which is equal to 4x9=36. Let V_1, …V_N be the macular texture feature vector, where V_i contains number of K elements of macular texture feature from 2D LDA space for the *i-th* image, which is equal to 2. These data are presented in the M x N and K x N matrices, i.e., $X=[X_1, X_2, \ldots, X_N]$ and $V=[V_1, V_2, \ldots, V_N]$, respectively.

To derive the correlation between the structural change in vascular feature and that in the macular textures against different statistical conditions (*I1, I2* and *I3*), for each trained sample feature data that belongs to a certain class, we do a normalization process for each entry in the feature vectors for both vascular network and macular structure.

First, for vascular feature vector $X_i = [x_i^1, x_i^2, x_i^3, \dots, x_i^M]^{\mathrm{T}}$, it is transformed into a new feature vector $Y_i = [y_i^1, y_i^2, y_i^3, \dots, y_i^M]^{\mathrm{T}}$, where for each entry of y_i^m in Y_i,

$$y_i^m = \frac{x_i^m - \mu_i^m}{\sigma_i^m}$$

μ_i^m and σ_i^m are, respectively, the entries for the mean and standard deviation vector of vessel features for the class which X_i belongs to.

Next, we derived the change of the macular texture for a given subject *S* in a particular group G_x against three (statistical) conditions *I1, I2* and *I3*.

(1) I1: "S is deviating from G_x *to some other state".*

For macular texture feature vector $\mathrm{V_i} = [v_i^1, v_i^2]^{\mathrm{T}}$, we transform it into a new feature vector $\mathrm{W_i} = [\mathrm{w_i}]$, where

$$\mathrm{w_i} = \frac{\|\mathrm{V_i} - \mathrm{C_i}\|}{\|\mathrm{V_i} - \mathrm{C_j}\| + \|\mathrm{V_i} - \mathrm{C_k}\|}$$

$\mathrm{C_i}$ is the mean macular feature vector (centroid) of the class to which the sample belongs to, and $\mathrm{C_j}$ and $\mathrm{C_k}$ are the mean macular feature vectors (centroids) of the classes that the sample do not belong. $\|.\|$ denotes the distance between two vectors. By design, larger value of $\mathrm{w_i}$ indicates that the macular structure of the sample instance is more different from the typical macular structure that the instance belongs to, while smaller value of $\mathrm{w_i}$ indicates that it is more of the typical structure of its category. See illustration in Figure 35.

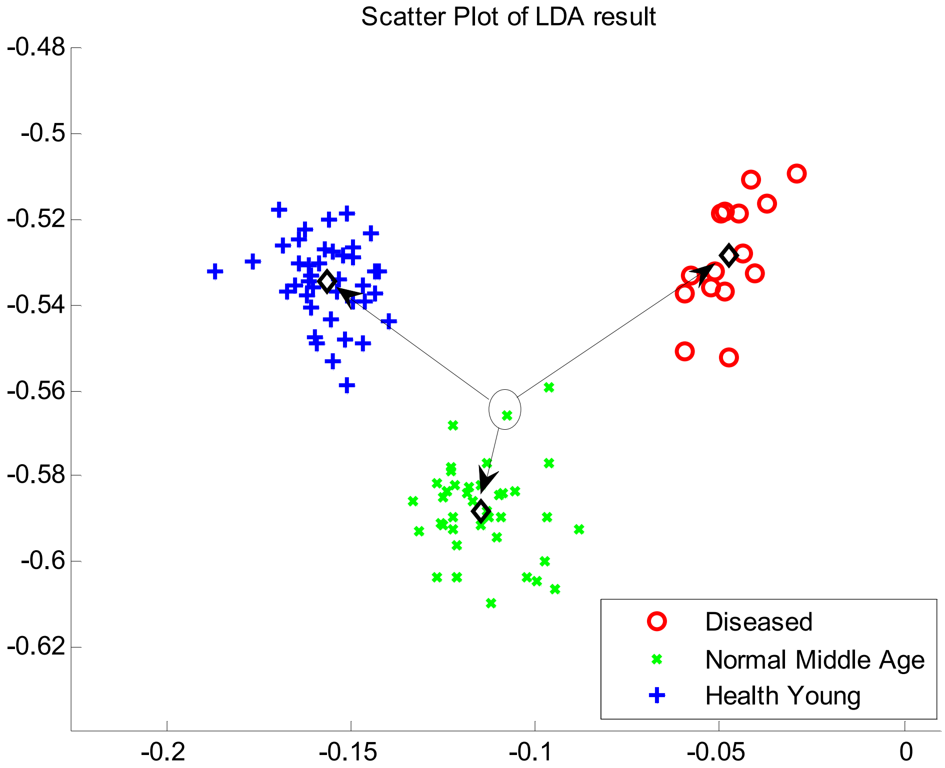

Figure 35: Distances between a particular subject to the three group centroids on LDA macular feature space.

(2) I2: "from G_Y *to* G_M*".*

In this case, we focus on the textural feature for the population group of healthy young retinas G_Y and are interested in its transition to normal middle aged retina G_M. For given *S* of G_Y we define its similarity measure with regard to both two groups based on the ratio of distances as follows.

$$\mathrm{w_i} = \frac{||\mathrm{V_{iY}} - \mathrm{C_Y}||}{||\mathrm{V_{iY}} - \mathrm{C_M}||}$$

where $\mathrm{V_{iY}}$ denotes the texture feature vector for each *S* in G_Y, $\mathrm{C_Y}$ and $\mathrm{C_M}$ are the centroids for G_Y and G_M respectively. $||.||$ denotes the distance between two vectors. Accordingly, larger value of $\mathrm{w_i}$ indicates that the macular structure of the sample instance is more different from the typical macular structure of $\mathrm{C_Y}$ but more like that of $\mathrm{C_M}$, while smaller value of $\mathrm{w_i}$ the other hand.

(3) I3: "from G_M to G_D".

A similar derivation to *I2* can be conducted in case of *I3* to characterize the textural feature for the population group of G_M transitioning to G_D. In this case,

$$\mathrm{w_i} = \frac{\|\mathrm{V_{iM}} - \mathrm{C_M}\|}{\|\mathrm{V_{iM}} - \mathrm{C_D}\|}$$

where $\mathrm{V_{iM}}$ denotes the texture feature vector for each S in G_M, $\mathrm{C_M}$ and $\mathrm{C_D}$ are the centroids for G_M and G_D respectively. $\|.\|$ denotes the distance between two vectors.

Let $Y_1, Y_2, \dots, Y_N$ be the normalized vessel feature vectors of the N sample image, where (Y_i is a M x 1 column vector $[y_i^1, y_i^2, y_i^3, \dots, y_i^M]^T$), and M the number of feature elements of the vessel feature vector, which is equal to 36. Let $W_1, W_2, \dots, W_N$ be the normalized macular texture feature vector, where W_i is a one-dimensional feature $W_i = [w_i]$ for the *i-th* image. These data are presented in the M x N and 1 x N matrices, i.e., $Y = [Y_1, Y_2, \dots, Y_N]$ and $W = [W_1, W_2, \dots, W_N]$, respectively. We take standard univariate correlation analysis to calculate the correlation between each vessel feature entry y_i^j and macular feature $\mathrm{w_i}$ as follows:

$$\rho_{jw} = \frac{\sum_{i=1}^{N}\{(y_i^j - \mu_j)(\mathrm{w_i} - \mu_w)\}}{N\sigma_j\sigma_w}$$

μ_j and μ_w are the means of y_i^j and $\mathrm{w_i}$. σ_j and σ_w are the standard deviations of y_i^j and $\mathrm{w_i}$ respectively.

Value of the correlation coefficient ρ_{jw} is within {-1, 1}. Mathematically, positive and negative signs of the correlation coefficient indicate positive and negative correlations respectively. Comparing the absolute values of the entries in m, we are able to identify the dominating regional features of vessel network that show the strongest correlations to macula-fovea area against different (statistical) conditional changes in macular textures. Larger (smaller) positive value in ρ_{jw} indicates that the farther the macular structure of the sample data is away from the centroid of the class the sample belongs to, the more the identified vessel feature index will surpass (be below) its average level (i.e., mean value). On the other hand, larger (smaller) magnitude in negative value for ρ_{jw} indicates that the farther the macular structure of the sample data is away from the centroid of the class the sample belongs to, the more the identified vessel feature index will be below (surpass) its average level (i.e., mean value).

4. Experimental Results

Figure 36 shows the four vessel feature (D_f, N_f, M_l, M_c) plots of different population groups. On each vessel feature plot, x axis denotes the region on retina and y axis denotes the mean value of the corresponding regional feature for the population group. Error bar on the plot is determined by the value of standard deviation.

Firstly, we compare the vessel features of healthy young and normal middle aged retinas. On different regions, young retinas are found to have higher fractals, larger number of fircations but shorter segment lengths than normal middle age retinas. Vessel segments in optic disc area of young retinas will be less tortuous than that of normal middle age retinas. These comply with the anatomic findings of vessel growing on retina in that in its young age, vessels flourish and furcate into many small branches. And when the retina is aging, vessel degenerates and the small branches decay. For diseased retinas, they have less fractals and less fircation numbers against different regions on retinas as compared to young and middle age counterparts. This is substantiated by the fact that in diseased conditions, malfunctioning of retinas leads to even more severe degradation of vessel structures. Diseased retinas also have more curved vessel segments in optic disc and superonasal areas but not the rest and their segment lengths in optic disc and superior areas are larger. Compared to the young and middle age retina, they have relatively higher deviations in vessel features. This results from the fact that patterns of diseased formations in their locations and severity vary among different diseased retinas in the collected sample data.

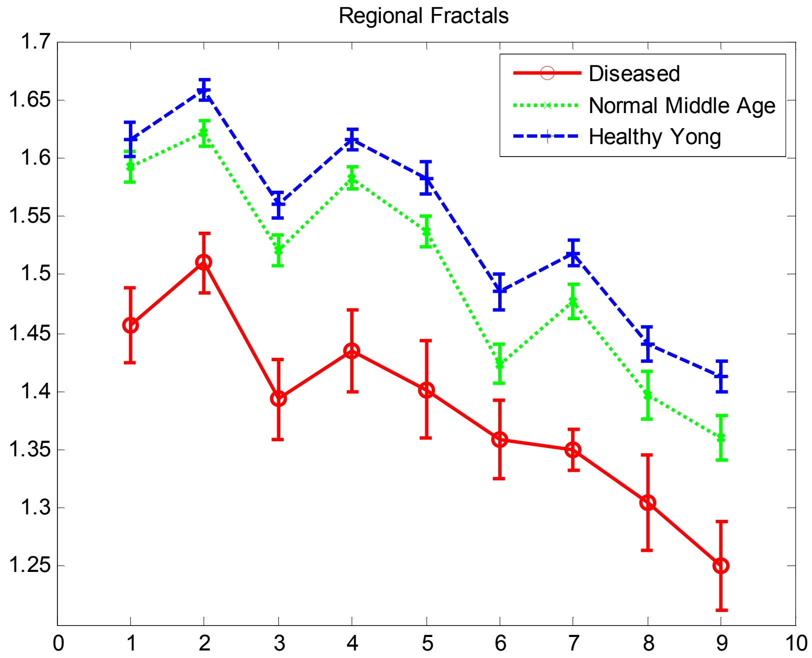

(a)

Figure 36: Plots of the mean values for different types of vessel features against different regions on retinal image. (a),(b),(c),(d) denote the vessel features of D_f, N_f, M_l, M_c respectively. On each plot, "1" to "9" on the x-axis denote the defined local regions on retina image of "Macular", "Optic disc", "Temporal", "Superior", "Inferior", "Superonasal", "Inferonasal", "Superotemporal" and "Inferotemporal" respectively.

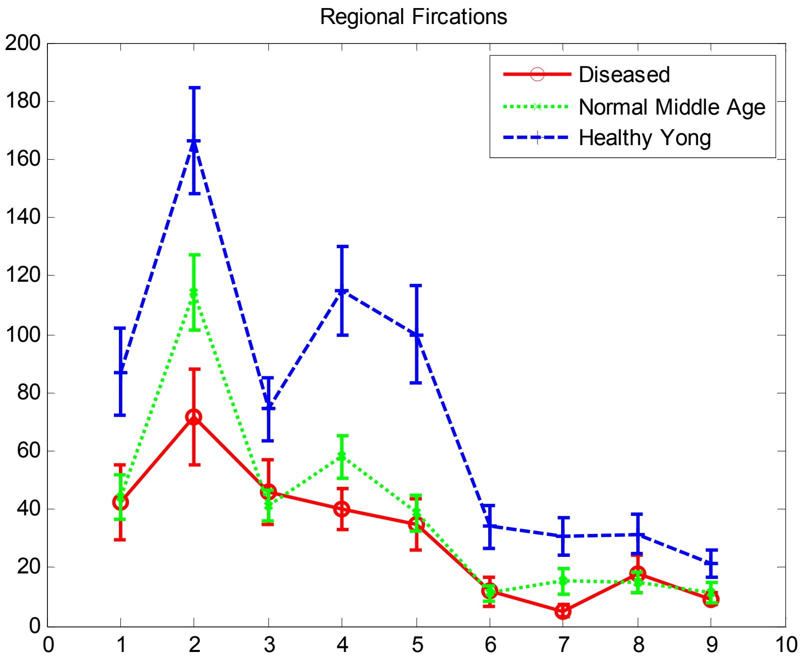

(b)

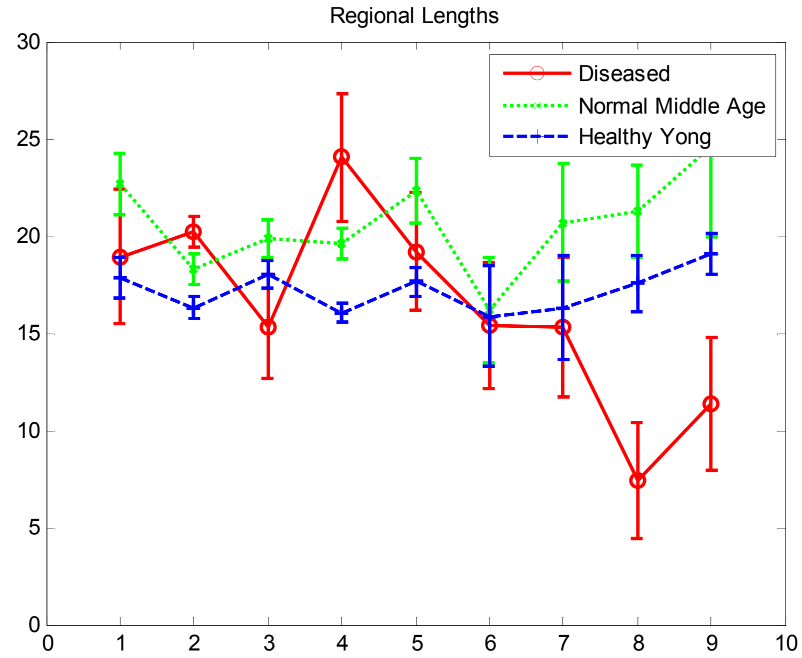

(c)

Figure 36 continued

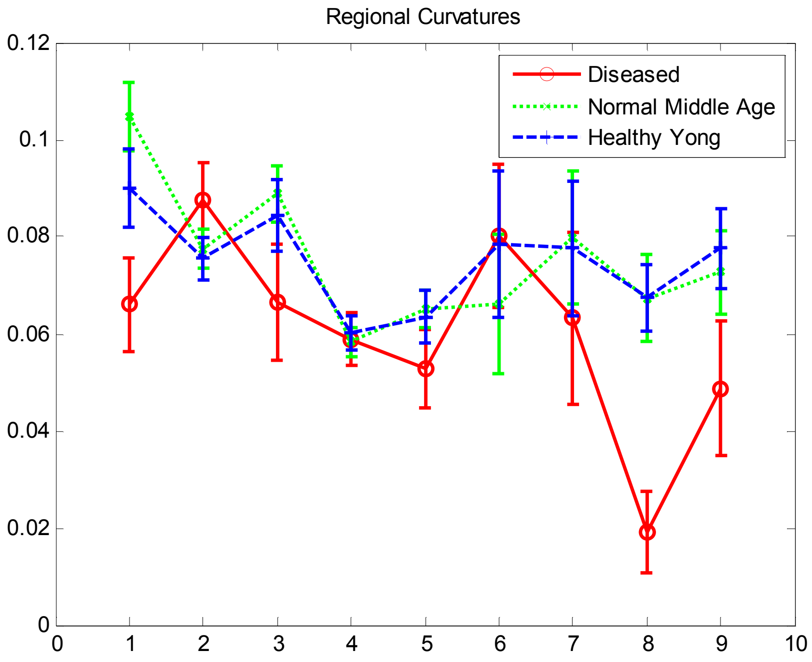

(d)

Figure 36 continued.

The above regional feature analysis characterizes the vascular network structures for different population groups. Next, we show the correlation between vascular network structure and macula-fovea textures against different (statistical) conditions.

(1) *I1: "S is deviating from* G_x *to some other state".*

(2) *I2: "S is deviating from* G_Y *to* G_M*".*

(3) *I3: "S is deviating from* G_M *to* G_D*".*

For each condition, calculated correlation coefficients for each entry of vessel feature with respect to macula texture are shown in the following tables. The last row and column on each table is the mean of absolute values for the entries in each corresponding row and column. Within each table, we identify the three feature entries that have strongest positive and negative correlations to macular texture and mark them with red and blue colors respectively. We are also to infer in average, which feature type of vessel structure and which area have largest correlation to macular texture by comparing the values in last row and column respectively and mark them with yellow color.

In Table 8, experimental results show that in case *I1,* when a subject *S is deviating from* G_x *to some other state* in the macular texture feature space, structures of vessels in superonasal area have strongest correlations with changes of macular structures and with fractal dimensions of vessels the most notable descriptor. More specifically, fractals dimensions in superior area, vessel curvatures and lengths in superonasal area are the three most pronounced feature indicators. On the other hand, little or no correlation exists for vessel features in temporal area.

Table 8: Calculated correlation factors under statistical condition *I1*.

Region #	Region name	Fractals	Curvatures	Fircations	Lengths	Absolute mean
1	Macula	-0.1465	-0.0798	-0.1434	-0.0321	0.1005
2	Optic Disc	-0.1699	-0.1762	-0.1887	0.0691	0.1510
3	Temporal	-0.0336	0.041	0.0396	-0.119	0.0583
4	Superior	-0.26	0.1124	-0.1161	0.0516	0.1350
5	Inferior	-0.0973	0.1234	-0.1916	-0.0617	0.1185
6	Superonasal	0.138	0.3011	0.1497	0.2954	0.2211
7	Inferonasal	0.202	0.1674	0.1347	0.1512	0.1638
8	Superotemporal	0.1262	0.0996	0.1052	0.1268	0.1145
9	Inferotemporal	0.2473	0.1108	0.0922	-0.1113	0.1404
Absolute mean		0.1579	0.1346	0.1290	0.1131	

In Table 9, experimental results also show that different correlation patterns exhibit in transitions of macular structure from healthy young age to healthy middle age and from healthy middle age to diseased case. When the macula texture feature τ for a young subject is closer to the centriod of that of the normal age group, fractals in superior area and fircations in both optic disc and superior areas show the most negative correlations with τ. Moreover, lengths in optic disc and superonasal areas and curvatures in superonasal area show the most positive correlations with τ. And overall, structures of vessels in optic disc area have strongest correlations with changes of macular structures and with lengths of vessels the most notable descriptor. The results indicate that when τ migrating from normal young age feature cluster into normal middle age cluster, correspondingly, it exhibits less fractal dimensions and fircation points compared to its average level in most regions on retina and the area has most pronounced correlation is identified to be within the optic disc area.

Table 9: Calculated correlation factors under statistical condition *I2*.

Region #	Region name	Fractals	Curvatures	Fircations	Lengths	***Absolute mean***
1	Macula	-0.0711	-0.1279	-0.1454	-0.0671	0.1029
2	Optic Disc	-0.2936	-0.2044	-0.3536	0.312	0.2909
3	Temporal	0.0267	0.0501	0.0575	-0.1174	0.0629
4	Superior	-0.3754	0.0523	-0.3348	0.1455	0.2270
5	Inferior	0.0128	-0.1654	-0.1956	-0.0962	0.1175
6	Superonasal	-0.0163	0.2934	0.0166	0.2952	0.1554
7	Inferonasal	-0.0917	0.0491	-0.0509	0.116	0.0769
8	Superotemporal	-0.0054	-0.0041	-0.0044	-0.0599	0.0185
9	Inferotemporal	0.1767	0.1306	-0.0167	-0.1406	0.1162
	Absolute mean	0.1189	0.1197	0.1306	0.1500	

In Table 10, it is shown that when the macula texture μ of a normal middle age subject is closer to the centroid of that of the diseased age group, fractals is the most pronounced vessel feature descriptor that shows the strongest correlation to γ. Fractals in macula, superior and inferior areas show the most negative correlations while in inferonasal and inferotemporal areas they show the most positive correlations. Moreover, curvatures in most areas on retina show positive correlations. The results indicate that when γ migrating from normal middle age cluster into diseased cluster, fractal dimensions within and surround the macula area tend to below their average level. On the other hand, fractals of the areas in superonasal and inferonasal or superotemporal and inferotemporal away from macular tend to be above its average level. Also, vessels are of more curved nature than the normal range.

Table 10: Calculated correlation factors under statistical condition *I3*.

Region #	Region name	Fractals	Curvatures	Fircations	Lengths	Absolute mean
1	Macula	-0.3372	-0.1336	-0.1921	0.0369	0.1750
2	Optic Disc	-0.231	-0.0801	-0.1787	-0.0008	0.1227
3	Temporal	-0.138	0.0865	-0.0315	-0.0629	0.0797
4	Superior	-0.3482	0.15	-0.0151	-0.0035	0.1292
5	Inferior	-0.2633	0.2819	-0.2039	-0.0646	0.2034
6	Superonasal	0.1992	0.277	0.142	0.2651	0.2208
7	Inferonasal	0.367	0.1627	0.1933	0.1074	0.2076
8	Superotemporal	0.1991	0.1435	0.2604	0.235	0.2095
9	Inferotemporal	0.2994	0.1701	0.1636	-0.113	0.1865
Absolute mean		0.2647	0.1650	0.1534	0.0988	

5. Discussions

Figure 36 indicates the general trend of structural changes in vessels when retina migrates from young to middle age and from healthy to diseased conditions by comparing their feature means. Table 9 and 10 indicate the trend of structural changes in vascular network of G_M and G_Y conditioning on textural migrations within macular areas. We discuss the commonalities and differences in the inferred results from the two. We take the inferred results of the comparison in fractal dimensions between two the population groups G_M and G_D as an example. On Figure 36, it is inferred that fractals on different areas of normal middle age retina are bigger than those on diseased retinas. On Table 10, we inferred from the signs of correlation coefficients that for the given G_M, when its macular structure migrate from G_M to G_D, fractal dimensions of vessel structures in the macula, optic disc, superior, inferior and temporal areas are below their average levels (indicating the trend of decrease) while the rest of regions tend to be above their average levels (indicating the trend of increase). The similarities and differences of the two inferred results can be explained by the fact vessel structure is susceptible to varying stimulus of disease and aging conditions. In correlation study, among the different factors that relate to the structural changes in vascular network, we pronounce and condition on the factors of migration of macular textures. Therefore, we find many analytical results inferred from Table 10 comply with that of Figure 36 while some others disagree. As such, our correlation study provides valuable insights into the correlation between the macular texture and vessel structure, which are not reflected in Figure 36.

The derived result of our correlation analysis is based on 96 images. The number of diseased retinas is relatively small due to the relatively few subjects contracted with macula diseases as were met in practical clinical setting. Clearly, when the number of image samples increases, it will provide a study result of even more relevance, which helps clinical physicians and medical doctors in the interpretation and understanding the underlying mechanism of retina function, disease formation as well as medical record tracking.

In summary, the proposed method provides valuable insights into the correlation between the macular texture and vessel structure based on image analysis on retinal images. The numerical index of the correlation coefficients indicates the relative importance among the features that characterize the pattern of local vessel morphology in response to the structural change in macular texture against different statistical conditions. It contributes to our approach to understanding the underlying functioning and interaction of the two noted organelles.

D. Similarity-based Ranked Retrieval on Retinal Image Database

In this session, we apply our analytical results to similarity-based ranked retrieval on retina image database and demonstrate the initial results we have made.

Image data has different semantic meanings in different contexts. In order to develop techniques of image retrieval system, it is required to understand the users' query needs and how they are interfaced to the system. Physicians mainly use image data to track, interpret and even predict the medical information. Proliferation of digital image collection has dramatically broadened information access, which leads to more promising and fruitful medical findings through image comparisons, categorizations and predictive modeling. When the data amount is large, however, manual searching and comparison of image data is quite a labor intensive task. It therefore, pushes the need of computer-aided information system to automate the whole process.

With the wealth collection of digital retina images, our ranked retrieval system on retina image database is to bring out the top ranked retrieval results that bear the closest resemblance to the query data based on its medical content. Our following discussion on the ranked retrieval design focuses on the two open problems. The first is on the representation of retinal image content. The second is on the evaluation of ranked retrieval outcome.

1. System Architecture

We first introduce the system architecture our ranked retrieval system. Figure 37 shows the system architecture of our retrieval system. The user inputs a query image on the client side. On server side, the backend engine do image analysis on the query retinal image, extract the image features and organize them into metadata in numerical format (in XML file). It then search in the image database and return the ranked retrieval image results to the client side based on the similarity measures in the metadata.

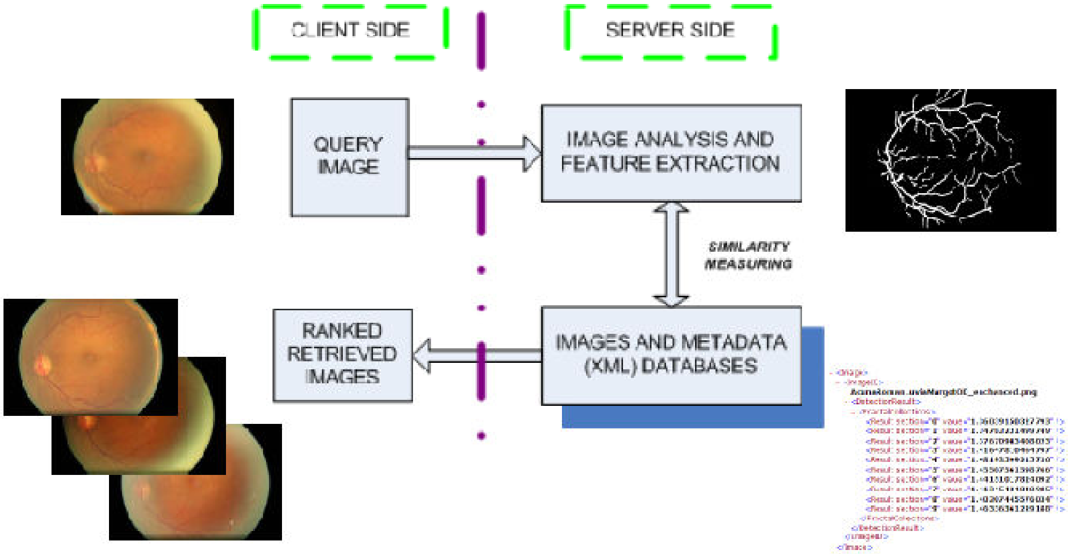

Figure 37: System architecture of ranked retrieval system on retinal images.

2. Content Representation

Medical information on retinal image is described by the physical property of the photographed retinal objects. We could therefore extract the attributes of the detected retinal objects to infer its medical health. In this dissertation, we have studied so far the attributes of vascular network structure and the macular texture. Among the many factors that describe the retinal health, we have known that vascular network exhibits highly dynamic changes with respect to aging or presence of diseases. Feature analysis of vascular structure has been done by extraction of morphological pattern of vessel segments. In Figure 36, it is clearly shown that vessel structures of different population groups have distinct patterns of fractal dimensions against different regions. Further, regional fractals have the strongest correlation to the macular texture.

In this session, we use these analytical results to develop ranked retrieval system on retinal image database by using the regional fractal dimension as the main feature to represent the image content. We further apply the results of our correlation analysis between vessel structure and macular texture by assigning different weights to regional fractals and compare its retrieved outcomes to the original one. Similarity metric is calculated by Mehalanobis distance and on the nearest neighbor approach. In a k-ranked retrieval system, the ranked retrieval results are the k nearest neighbor to the query in terms of the calculated Mehalanobis distance.

3. Evaluation Metric

Evaluation of performances of information retrieval outcome is an even more open problem in the research community of information retrieval. On one hand, performance evaluation measures the relative differences of the underlying principle of different similarity metrics under different conditions. On the other hand, evaluation drives and identifies what needs to be retrieved. Among the different proposed evaluation measures for ranked retrieval system, we used the metric of *"Normalized Discounted Cumulative Gain"(NDCG)* to evaluate our system performance [107].

NDCG is designed for situations of non-binary notions of relevance and is used to evaluate over some number k of top search results. For a set of queries Q, let *C(j)* be the relevance score assessors gave to retrieved outcome for query j. Then, *NDCG* at position n is denoted as:

$$NDCG@n = Z_n \sum_{j=1}^{n} (2^{c(j)} - 1)/\log(1 + j)$$

where Z_n is a normalization factor calculated to make it so that a perfect ranking's *NDCG* at n is 1. The relevance score of a retrieve outcome is based on the following criteria: population group (1.5), diseased condition (1.5), field-type (1), field clarity (0.5) and illumination condition (0.5). Scores of each criterion is shown in their following brackets.

4. Experimental Results and Discussions

Our ranked retrieval algorithm is tested on 20 query images on an image database of 895 images. Table 11 shows the average and standard deviations of *NDCG* scores for the top 5 ranked retrieval results. Initial test results show that regional fractal analysis is an important attribute to indicate the aging and diseased content, which is of the key concern for retina image retrieval. Our test results also show that by tuning the weighting among fractals against different regions using the derived correlation coefficients, *NDCG* score will be slightly improved.

Table 11: Performance evaluation of ranked retrieval outcome.

NDCG @ n	*n=1*	*n=2*	*n=3*	*n=4*	*n=5*
fractal features	0.8665±0.2669	0.7949±0.2536	0.7527±0.2303	0.7295±0.1927	0.7359±0.1631
weighted fractal features	0.8665±0.2669	0.8466±0.2200	0.8235±0.1825	0.7909±0.1806	0.7805±0.1693

In summary, our design of the ranked retrieval system is still at its initial stage. Still, much can be improved in terms of both content representation and evaluation metrics. Current progress of our ranked retrieval system based on the analytical results on retina images demonstrate that it is quite promising research direction to follow in the future work.

E. Summary of the Chapter

In this chapter, we do quantitative analysis on the segmented objects on retinas. Within the cropped macular-fovea area, we first do texture analysis and classification of macular-fovea areas relating to different population groups. Using entropy statistics of Gabor filter responses as the texture features and dimensionality reduction technique of LDA, our algorithm achieves classification rate of 85% using kNN classifier on the test data sets. Using the LDA result as the texture features of macular area, we continue to study its correlation to the structures of vascular network. The vascular network exhibits dynamic changes in topologies due to repair and modification processes. On the other hand, textures are the main changes manifested in macular areas of people in different ages and health groups. Even though qualitative medical studies confirmed that degradation of the vascular network caused by diseases or aging lead to deteriorations of the macular functions, as of now, there is few known quantitative technique which can characterize the relationship between changes in the macular texture from that of the vascular network structure based on image analysis on retinal images. We characterize the structure of vascular network by doing regional analysis of its morphological structures. Our study is conducted to demonstrate the correlation pattern between the structural change in vascular network and the textural migration in macular-fovea area against different statistical conditions. The chapter is concluded by applying our analytical results to the design of a ranked retrieval system on retina image database. Initial results in its increased performances in *NDCG* metric on our ranked retrieval algorithms have demonstrated the effectiveness of our method.

CHAPTER VI

CONCLUSION

In this work, I investigate and develop an overarching analytical framework to support computer-aided analysis of retinal images. Experimental results show that our scheme can be used to construct robust, accurate low level image analysis functions, which would require little, if any, parameter calibration to achieve optimal performance. These low level functions form the foundation for high level statistical analysis techniques of high level system dynamics.

Being able to automate the entire modeling process is important to deal with various imaging conditions, such as illumination setting, disease conditions and incomplete field of view, which occur in real world operations routinely. Different from most traditional modeling techniques, our work is derived from a well established yet largely ignored anatomic property: the generation levels of a vascular network. Medical study has proved that a blood vascular network is consisted of different generation levels based on their width, length and locations.

Two novel feature descriptors S_p and E_p of the *radial contrast transform (RCT)* of image pixels effectively capture patterns of the physical property of vessel generations in the feature space. As a result, we can fit the histogram plot of the S_p descriptor for vessel pixels to a lognormal distribution curve, due to the fixed ratios of vessels pixels among different generation levels. The model is effectively used to study the relationship of segmentation sensitivity among different human-labeled vessel maps, and the relationship of vessel pixels and its corresponding boundary pixels. It provides an important statistical tool for the tradeoff analysis between sensitivity and specificity of vessel detection on retinal images.

Based on the modeling technique, we develop a self-adapted retina blood vessel detection algorithm by using an edge detector as a probing tool to acquire vessel statistics. Different from conventional vessel detection algorithms, we develop our mapping process into different stages. By sliding the threshold value of S_p from small to large, the resulted vessel maps presents a growth pattern from "ridge to boundary" and "large to small" process. It can thus serve the purpose of vessel study at different segmentation sensitivity needs. We continue to take the vessel topology analysis for the localization of two landmark retina feature objects of macula-fovea (M-F) and optic disc (OD) area. M-F is an important area on retina, which is responsible for sharp vision of human eyes and OD is the place where major retina blood vessels emerge. Accurate segmentation of these two areas is thus important for automated retina health evaluation and image registrations. In practice, image factors in illumination settings, health conditions and field clarities, etc., make their detection algorithm design a difficult problem. Our method uses their fixed relations in location to vessel topology as the main image cue. Regardless of the severity in retinal diseases, the high level topology of vascular network remains highly predictable. Both our detection algorithms for M-F and OD are tested on the benchmark retinal image databases STARE and DRIVE as well as the data collections from field clinics in our database. Our M-F localization algorithm achieves 93.4% on STARE, 100% on DRIVE, and 95.75% on our database. Our OD segmentation algorithm achieves 93.83% on STARE, 100% on DRIVE and 92% on our database. Both their performances are comparable or better than the state-of-art algorithms in the field of study.

Based on the low level analysis results, we conclude our discussion by developing high level applications on retinal images by doing quantitative analysis on the detected landmark retina objects. We first show that people belonging to different population groups in their ages and retinal health conditions are associated with different appearances within and around their macula-fovea areas. By doing entropy statistics from the Gabor responses of automatically extracted macula areas, their textures can be well separated and classified on the resulted feature space based on LDA dimensionality reduction technique. Medical study has demonstrated the tight relationship of the M-F and retina blood vessels at the cellular level. Any (non-macular) disease that affects the performance of the vascular network will affect the functionality of the macular subsystem. On the other hand, when the macular subsystem is sick, it may also signal the blood vessel network to change its structure as a part of the biological feedback loop. Even though several clinical studies did confirm the existence such relationships, as of now there is few study which can quantify the nature of these relationships based on automated retinal image analysis. To investigate this interesting problem, we continue to use LDA as the numerical feature values to represent the texture of macula-fovea area and develop an analytical method to quantify the correlation between the texture of the macula-fovea area and the structures of vascular network. We extract local features of furcation point count, lengths, curvatures, and fractal dimensions to characterize the morphological pattern of vessel structure. The correlation analysis between the two is performed based on a standard univariate correlation technique. Under different defined statistical conditions, we can thus identify where and how change of local vascular morphology is correlated to the change in macula-fovea texture. The analytical result contributes to our knowledge of the underlying interaction between the two organelles. Finally, we apply our analytical results to the design of an algorithm for the similarity-based ranked retrieval of retinal images on retina image library. Initial results of our ranked retrieval system have demonstrated its effectiveness in design of image retrieval system on retinas. The proposed approach, though tested only on retinal images, can be extended to other applications.

Experimental results show that the proposed analytical framework can serve as the basis for automated computer-aided analysis of retinal images acquired using a C# based camera control tool. It has been used for field test based on retinal images acquired from clinics. The proposed modeling technique sets a concrete foundation for development of practical management and analysis tools of retina images.

REFERENCES

[1] T. L. McKay, D. J. Gedeon, M. B. Vickerman, A. G. Hylton, D. Ribita, H. H. Olar, P. K. Kaiser, and P. Parsons-Wingerter, "Selective inhibition of angiogenesis in small blood vessels and decrease in vessel diameter throughout the vascular tree by triamcinolone acetonide," *Investigative Ophthalmology and Visual Science*, vol. 49, pp. 1184-1190, 2008.

[2] STARE Project, (Nov.2000) “The stare databases,” University of California, San Diego. Available: http://www.ces.clemson.edu/~ahoover/stare/.

[3] DRIVE Project, (2004) “The drive databases,” Image Sciences Institute, University Medical Center Utrecht. Available: http://www.isi.uu.nl/Research/Databases/DRIVE/.

[4] P. J. Saine and M. E. Tyler, *Ophthalmic photography: retinal photography, angiography, and electronic imaging*, 2nd ed, Boston: Butterworth-Heinemann, 2001.

[5] H. Friedman, “Blood circulation of the eye,” *Blood Vessels and Lymphatics in Organ Systems*, D. I. Abramson and P. B. Dorbin, Orlando: Academic Press Inc., pp.247-258, 1984.

[6] C. W. Oyster, *The Human Eye: Structure and Function*. Birmingham: Sinauer Associates Publishing, 1999.

[7] J. M. Provis, P. L. Penfold, E. E. Cornish, T. M. Sandercoe, and M. C. Madigan, “Anatomy and development of the macula: specialization and the vulnerability to macular degeneration,” *Clinical and Experimental Optometry*, vol. 88, pp.269-281, 2005.

[8] S. Patel, (Nov. 2010), Florida Retina Center. Available: http://patelmd.info.

[9] Z. Ockrim and D. Yorston, "Managing diabetic retinopathy," *BMJ*, vol. 341, pp. 930-935, 2010

[10] C. M. Gibson, (Jan. 2010). Available: http://www.wikidoc.org/index.php/Glaucoma.

[11] S. Chaudhuri, S. Chatterjee, N. Katz, M. Nelson, and M. Goldbaum, "Detection of blood vessels in retinal images using two-dimensional matched filters," *IEEE Transactions on Medical Imaging*, vol. 8, pp. 263-269, 1989.

[12] D. Wu, M. Zhang, and J. Liu, "On the adaptive detection of blood vessels in retinal images," *IEEE Transactions on Biomedical Engineering*, vol. 53, pp. 341-343, 2006.

[13] L. Gang, O. Chutatape, and S. M. Krishnan, "Detection and measurement of retinal vessels in fundus images using amplitude modified second-order Gaussian filter," *IEEE Transactions on Biomedical Engineering*, vol. 49, pp. 168-172, 2002.

[14] O. Chutatape, L. Zheng, and S. M. Krishnan, "Retinal blood vessel detection and tracking by matched Gaussian and Kalman filters," *Proceedings of the 20th Annual Conference of the IEEE Engineering in Medicine and Biology Society*, vol. 6, pp. 3144-3149, 1998.

[15] A. Hoover, V. Kouznetsova, and M. Goldbaum, "Locating blood vessels in retinal images by piecewise threshold probing of a matched filter response," *IEEE Transactions on Medical Imaging*, vol. 19, pp. 203-210, 2000.

[16] K. A. Vermeer, F. M. Vos, H. G. Lemij, and A. M. Vossepoel, “A model based method for retinal blood vessel detection,” *Computers in Biology and Medicine*, vol. 34, pp. 209-219, 2004.

[17] J. V. B.Soares, J. J. G.Leandro, R. M. Cesar, H. F. Jelinek and M. J. Cree, “Retinal vessel segmentation using the 2-D Gabor wavelet and supervised classification,” *IEEE Transactions on Medical Imaging*, vol. 25, pp. 1214-1222, 2006.

[18] M. Sopfka and C. V. Stewart, “Retinal vessel centerline extraction using multiscale matched filters, confidence and edge measures,” *IEEE Transactions on Medical Imaging*, vol. 25, pp. 1531-1546, 2006.

[19] H. F. Jelinek and R. M. Cesar, “Segmentation of retinal fundus vasculature in non-mydriatic camera images using wavelets,” in *Angiography and Plaque Imaging in Advanced Segmentation Techniques*, S. Laxminarayan and J. S. Suri, Eds., London: CRC Press, 2003, pp. 193-224.

[20] F. Zana and J. Klein, “Robust segmentation of vessels from retinal angiography,” *DSP*, vol. 2, pp. 1087-1090, 1977.

[21] F. Zana and J. Klein, “Segmentation of vessel-like patterns using mathematical morphology and curvature evaluation,” *IEEE Transactions on Image Processing*, vol. 10, pp. 1010-1019, 2001.

[22] A. M. Mendonca and A. Campilho, “Segmentation of retinal blood vessels by combining the detection of centerlines and morphological reconstruction,” *IEEE Transaction on Medical Imaging*, vol. 25, pp. 1200-1213, 2006.

[23] A. Can, H. Shen, J. N. Turner, H. L. Tanenbaum, and B. Roysam, “Rapid automated tracing and feature extraction from retinal fundus images using direct

exploratory algorithms," *IEEE Transactions on Information Technology in Biomedicine*, vol. 3, pp. 125-138, 1999.

[24] K. H. Fritzsche, A. Can, H. Sheng, C. Tsai, J. N. Turner, H. L. Tanenbaum, C. V. Stewart, and B. Roysam, "Automated model-based segmentation, tracing, and analysis of retinal vasculature from digital fundus images," in *Angiography and Plaque Imaging in Advanced Segmentation Techniques*, S. Laxminarayan and J. S. Suri, Eds., London: CRC Press, 2003, pp. 225-290.

[25] A. Hoover, V. Kouznetsova, and M. Goldbaum, "Locating blood vessels in retinal images by piecewise threshold probing of a matched filter response," *IEEE Transactions on Medical Imaging*, vol. 19, pp. 203-210, 2000.

[26] X. Y. Jiang and D. Mojon, "Adaptive local thresholding by verification-based multithreshold probing with application to vessel detection in retinal images," *IEEE Transactions on Pattern Analysis and Machine Intelligence*, vol. 25, pp. 131-137, 2003.

[27] A. Bhuiyan, B. Nath, J. Chua, and R. Kotagiri, "Blood vessel segmentation from color retinal Images using unsupervised texture classification," *ICIP*, vol. 5, pp. 521-524, 2007.

[28] S. Supot, C. Thanapong, P. Chuchart, and S. Manas, "Automatic segmentation of blood vessels in retinal image based on Fuzzy K-Mean clustering," *Proceedings of IEEE International Conference on Integration Technology*, vol. 1, pp. 584-488, 2007.

[29] E. Ricci and R. Perfetti, “Retinal blood vessel segmentation using line operators and support vector classification,” *IEEE Transactions on Medical Imaging*, vol. 26, pp. 1357-1365, October 2007.

[30] Y. A. Tolias and S. M. Krishnan, “A fuzzy vessel tracking algorithm for retinal images based on fuzzy clustering,” *IEEE Transactions on Medical Imaging*, vol. 17, pp. 263-273, 1998.

[31] H. Li and O. Chutatape, “Automated feature extraction in color retinal images by a model based approach,” *IEEE Transactions on Biomedical Engineering*, vol. 51, pp. 246-254, 2004.

[32] M. Elena, A. D. Hughes, A. V. Stanton, S. A. Thorn, N. Chapman, et al., “Segmentation of blood vessels from red-free and fluorescein retinal images,” *Medical Image Analysis*, vol. 11, pp. 47-61, 2007.

[33] H. F. Jelinek, M. J. Cree, J. J. Leandro, J. V. Soares, R.M. Cesar, et al., “Automated segmentation of retinal blood vessels and identification of proliferative diabetic retinopathy,” *OpticsInfoBase Soc.Am.A*, vol. 24, pp. 1448-1456, 2007.

[34] D. A. Adjeroh, U. Kandaswamy, and J. V. Odom, “Texton-based segmentation of retinal vessels,” *Optical Society of America*, vol. 24, pp. 1384-1393, 2007.

[35] O. Chutatape, “Fundus foveal localization based on vessel model,” *EMBS*, pp. 4440-4444, 2006.

[36] E. Chaum, T. P. Karnowski, V. P. Govindasamy, M. Abdelrahman, and K. W. Tobin, “Automated diagnosis of retinopathy by content-based image retrieval,” *Retina*, vol. 28, pp. 1463-1477, 2008.

[37] A. D. Fleming, K. A. Goatman, S. Philip, J. A. Olson, and P. F. Sharp, "Automated detection of retinal anatomy to assist diabetic retinopathy screening," *Phys. Med. Bio*, vol. 52, pp. 331-345, 2007.

[38] C. Sinthanayothin, J. Boyce, H. Cook, and T. Williamson, "Automated localization of the optic disc, fovea and retinal blood vessels from digital colour fundus images," *Br F Opthalmol*, vol. 83, pp. 902-910, 1999.

[39] M. V. Ibanez and A. Simo, "Bayesian detection of the fovea in eye fundus angiographies," *Pattern Recognition Letters*, vol. 20, pp. 229-240, 1999.

[40] A. Haddouche, M. Adel, M. Rasigni, J. Conrath, and S. Bourennane, "Detection of the foveal avascular zone on retinal angiograms using Markov random fields," *Digital Signal Processing*, vol. 20, pp. 9, 2010.

[41] A. D Fleming, S. Philip, K. A. Goatman, J. A. Olson, and P. F. Sharp, "Automated assessment of diabetic retinal image quality based on clarity and field definition," *Invest.Ophthalmol.Vis.Sci.*, vol. 47, pp. 1120-1125, 2006.

[42] H. Li and O. Chutatape, "Automatic location of optic disc in retina images," *ICIP*, vol. 2, pp. 837-840, 2001.

[43] M. Lalonde, M. Beaulieu, and L. Gagnon, "Fast and robust optic disc detection using pyramidal decoposition and Hausdorff-Based template matching," *IEEE Transactions on Medical Imaging*, vol. 20, pp. 1193-1200, 2001.

[44] P. Pallawala, W. Hsu, M. L. Lee, and K. G. A. Eong, "Automated optic disc localization and contour detection using ellipse fitting and wavelet transform," *Lecture Notes in Computer Science*, vol. 3022, pp. 139-151, 2004

[45] M. Foracchia, E. Grisan, and A. Ruggeri, “Detection of optic disc in retinal images by means of a geometrical model of vessel structure,” *IEEE Transactions on Medical Imaging*, vol. 23, pp. 1189-1195, 2004.

[46] A. E. Mahfouz and A. S. Fahmy, “Ultrafast optic disc localization using projection of image features,” *ICIP*, vol. 1, pp. 665-668, 2009.

[47] R. Datta, J. Li and J. Z. Wang, “Content-based image retrieval: Approaches and trends of the new age,” *Proceedings ACM International Workshop on Multimedia Information Retrieval*, New York, August 1-2, pp. 253-262, 2005.

[48] D. Heesch, “A survey of browsing models for content based image retrieval,” *Multimed Tools Appl*, vol. 40, pp. 261-284, 2008.

[49] D. Neumann and K. R. Gegenfurtner, “Image retrieval and perceptual similarity,” *ACM Transactions on Applied Perception*, vol. 3, pp. 31-47, 2006.

[50] J. Zhang, W. Hsu, and M. L. Lee, “An information-driven framework for image mining,” *LNCS*, vol, 2113, pp. 232-242, 2001.

[51] Y. Liu, D. Zhang, G. Lu, and W. Ma, “A survey of content-based image retrieval with high level semantics,” *Pattern Recognition Society*, vol. 40, pp. 262-282, 2006.

[52] P. L. Stanchev, D. Green, and B. Dimitrov, “High level color similarity retrieval,” *Int. J. Inf. Theories Appl.* vol. 10, pp. 363-369, 2003.

[53] Y. Liu, D. S. Zhang, G. Lu, and W. Ma, “Region-based image retrieval with perceptual colors,” *Lecture Notes in Computer Science,* vol. 3332, pp. 931-938, 2005.

[54] W. K. Leow and S. Y. Lai, “Scale and orientation-invariant texture matching for image retrieval,” in *Texture Analysis in Machine Vision*, M. K. Pietikaine, Ed., Singapore: World Scientific Publishing, pp. 151-165, 2000.

[55] R. Shi, H. Feng, T. S. Chua, and C. H. Lee, “An adaptive image content representation approach and segmentation approach to automatic image annotation,” *International Conference on Image and Video Retrieval (CIVR)*, Dublin, Ireland, pp. 545-554, 2004.

[56] V. Mezaris, I. Kompatisiaris, and M. G. Strintzis, “An ontology approach to object-based image retrieval,” *ICIP*, vol. 2, pp. 511-514, 2003.

[57] C. Carson, S. Belongie, H. Greenspan, and J. Malik, “Blobworld: Image segmentation using expectation-maximization and its application to image querying,” *IEEE Trans. Pattern Anal. Mach. Intell*, vol. 24, pp. 1026-1038, 2002.

[58] C. P. Town and D. Sinclair, “Content-based image retrieval using semantic visual categories,” Society for Manufacturing Engineers, AT&T Laboratories Cambridge, Technical Report 2000.14, 2000.

[59] J. Z. Wang, J. Li, D. Chan and G. Wiederhold, “Semantics-sensitive retrieval for digital picture libraries,” *Digital Library Magazine*, vol. 5, pp. 11, 1999.

[60] R. C. Veltkamp and M. Tanase, (2002), “Content-based image and video retrieval”. Available: http://www.ai.mit.edu/courses/6.801/Fall2002/lect/lect24.pdf.

[61] M. J. Cree, J. A. Olson, K. C. McHardy, J. V. Forrester, and P. F. Sharp, "Automated microaneurysm detection," *ICIP,* vol. 3, pp. 699-702, 1996,

[62] M. Kamel, S. Belkassim, A. M. Mendonca, and A. Campilho, "A neural network approach for the automatic detection of microaneurysms in retinal angiograms," *IJCNN*, vol. 4, pp. 2695-2699, 2001.

[63] K.Rapantzikos and M. Zervakis, “Nonlinear enhancement and segmentation algorithm for the detection of age-related macular degeneration (AMD) in human eye’s retina,” *ICIP*, vol. 3, pp. 1055-1058, 2001.

[64] S. S. Parvathi and N. Devi, “Automatic drusen detection from color retinal images,” *Internal Conference on Computational Intelligence and Multimedia Applications*, vol. 2, pp. 377-381, Sivakasi, Tamil Nadu, December 13-15, 2007.

[65] A. Khademi and S. Krishnan, “Shift-invariant discrete transform analysis for retinal image classification,” *Medical and Biological Engineering and Computing*, vol. 45, pp. 1211-1222, 2007.

[66] L. Brandon and A. Hoover, “Drusen detection in a retinal image using multi-level analysis,” *Lecture Notes in Computer Science*, vol. 2878, pp. 618-625, 2003.

[67] A. Bindewald, A. C. Bird, S. S. Dandekar, J. D. Szczasny, J. Dreyhaupt, F. W. Fitzke, et al., “Classification of fundus autofluorescene patterns in early age-related macular disease,” *Investigative Ophthalmology & Visual Science*, vol. 46, pp. 3309-3314, 2005.

[68] M. Lamard, G. Cazuguel, G. Quellec, L. Bekri, C. Roux, and B. Cochener, “Content based image retrieval based on wavelet transform coefficients distribution,” *Proceedings of the 29th Annual International Conference of the IEEE EMBS*, Lyon, France, pp. 4532-4535, August 23-26, 2007.

[69] G. Quellec, M. Lamard, G. Cazuguel, B. Cochener, and C. Roux, “Wavelet optimization for content-based image retrieval in medical databases,” *Medical Image Analysis*, vol. 14, pp. 227-241, 2010.

[70] M. D. Amiri, F. A. Tab, and W. Barkhoda, “Retina identification based on the pattern of blood vessels using angular and radial partitioning,” *LNCS*, vol. 5807, pp. 732-739, 2009.

[71] M. Zhang and J. Liu, “Directional local contrast based blood vessel detection in retinal images,” *ICIP,* vol. 4, pp. 317-320, 2007.

[72] E. Peli, "Contrast in complex images," *Journal of the Optical Society of America a-Optics Image Science and Vision*, vol. 7, pp. 2032-2040, 1990.

[73] A. B. Watson, H. B. Barlow, and J. G. Robson, "What does the eye see best," *Nature*, vol. 302, pp. 419-422, 1983.

[74] P. Zingaretti and A. Carbonaro, "Route following based on adaptive visual landmark matching," *Robotics and Autonomous Systems*, vol. 25, pp. 177-184, 1998.

[75] F. Family, B. R.Masters, and D. E. Platt, “Fractal pattern formation in human retinal vessels,” *Physica D: Nonlinear Phenomena*, vol. 38, pp. 98-103, 1989.

[76] B. R. Masters, “Fractal analysis of the vasculature tree in the human retina,” *Annual Review of Biomedical Engineering*, vol. 6, pp. 427-452, 2004.

[77] D. C. Boes, F. A. Graybill, and A. M. Mood, *Introduction to the Theory of Statistics*, 3rd ed, New York: McGraw-Hill, 1974.

[78] G. Casella and R. L. Berger, *Statistical Inference,* 2nd ed, Florida: Thomson Learning, 2000.

[79] E. Limpert, W. A. Stahel, and M. Abbt, “Log-normal distributions across the sciences: Keys and clues,” *BioScience*, vol. 51, pp. 341-352, 2001.

[80] L. G. Blackwood, “The lognormal distribution, environmental data, and radiological monitoring,” *Environmental Monitoring and Assessment*, vol. 21, pp. 93-210, 1992.

[81] C. J. Moravski, D. J. Kelly, M. E. Cooper, R. E. Gilbert, J. F. Bertram, et al., “Retinal neovascularization is prevented by blockade of the renin-angiotensin system,” *Hypertension*, vol. 36, pp. 1099-1104, 2000.

[82] P. A. Campochiaro, “Retinal and choroidal neovascularization,” *Journal of Cellular Physiology*, vol. 184, pp. 301-310, 2000.

[83] R. C. Gonzalez and R. E. Woods, *Digital Image Processing*, 2nd ed, Tennessee: Princeton Hall, 2002.

[84] M. H. Hueckel, “An operator which locates edges in digitized pictures,” *J.Ass.Comput. Mach.*, vol. 18, pp. 113-125, 1971.

[85] J. J. Kanski, *Clinical Ophthalmology: A Systematic Approach*, London, U.K, Butterworth-Heinemann, 1989.

[86] K. W. Bowyer and P. J. Phillips, *Empirical Evaluation Techniques in Computer Vision*, Piscataway, NJ: IEEE Press, 1998.

[87] J. Staal, M. D. Abramoff, M. Niemeijer, M. A. Viergever, and B. V. Ginneken, "Ridge-based vessel segmentation in color images of the retina," *IEEE Transactions on Medical Imaging*, vol. 23, pp. 501-509, 2004.

[88] B. Shu, Y. Lam, and H. Yan, “A novel vessel segmentation algorithm for pathological retina Images based on the divergence of vector fields,” *IEEE Transactions on Medical Imaging*, vol.27, pp. 237-246, 2008.

[89] M. Niemeijer, M.D. Abramoff and V.Ginneken, “Segmentation of the optic disc, macula and vascular arch in fundus photographs,” *IEEE Trans on Medical Imaging*, vol. 26, pp. 116-127, 2007.

[90] C. Rusu, M, Tico, P. Kuosmanen, E. J. Delp, “Classical geometrical approach to circle fitting-review and new developments,” *Journal of Electronic Imaging*, vol. 12, pp. 179-193, 2003.

[91] A. Daxer, “Characterization of the neovascularisation process in diabetic retinopathy by means of fractal geometry: Diagnostic implications,” *Graef’s Arch Clin Exp Ophthalmol*, vol. 231, pp. 681-686, 1993.

[92] A. Avakian, R. E. Kalina, E. H. Sage, A. H. Rambhia, K. E. Elliott, et al., “Fractal analysis of region-based vascular change in the normal and non-proliferative diabetic retina,” *Current Eye Research*, vol. 24, pp. 274-280, 2002.

[93] M. Cusick, “Histopathology and regression of retinal hard exudates in diabetic retinopathy after reduction of elevated serum lipid levels,” *Ophthalmology*, vol. 110, pp. 2126-2133, 2003.

[94] C. Lee and S. Wang, “Fingerprint feature extraction using Gabor filters,” *Electronics Letters*, vol. 35, pp. 288-290, 1999.

[95] D. A. Clausi and M. E. Jernigan, “Designing Gabor filters for optimal texture separability,” *Pattern Recognition*, vol. 33, pp. 1835-1849, 2000.

[96] M. Idrissa and M. Acheroy, “Texture classification using Gabor filters,” *Pattern Recognition Letters*, vol. 23, pp. 1095-1102, 2002.

[97] A. Kunmar and G. K. H. Pang, “Defect detection in textured materials using Gabor filters,” *IEEE Transactions on Industry Applications*, vol. 38, pp. 425-440, 2002.

[98] S. R. Cloude and E. Pottier, “An entropy based classification scheme for land applications of polarimetric SAR,” *IEEE Transactions on Geoscience and Remote Sensing*, vol. 35, pp. 68-78, 1997.

[99] C. M. Bishop, “Pattern recognition and machine learning,” 3rd ed, Cambridge: Springer, 2006.

[100] R. L. Engerman, “Development of the macular circulation,” *Invest. Ophthalmol. Vis. Sci*, vol. 15, pp. 835-840, 1976.

[101] N. M. Bressier, S. B. Bressier, and S. L. Fine, “Age-related macular degeneration,” *Survey of Ophthalmology*, vol. 32, pp. 375-413, 1988.

[102] P. L. Penfold, J. F. Gyory, A. B. Hunyor, and F. A. Billson, “Exudative macular degeneration and intravitreal triamcinolone: A pilot study,” *Australian and New Zealand Journal of Ophthalmology*, vol. 23, pp. 293-298, 1995.

[103] A. Scheider, O. Guendisch, and A. Kampik, “Surgical extraction of subfoveal choroidal new vessels and submacular haemorrhage in age-related macular degeneration: Results of a prospective study,” *Graefe’s Archive for Clinical and Experimental Ophthalmology*, vol. 237, pp. 10-15, 1999.

[104] H. Funatsu, M. Yamasaki, H. Tsukamoto, T. Mimura, T. Sone, et al., “Pathogenesis of Macular Edema With Branch Retinal Vein Occlusion and

Intraocular Levels of Vascular Endothelial Growth Factor and Interleukin-6," *American Journal of Ophthalmology*, vol. 140, pp. 256.e1-256.e7, 2005.

[105] M. Vinten, M. Larsen, H. L. Andersen, B. Sander, and M. L. Cour, "Short –term effects of intravitreal triamcinolone on retinal vascular leakage and trunk vessel diameters in diabetic macular oedema," *Acta Ophthalmologica Scandinavica*, vol. 85, pp. 21-26, 2007.

[106] W. E. Hart, M. Glodbaum, B. Cote, P. Kube, and M. R. Nelson, "Measurement and classification of retinal vascular tortuosity," *International Journal of Medical Informatics*, vol. 53, pp. 239-252, 1999.

[107] C. D. Manning, P. Raghavan, and H. Schuetze, *An Introduction to Information Retrieval*, Cambridge, England: Cambridge University Press, 2008.

VITA

Huajun Ying received his B.S. degree in electrical engineering in 2005, from Shanghai JiaoTong University in Shanghai, China. In 2006, he worked as a research assistant in Zhejiang University doing research work on electric motor design.

Dr. Ying began working toward his doctoral degree in Texas A&M University in August 2006 under the supervision of Dr. Jyh-Charn (Steve) Liu and graduated with his Ph.D. in May 2011. His research areas of interest include medical image processing, pattern recognition and signal processing. His permanent address is:

Department of Computer Science, Texas A&M University,
College Station, TX, 77843-3112